"Homo liber nulla de re minus quam de morte cogitat;
et ejus sapientia non mortis sed vitae meditatio est"

Baruch de Spinoza

Sándalo Roldán Vargas

Structure and Dynamics of Colloidal Systems with Application to Vesicle Suspensions

Sándalo Roldán Vargas

Departamento de Física Aplicada
Universidad de Granada

TESIS DOCTORAL 2011

Structure and Dynamics of Colloidal Systems
with Application to Vesicle Suspensions

$$m\frac{dv(t)}{dt} = -\beta v(t) + F(t)$$

$$\lim_{r\to 0} -\frac{\log N(r)}{\log r} = D$$

University of Granada
Faculty of Sciences

Applied Physics Department
Biocolloid and Fluid Physics Group

Structure and Dynamics of Colloidal Systems with Application to Vesicle Suspensions

Sándalo Roldán Vargas

PhD. Thesis

Editor: Editorial de la Universidad de Granada
Autor: Sándalo Roldán Vargas
D.L.: GR 1411-2012
ISBN: 978-84-694-4447-4

Structure and Dynamics of Colloidal Systems with Application to Vesicle Suspensions

by

Sándalo Roldán Vargas

SUPERVISORS

Dr. D. José Callejas Fernández
Catedrático de Física Aplicada
Universidad de Granada

Dr. D. Manuel Quesada Pérez
Prof. Titular de Física Aplicada
Universidad de Jaén

This dissertation is presented
in partial fullfitment
of the requirements for the degree
of Doctor of the University of Granada
and Doctor Europeus
Granada, 2011

Agradecimientos

Considero que los agradecimientos de las tesis doctorales deberían ser, si no lo son ya, objeto de un serio estudio antropológico. Por mi parte, añado un elemento más a ese material de estudio, entendiéndose que en él está mi más sincero agradecimiento a lo mucho que muchos me han dado durante estos años.

Empiezo agradeciendo, es lo justo, a José Callejas y Manuel Quesada el personificar la dirección de esta tesis. En particular, a ti, Pepe, te agradezco el haberme ofrecido tus buenas intuiciones, tu humanidad y tu ilusión. Reivindico esa humanidad y esa ilusión, que siempre imagino vestidas con bata blanca. Sigo contigo, Roque: me abriste la puerta. Nunca lo olvidaré.

Muestro, además, mi agradecimiento a toda la buena gente que en algún momento me ofreció su amabilidad desinteresadamente durante mi camino por el grupo i8. Fueron muchos. Entre ellos, A Delfi y a Juan Luis les agradezco el cariño con el que siempre me trataron. A Juan de Vicente el saber ser y el saber estar. A Arturo el compartir conmigo su talento y su gracia. Añado, además, los nombres de Javier Montes, Catalina, Artur y Teresa. Por último, a los que vivís con nosotros, Alicia, Conrado y José Antonio, os agradezco vuestra eficacia y vuestra gentileza.

Separo ahora a unos pocos. A Manolo Santander le agradezco el compartir conmigo su alma de tomillos y libélulas: un alma de hombre bueno. A Roberto, claro que sí, su chispa; pero también le conmino a seguir cultivando su rebeldía para crear con ella entes vivos. A Joaquín su eterna defensa del optimismo. A Fernando Vereda su serena discreción y su amor por las cosas bien hechas. A Francisco Martínez el mostrarse siempre ante mí como Paco. A Ignacio Pérez Victoria el enriquecerme durante nuestra colaboración con su inteligencia, su confianza y su determinación. A Fernando Martínez el "sueña el rico en su riqueza…", el magnetismo y el cariño. Al Moro su fuerza, su curiosidad y su endemoniado sentimiento, así como la voluntad de no traicionarlos nunca. Para ti, Juan Carlos, dejo aquí escrito que te quiero; con tus "yo", con tus "tú", con tus "él" cuando quieres decir "tú": con cualquiera de tus pronombres, te quiero.

Finalmente, a ti, Miguel Alberto, te agradezco la palabra “amigo”. Todos vosotros sois para mí gloriosas excepciones en un mundo que a veces se me antoja vacío casi por doquier, hecho a la medida del ignorante y del oportunista, y en el que ya no todos los hombres desean saber.

Ara torno la mirada cap a Barcelona. Al meu amic Joan Estelrich li agraeixo el plaer de treballar i enraonar amb ell. A Ramon Barnadas la seva amistat més enllà de la simple col.laboració, el seu suport sense condicions, les seves brillants idees i la seva honestedat com a científic.

Let us go to Montpellier. Thanks to Walter Kob and Ludovic Berthier for sharing with me their time, their knowledge, and also their dreams. Merci beaucoup, Ludo. Vielen dank, Walter.

A mis amigos de la facultad: A Rolo el ser bueno y el honrar a sus amigos. A Manolo el hacerme ver que yo también quiero salir a pasear cuando llegue ese día. A Miguel Niño (entiéndeme bien, Miguel) le agradezco sus valores decimonónicos; empezamos a menguar el día que perdimos esos valores. A Paco el perdonarme muchas ausencias. A José Carlos el haber respirado Física conmigo.

Fuera de la “Academia”, a Manolo Guerrero le agradezco el ser mi maestro. A mi amigo Carlos Sanz su verdad geológica. A mi “foro”: Ginés, Gabriel, Javier, Victor, Joan Carles, Pablo, Marcos y Antonio, sólo os digo que sois la parte luminosa del mundo. A Merche le agradezco el haberme querido, el quererme y el haberme dejado quererla. For you, Cynthia, my dear, I will commit a sin by changing a verse of our uncle Walt: Not “Goodbye” but “Hello- and hail! my Fancy”.

A mi calle Garzón: A Pepe le agradezco el poder llamarle, con justicia, Ismael. A Lourdes su pañuelo y el honor de defenderlo. A mi compadre Rafa el que me siga llamando “mi niño”.

A mis amigos de siempre: A mi Cañi su inquebrantable fidelidad y su amor a la vida. A Jose una niñez, una adolescencia y un sentimiento perenne. A Alejandro el compartir su felicidad, sin saber que él mismo es feliz. A Paco, mi Paco, el "para siempre". Y por último, tú, Miguel: eres parte de mí mismo.

Termino: Lucía, mi felicidad vive debajo de tu sonrisa. Carmela, yo te enseñé Física con mis manos, tú me enseñaste a hacer monaguillos con las amapolas.

Esta tesis está dedicada a mi familia y, por encima de todo, a mis hermanos: Antonio, Pauli y Mari. Vuestro amor me ha acompañado desde niño. Vuestra presencia ha iluminado mi vida.

Mis últimas palabras son para los que se fueron, siempre demasiado pronto. Vivís en estas páginas porque en mí seguís viviendo.

La Zubia, Granada, 14 de Marzo de 2011

Contents

Part 3. Glass Transition: Experiment and Simulation

Further Acknowledgements: Thanks to Ramon Barnadas for the design of the cover and back cover of this dissertation, to Cynthia Reyero for the careful reading of this manuscript, and to Manuel Santander for offering me his picture, “Jaramagos”.

"*Any serious consideration of a physical theory must take into account the distinction between the objective reality, which is independent of any theory, and the physical concepts with which the theory operates. These concepts are intented to correspond with the objective reality, and by means of these concepts we picture this reality to ourselves.*"

A. Einstein, B. Podolski, and N. Rosen,
Phys. Rev. **47**, 777 (1935)

"*La primavera ha venido.*
Nadie sabe cómo ha sido."

Antonio Machado,
Nuevas Canciones (1917-1930),
CLIX (Canciones), III

Chapter 1

Introduction

Why does Physics study colloidal systems? An oversimplified answer to this question could be: Physics studies natural processes from a fundamental viewpoint and colloidal systems show the emergence of several interesting natural processes such as the appearance of fractal structures, phase transitions, or the manifestation of Brownian motion as consequence of the interaction between liquid molecules and nanometric particles. That is, processes which are examples of phenomena present in many body systems. However, we have an additional reason which is less obvious but still true: Colloidal systems represent a field for testing theoretical models that were in principle developed for molecular or atomic systems. For instance, theories that were created to explain phase transitions which occur in molecular liquids are legitimately probed on colloidal systems.

We can also argue that colloids have a ubiquitious presence in everyday life and, therefore, a significant interest *per se*. Thus, nowadays technology, mainly associated with industrial and biomedical applications, has an underlying colloidal "substratum". Probably more fascinating, biological objects suspended in their physiological medium such as DNA, cells, erythrocytes or leukocytes (to mention only a few examples) are colloids. In general, according to the very nature of its interactions and its typical time and length scales, the "biological world" is a colloidal world.

Motivated by these considerations, this dissertation is an attempt for rationalizing some of the emerging phenomena which are understood in terms of the interactions between colloidal particles suspended in a molecular liquid. These phenomena have two coupled manifestations: Structure and Dynamics. Here *Structure* will be defined by the static

spatial correlations between the colloidal particles which form the system, where *static* will refer to the average of time independent observables over an ensemble of equilibrated colloidal systems. By *Dynamics* we will not signify the classical deterministic motion of a set of particles as the result of their interactions but the probabilistic representation of the relaxation of those fluctuations arising in a system in equilibrium.

Different methodologies were employed to carry out the investigations present in this dissertation. From the experimental viewpoint, our most recurrent techniques will be dynamic and static light scattering, which will be complemented by cryotransmission electron microscopy, infrared spectroscopy and rheology. With these techniques we pretend to resolve in space and/or time those processes which constitute the object of our research. In addition, theoretical models will be proposed, and validated, for describing quantitatively our experimental results. For instance, the fluctuating signal scattered by a suspension of Brownian particles will be explained using as basis the mathematical formalism of the stochastic processes. Numerical models will be employed to describe the aggregation processes arising in a suspension of colloidal particles dominated by short range attractions. Mechanical statistical models will be also probed to account for by the experimental phenomenology of a colloidal system near the glass transition. Finally, numerical simulations based on molecular dynamics will be used as a predictive tool to tackle some of the present open problems which concern the glass transition phenomenon.

Although not the unique, suspensions of lipid vesicles (liposomes) are here our main experimental system. Two essential reasons can be provided to argument our choice. First, liposomes present singular and useful properties to perform reliable and general experimental studies whose results can be extended to other colloidal systems. For instance, their size and surface charge can be controlled adequately whereas their refractive index, which is slightly different from that of the aqueous medium, allows us to prepare nearly transparent suspensions at high volume fractions. Second, the study of liposome suspensions has contributed over the last decades to a better understanding of biological processes involving cellular phenomena. Moreover, significant applications such as drug delivery or biological transport through the lipid membranes have been

developed from the synthesis of model liposome systems. Thus, here we will present results concerning some specific issues of liposome suspensions such as the study of the lipid membrane deformability or the influence of divalent cations on the hydration grade of the lipid molecules, a key point for understanding the aggregation and fusion of lipid membranes.

The outline of this dissertation has been separated according to our aims. First, we will provide the reader with a concise but sufficient theoretical background to understand our main findings (chapters 2 to 5). Second, we will present our experimental and theoretical results concerning the Brownian dynamics of colloidal particles at short and long times (papers I and II). In this respect, special attention will be paid to the Brownian motion of deformable particles, an issue which is surprisingly scarce in the previous literature. Third, we will present the first example of structure through our investigation concerning the fractal organizations emerging in liposome suspensions governed by short range attractions under the influence of divalent cations (papers III and IV). In this sense, we will discriminate between those results which are common to other colloidal systems and those which are specific of systems at which hydration forces play a central role. We devote the final part of this dissertation to the study of the puzzling problem of the glass transition (papers V and VI). Thus, we will deal with the structure and dynamics of systems near the glass transition which are dominated by repulsive interactions. In this respect, the glass transition will be studied experimental and theoretically by offering a common description in time and frequency domains. Finally, based on molecular dynamics simulations (which can also be applied to molecular liquids), we present our interpretation of the glass transition phenomenon by recovering the old debate of its controversial origin in an attempt to reconcile its kinetic and thermodynamic perspectives.

In a crude sense, this dissertation treats the ancient concept of *Emergence* and its manifestation in colloidal systems. That is, those complex patterns and self-organizations arising in many body systems for which we know in principle the simple interactions between two isolated particles. Fractals are an emergence. Glasses are an emergence whose cause is not completely understood. Finally, the most fascinating and mysterious: Life itself is an emergence.

Chapter 2

Interactions in Colloidal Suspensions

In classical Physics, the *mechanical state* of a system of particles is completely determined at any instant if all the coordinates and velocities are simultaneously specified. The future state of the system is then determined by the relations between the accelerations, velocities and coordinates, that is, by means of the *equations of motion*.

In spite of this experimental fact, there are several examples for which the mechanical phenomenology of a system is described by probabilistic laws. This description is often consequence of the non-accessibility to the mechanical state of the system (usually determined by a large number of variables) with a sufficiently accurate temporal coarse graining ("level of detail"). Historically, one of the reference systems studied by this stochastic description is a suspension of Brownian particles whose motion is subjected to different mechanical constraints (classical references are [1-3]). The study of this motion, present in any system of colloidal particles suspended in a liquid medium, will be the starting point of this Chapter.

2.1. Brownian Motion

By *Brownian motion* we understand indistinctly the "random" motion of mesoscopic particles suspended in a liquid without direct interaction between them as well as the mathematical model describing this motion.

One of the first documented observations of Brownian motion, from which its name was coined, was performed by the English botanic Robert Brown (1827) while looking through a simple microscope at the erratic motion of micron-scale pollen grains suspended in water [4]:

"*While examining the form of these particles immersed in water, I observed many of them very evidently in motion [...] These motions were such as to satisfy me, after frequently repeated observation, that they arose neither from currents in the fluid, nor from its gradual evaporation, but belonged to the particle itself.*"

Robert Brown's interpretation (…*belonged to the particle itself*) was definitively rejected at the beginning of the 20th century when Einstein [5], von Smoluchowski [6], Langevin [7], and Perrin [8] established and validated the theoretical fundamentals of Brownian motion, supporting their new interpretation on the molecular constitution of the liquid. The Brownian particle would collide with the light molecules of the liquid in an extremely frequent fashion, leading the particle to perform jumps supposedly uncorrelated. The duration of these collisions would be too short to be discriminated, therefore, the continuous change of Brownian velocity would not be appreciated. Thus, under this temporal coarse graining, the future velocity of the particle depends on the present velocity but not on its earlier values[1].

The first physical model of Brownian motion in which velocity was considered came with the *Langevin Equation* [1, 7]. Langevin equation interprets the interaction between the Brownian particle and its surrounding liquid in terms of two forces associated with a common origin, a systematic friction and a fluctuating noise, with no considerations of hydrodynamic memory effects. To facilitate our discussion, we treat the motion as if it were one-dimensional without loss of generality:

$$m\frac{dv(t)}{dt} = -\beta v(t) + F(t) \qquad (2.1)$$

m being the mass of the Brownian particle, $v(t)$ its velocity at time t, β is the friction coefficient, and $F(t)$ a stochastic force[2]. The frictional term, $-\beta v(t)$, is assumed to be governed by Stokes' law, which in case of spherical particles takes the form $\beta = 6\pi R\eta$.

[1] Formally speaking, the Brownian velocity would be Markovian. A formal definition of the Markovian property can be found in Paper II.

[2] The systematic friction, $-\beta v(t)$, and the fluctuating noise, $F(t)$, represent in fact a manifestation of the so-called fluctuation-dissipation theorem [9] since they are associated with a common origin: The interaction between the Brownian particle with the liquid molecules.

Here R is the radius of the particle whereas η is the shear viscosity of the liquid. Concerning the "fluctuating part", $F(t)$, two *a priori* hypotheses, which are characteristic of Brownian motion, are assumed:

1- $F(t)$ is a Gaussian stochastic process with $\langle F(t)\rangle = 0$ [3].

2- $\langle F(t)F(t+\tau)\rangle \propto \delta(\tau)$.

Hypothesis 1 considers $F(t)$ as the result of several independent and isotropic collisions between the Brownian particle and the liquid molecules. Therefore, by virtue of the Central Limit Theorem, $F(t)$ is a Gaussian process with a zero time-averaged value [10-12]. Hypothesis 2 establishes that the collisions between the Brownian particle and the liquid molecules are uncorrelated[4] (or, formally speaking, delta-correlated). This is a consequence of the temporal coarse graining at which the motion is observed.

In 1930 Ornstein and Uhlenbeck presented the solution of Equation (2.1) under the assumptions 1 and 2, founding their derivation on the relation between any Cartesian component of the mean-square displacement, $\langle \Delta x(\tau)^2 \rangle$, of the Brownian particle and its velocity autocorrelation function, $\langle v_x(0)v_x(t)\rangle$ [1]:

$$\langle \Delta x^2(\tau)\rangle = 2\int_0^{\tau} (\tau - t)\langle v_x(0)v_x(t)\rangle dt \qquad (2.2)$$

[3] Here we assume as time-average: $\langle F(t)\rangle = \lim_{T\to\infty}\frac{1}{T}\int_0^T F(t)dt$

[4] $F(t)$ is the so-called *Gaussian white noise*. Here the adjective Gaussian is not redundant despite sometimes it is incorrectly assumed that the Gaussian property is a necessary condition for the white noise definition. In this respect, there are other frequent examples of white noise with different probability distributions (e.g. Poisson or Cauchy distributions).

They obtained:

$$\left\langle \Delta x^2(\tau) \right\rangle = 2D_0 \left[\tau - \tau_B + \tau_B \exp\left(-\tau / \tau_B\right) \right] \tag{2.3}$$

$$\left\langle v_x(0) v_x(t) \right\rangle = \frac{k_B T}{m} \exp(-t / \tau_B) \tag{2.4}$$

k_B represents Bolztmann's constant and T the absolute temperature[5] (both included to impose the equilibrium Maxwellian variance $\left\langle v_x(t)^2 \right\rangle = k_B T / m$). $D_0 \equiv k_B T / \beta$ is the free particle diffusion coefficient and $\tau_B \equiv 2R^2 \rho / 9\eta$ the Brownian time (ρ being the Brownian particle density).

Two obvious regimes can be discriminated from Equation (2.3). At short times, we have a ballistic regime:

$$\left\langle \Delta x^2(\tau) \right\rangle = \left\langle v_x(t)^2 \right\rangle \tau^2, \tag{2.5}$$

whereas at long times, motion is diffusive:

$$\left\langle \Delta x^2(\tau) \right\rangle = 2D_0 \tau \quad ; \quad (\tau >> \tau_B) \tag{2.6}$$

Where Equation (2.6) is the celebrated result obtained by Einstein in his seminal work "*On the disordered motion of particles suspended in a liquid and its relation to diffusion*" [5][6].

In spite of its mathematical significance, the Langevin equation predicts a rapid and non-realistic transition from ballistic to diffusive motion. A successful description of

[5] We will indistinctly use T for temperature and time. The meaning will be made clear by the dimensionality of the corresponding equation.

[6] Einstein's words concerning the range of applicability of the diffusive time scale are as follows: *"We now introduce a time interval τ, which is very small compared with observable time intervals but still large enough that the motions performed by a particle during two consecutive time intervals τ can be considered as mutually independent events"* [5].

this transition came in the 1960's when Alder and Wainwright [13, 14] found a "…surprising persistence of the velocities" [14] through a "long-time tail" ($\langle v_x(0)v_x(t)\rangle \propto \tau^{-3/2}$) in the velocity autocorrelation function (see Paper I). By means of a molecular dynamics simulation, they "observed" a delay in the emergence of the diffusive motion which was explained in terms of a hydrodynamic memory effect: The fluid would circulate from the front of the particle, where it is compressed, to the rear, where a rarefaction wave is developed. This vorticity effect results in an effective boost that pushes the particle.

This finding was theoretically described by means of a more complete hydrodynamic treatment where vorticity memory effects were considered [15-18]. Accordingly, the mean-square displacement results:

$$\left\langle \Delta x^2(\tau)\right\rangle \cong 2D_0\left[\tau - 2\left(\frac{\tau_L}{\pi}\right)^{1/2}\tau^{1/2} + \frac{\tau_L}{9}\left(8-\frac{2\rho}{\rho'}\right) - \frac{\tau_L^{3/2}}{9\sqrt{\pi}}\left(7-\frac{4\rho}{\rho'}\right)\tau^{-1/2}\right];(\tau \geq \tau_L) \quad (2.7)$$

Here $\tau_L = (9/2)(\rho'/\rho)\tau_B$, where the fluid density, ρ', appears as a new parameter. Thus, despite the fact that both Equation (2.3) and (2.7) tend to a common diffusive regime, $\left\langle \Delta x^2(\tau)\right\rangle = 2D_0\tau$ ($\tau >> \tau_B$), the latter presents a second term, $2(\tau_L/\pi)^{1/2}\tau^{1/2}$, which is easily associated through Equation (2.2) to the long-time tail in the velocity autocorrelation function ($\langle v_x(0)v_x(t)\rangle \propto \tau^{-3/2}$). As a way of example, a simple calculation shows that this second term ($\propto \tau^{1/2}$) represents a fraction $1/(5\sqrt{\pi}-1) \cong 0.13$ of the mean-square displacement at $\tau = 100\tau_L$ for $\rho'/\rho = 1$ (Equation (2.7)) whereas for the same time $\left\langle \Delta x(\tau)^2\right\rangle$ given by Equation (2.3) is close to $2D_0\tau$ in 99.8%.

First, Equation (2.7) was validated on real simple liquids [19, 20]. For rigid colloidal particles, experiments using dynamic light scattering (DLS) [18, 21, 22], diffusing-wave

spectroscopy [23, 24], and optical trapping interferometry [25], have confirmed the existence of the long-time tail[7]. However, the past and present studies are based on the assumption of a hard spheres-like interaction (computer simulations) or a fixed, rigid, geometrical shape of the tracer particles (experiments). In paper I, we extend these studies to deformable Brownian particles for which a lack of investigations still persist.

Thus, in this dissertation we will present a firm experimental observation against the validity of the classic long-time tail prediction (Equation (2.7) in case of deformable Brownian particles. In addition to translational motion, our observation will consider the deformational motion of the particles on timescales of the order of the Brownian time.

2.2. Interparticle Forces

We have discussed the interaction between a colloidal particle and its surrounding liquid using as theoretical basis the classical Brownian model. However, this model is often insufficient when we increase the concentration of the colloidal particles since they start to "feel" the presence of their neighbours. In this case, if we neglect the effect of the external gravitational field, the only active observable governing the direct interaction between colloidal particles is the electric charge. Taking into account this experimental fact, we now present the most relevant interactions between colloidal particles, paying special attention to those that will be most apparent in the experimental systems explored within this dissertation. They are:

1- Electrostatic Repulsion.
2- London-van der Waals Attraction.
3- Hydration Forces.
4- Hydrodynamic Forces.

The classical model constituted by the non-coupled addition of 1 and 2, whose effectiveness has been proven on several colloidal systems, is the so-called *DLVO Theory*, whose acronym was adopted from the works of Derjaguin and Landau [26] and Verwey and Overbeek [27].

[7] Additional results for rigid colloidal particles will be also provided in this dissertation (see Paper I).

2.2.1. Electrostatic Repulsion

There are many examples of colloidal particles presenting a specific ionization when they are suspended in a polar liquid due to the chemical constitution of their surfaces. In these cases, the colloidal particle acquires charge being surrounded by counterions (ions with opposite charge from that of the particle) and, in general, by the ions of any electrolyte present in the fluid, maintaining the electric neutrality of the suspension. The resulting scenario is a colloidal particle surrounded by an electric double layer. The overlap between double layers corresponding to two neighbour particles results in a Coulombic repulsion. Although there exist sophisticated treatments which discriminate different regions of the electric double layer [28, 29], here we will discuss an essential approximation based on the classical Poisson equation.

Let us consider the ions surrounding the colloidal particle as point charges creating a continuous charge density, $\rho(r)$, that is, a scalar function of class C^0 at each point of the space around the colloidal particle. Poisson equation is then applied to obtain the potential $\varphi(r)$:

$$\Delta\varphi(r) = -\frac{\rho(r)}{\varepsilon} \tag{2.8}$$

Where the liquid medium is only described by its electric permittivity, ε. If we consider the colloidal particle as spherical with a uniform surface charge density, the spatial dependence of the stationary problem (2.8) will rely on the radial coordinate, r. Within this framework, only a functional form for $\rho(r)$ is required to solve Equation (2.8). In this respect, it is assumed that the small ions around the colloidal particle present a motion which is rapid enough compared to that associated to the colloidal particle. Therefore, their distribution can be taken as that corresponding to a system in equilibrium, that is, Boltzmann distribution [30]:

$$\rho(r) = e_0 \sum_{i=1}^{M} z_i n_i \exp\left(e_0 z_i \varphi(r) / k_B T\right) \tag{2.9}$$

Where we assume the presence of M different species of ions, whose number densities and valences are given respectively by n_i and z_i ($i = 1,...,M$), e_0 being the elementary charge. Equation (2.8) with the functional form (2.9) is the renowned *Poisson-Boltzmann Equation*.

Due to its highly non-linear character, the Poisson-Boltzmann Equation is usually linearised to overcome analytical difficulties. In principle, the validity of this approximation is restricted to those cases in which the thermal energy, $k_B T$, is comparable to the potential energy $e_0 z_i \varphi(r)$ ($i = 1,...,M$), e.g. long distances from the colloidal particle surface. As in the Debye-Hückel theory for simple electrolytes, the exponentials in (2.9) are truncated at the first order leading the Poisson problem to an analytical solution which is well-known for different geometries of the colloidal particle surface.

In particular, the solution for the potential energy $E_{elec}(r)$ of a pair of spherical colloidal particles of radius a and equal uniform surface charge, adopts the form of a Yukawa potential energy [31]:

$$E_{elec}(r) = \frac{q_e^2}{\varepsilon r}\exp(-\kappa r) \qquad (r > 2a) \tag{2.10}$$

Where:

$$q_e = \frac{q_0}{(1+\kappa a)}\exp(\kappa a) \tag{2.11}$$

$$\kappa^2 = \frac{4\pi}{\varepsilon k_B T}\sum_{i=1}^{M} n_i (e_0 z_i)^2 \tag{2.12}$$

q_0 being the effective charge on the colloidal particle surface whereas κ^{-1}, the so-called *Debye screening length*, indicates the range of interaction. As can be seen, this range does not only depend on the charge and density of the small ions but also presents a decreasing behavior upon increasing temperature. These dependences lead to values of

κ^{-1} ranging from a small fraction of the particle radius to values which are significantly larger than a.

Despite that the acceptability of the linearised Poisson-Boltzmann Equation is restricted by the conditions $k_B T > e_0 z_i \varphi(r)$ $(i = 1,...,M)$, it is frequent to use this approximation when q_e and κ are not well characterised experimentally. In these cases, q_e and κ are regarded as fitting parameters, q_e being usually smaller than the expected prediction in case of highly-charged colloidal particles. Nevertheless, not only the linearised version of the Poisson-Boltzmann Equation but also its exact, non-linear, starting point (Equation (2.9)), present systematic predictive failures under certain conditions. We highlight here two of them:

1- The assumption of the small ions as point charges is not adequate in many experimental systems where the ratio between the size of the colloidal particle and the ions is not large enough [31].

2- The effective charge q_0 suffers an obvious alteration upon approaching two double layers. This experimental fact conditions the validity of a stationary approximation as the Poisson Equation [32].

2.2.2. London-van der Waals Attraction

Electrostatic repulsion is the main mechanism for colloidal particle stabilization. However, when the double layer around a colloidal particle is sufficiently screened until very short distances, e.g. by the addition of an electrolyte, the particles can start an aggregation process due to short-range attractive forces. Classical DLVO theory incorporates *London-van der Waals Attraction*[8] to explain this phenomenon [33].

[8] Here we clearly specify the kind of van der Waals forces discussed in this section: London-van der Waals, that is, forces between two instantaneously induced dipoles. We do not consider here Keessom-van der Waals forces between two permanent dipoles or Debye-van der Waals forces between a permanent dipole and a corresponding induced dipole.

The fluctuation of the electromagnetic fields associated to the polarisability of two molecules creates an attractive force between them due to the emergence of instantaneously induced dipoles that decreases upon increasing their distance as r^{-6}. For macromolecules (or colloidal particles), Hamaker derived an expression by the addition of any pair of molecules constituting the colloidal particles presenting an asymptotic behaviour r^{-2} and typically operating at distances of the order of a few nanometers [34][9]. The corresponding potential energy is:

$$E_{LvW} = -\frac{A}{6}\left[\frac{2a^2}{r^2-4a^2}+\frac{2a^2}{r^2}+\ln\left(1-\frac{4a^2}{r^2}\right)\right] \tag{2.13}$$

Where A, known as Hamaker's constant, depends on the polarisability of the molecules and its relation to that of the liquid medium, being negligible when both are coincident. A typical order of magnitude for A is $10^{-20}J$ [33].

Expression (2.13) does not possess a clear range of applicability since it presents a divergence at the contact ($r \to 2a$). However, it permits a good approximation at sufficiently short distances where a deep minimum appears (usually many times greater than k_BT). When distance decreases under the range of applicability of Equation (2.13), additional repulsive forces can prevent the contact (e.g. the hydration forces discussed in the next section). Finally, the sharp Born repulsion due to the overlap of the electronic clouds usually ensures the particle impenetrability. In this respect, a hard-spheres interaction, $E_{hs}(r)$, is often added to the classic DLVO theory implementing this last repulsion:

$$E_{hs}(r) = \begin{cases} \infty & (r \le 2a) \\ 0 & (r > 2a) \end{cases} \tag{2.14}$$

[9] Here r is the center-center separation between two macromolecules.

2.2.3. Hydration Forces

When colloidal particles have a surface with a certain degree of hydrophility, a new non-classical DLVO interaction appears. This interaction is usually understood in terms of a hydration energy which is generally repulsive [33, 35-37]. The earliest explanation of this hydration or structural force came in the 1970´s, when it was attributed to the strongly bound liquid molecules (e.g. water) on the colloidal particle surface [35]. Accordingly, the liquid would form an oriented layer around the colloidal particle inducing an effective repulsion when two particles became sufficiently close. However, this is not the only plausible explanation since the local variation of the dielectric permittivity in the electric double layer [36] or the entropic repulsion arising from the confinement of thermally mobile surface groups would also provide a satisfactory interpretation [37]. Thus, a definite understanding of the hydration interaction still remains elusive. Due to its complexity, it seems that more sophisticated experiments as well as computer simulations should be considered over the following years to give us new insight on this phenomenon. In the meantime, some authors as Okhi and Arnold have proposed semi empirical expressions [38-40] to explain experimental results with a certain level of success. In their model, they define a hydrophobic index, p, that represents the degree of hydrophobicity of the surface [39]. Thus, the hydration energy would be purely repulsive when the surface is hydrophilic and tends to be completely hydrated ($p = 0$) whereas the interaction would be attractive when the surface is hydrophobic and then it is completely dehydrated ($p = 1$).

Their ansatz for the hydration energy per unit area is:

$$E_h(R) = (1-p)P_0 l \exp(-R/l) + pP_0' l' \exp(-R/l') \qquad (2.15)$$

Here R represents the separation distance between the surfaces of two colloidal particles, P_0 (>0) and P_0'(<0) are constants having the dimension of pressure whereas l and l' are decay rates indicating the range of the hydration repulsion and attraction respectively (usually of the order of a few Ångströms).

Within this dissertation, the significace of $E_h(R)$ will be obvious in the aggregation processes of liposome suspensions mediated by divalent cations (see Paper IV). However, instead of using an analytical approximation as (2.15), we will show experimental results on the effective dehydration exerted by some metallic cations on the superficial lipid headgroups.

2.2.4. Hydrodynamic Forces

There are different notions under the appellative of *Hydrodynamic Forces*. In principle, by hydrodynamic forces we can understand any transfer of momentum between a colloidal particle and its surrounding liquid. In this respect, the Brownian interaction described in section 2.1 will belong to that category. However, when colloidal particle concentration is increased it can appear a new hydrodynamic component. Let us discuss briefly this interaction.

By virtue of Newton's third law, the liquid interacting with a mesoscopic particle receives a momentum transfer from the particle which is equal in magnitude to that received by the particle. If particle concentration is large enough, this perturbation in the fluid will be transmitted reaching the neighbour particles and appearing a new force, which is not strictly Brownian, with the fluid as propagating medium[10]. This interaction

[10] The range of this hydrodynamic interaction can be often of the order of a fraction of the colloidal particle radius [31].

will depend at any instant on the mechanical state of the system (position and velocities of the particles) as well as on the transport coefficients of the liquid medium (e.g. viscosity). This phenomenon is often described by a generalization of the Langevin Equation [31]:

$$m_i \frac{d\vec{v}_i(t)}{dt} = -\sum_{i=1}^{N} \beta_{ij}(\vec{r}^{\,N}(t)) \cdot \vec{v}_j(t) + \vec{F}_i(t) \tag{2.16}$$

N being the number of colloidal particles, m_i the mass of particle i, $\vec{v}_i(t)$ its velocity at time t and $\vec{F}_i(t)$ is the three-dimensional version of the Gaussian white noise referred in section 2.1. Now the friction coefficient in Langevin Equation becomes a tensor, $\beta_{ij}(\vec{r}^{\,N}(t))$, depending on the instantaneous particle configuration, $\{\vec{r}^{\,N}(t)\}$. Again, we can take advantage of Newton's third law to ensure the symmetry of β_{ij} [11].

Nevertheless, it is difficult to find an analytic expression for β_{ij}. For that reason, authors such as Beenakker and Mazur have described the effect of the hydrodynamic interaction in simple terms for a suspension of hard spheres by means of a semi empirical correction of the free diffusion coefficient present in section 2.1 that depends on the particle volume fraction, ϕ [41]:

$$D_{eff} = D_0\left(1 + 1.56\phi + 0.91\phi^2\right) \tag{2.17}$$

Now D_{eff} is the effective particle diffusion coefficient. Thus, the effect of the hydrodynamic forces is manifested through the inequality $D_{eff} > D_0$ as a slowing down of the motion with respect to the free diffusion.

[11] In case of dilute systems, where the hydrodynamic forces between the colloidal particles are negligible, β_{ij} recovers its diagonal form and the Equations (2.16) become uncoupled, that is, we recover the Langevin Equation (2.1).

Chapter 3

Structure: General Concepts

The previous Chapter was dedicated to the discussion of the most relevant interactions present in a suspension of colloidal particles, that is, liquid-particle and particle-particle interactions. These interactions have two coupled manifestations, one concerning the dynamics, whereas the other, is manifested through the static spatial correlations between particles. This latter effect is commonly known as *Structure* being classically described in terms of ensemble averages of functions that involve correlations between two or more particles.

3.1. Pair Correlations

In classical Statistical Mechanics the configurational space of a system of N particles is weighted by an ensemble probability distribution $P(\vec{r}^{\,N})$, that is, a joint distribution for finding the system at the state $\{\vec{r}^{\,N}\}=\{\vec{r}_1,...,\vec{r}_N\}$, where $\vec{r}_i$ is the position of the particle labelled as i. Under equilibrium conditions, this distribution is stationary for any ensemble, in particular for that represented by the canonical ternary set $\{N,V,T\}$, V being the volume of the system.

In the case of indistinguishable particles, we can reduce our description to a correlation between any pair of particles by means a generic distribution, $\rho^{2/N}(\vec{r}_1,\vec{r}_2)$, that is, a joint distribution for finding any particle of the system at position $\vec{r}_1$ and any other at position $\vec{r}_2$ [42]:

$$\rho^{2/N}(\vec{r}_1,\vec{r}_2)=N(N-1)\frac{\int_{\Omega} d\vec{r}_3...d\vec{r}_N P(\vec{r}^{\,N})}{\int_{\Omega} d\vec{r}_1...d\vec{r}_N P(\vec{r}^{\,N})} \tag{3.1}$$

Where the rest of the particles can be at any position of the configurational space, Ω, $N(N-1)$ being the possible assignations between particles and positions. We can go further by assuming that space is homogeneous, that is, there are not privileged positions. Under this assumption, the generic distribution for an ideal system, a system with no interaction between particles, takes the form:

$$\rho_{ideal}^{2/N}(\vec{r}_1,\vec{r}_2) = N(N-1)/V^2 \underset{\substack{\text{V,N}\to\infty,\ \text{V/N}\to\text{constant}\\ \text{(Thermodynamic limt)}}}{\longrightarrow} \rho^2 \tag{3.2}$$

ρ being the density of our system. If space is also isotropic, that is, there are not privileged directions, we can define the *radial distribution function,* $g(r = |\vec{r}_2 - \vec{r}_1|)$, as:

$$g(r) \equiv \rho^{2/N}(\vec{r}_1,\vec{r}_2)/\rho^2 \tag{3.3}$$

Thus, by $g(r)$ we establish the correlation between any pair of particles separated by a distance r with respect to that corresponding to an ideal system. Some simple considerations are pertinent:

1- $\rho g(r)$ is the mean density of particles at a distance r from a given particle with respect to the mean density ρ.

2- If correlation is lost upon increasing r, then we have $g(r\to\infty)=1$.

3- Definition (3.3) is supported by three essential assumptions: particle indistinguishability, space homogeneity and space isotropy.

The experimental accessibility to the pair correlations in a system of colloidal particles usually comes from directly measurable functions in Fourier space instead of real space.

To establish the connection between these functions and those defined above, let us consider an alternative way to express the generic distribution $\rho^{2/N}(\vec{r},\vec{r}')$ [43]:

$$\rho^{2/N}(\vec{r},\vec{r}') = \left\langle \sum_{i\neq j}^{N} \delta(\vec{r}-\vec{r}_i)\delta(\vec{r}'-\vec{r}_j) \right\rangle \tag{3.4}$$

Where $\delta(\vec{r})$ is the delta distribution whereas $\langle\ \rangle$ denotes the ensemble average. Equivalently, the *local particle density* at position $\vec{r}$ can be expressed as:

$$\rho(\vec{r}) = \sum_{i=1}^{N} \delta(\vec{r}-\vec{r}_i) \tag{3.4}$$

Any Fourier component, $\rho_{\vec{k}}$, of the local density is then given by:

$$\rho_{\vec{k}} = \int \exp\left(-i\vec{k}\cdot\vec{r}\right)\rho(\vec{r})d\vec{r} = \sum_{i=1}^{N} \exp\left(-i\vec{k}\cdot\vec{r}_i\right) \tag{3.5}$$

Where its autocorrelation function is the so-called *Static Structure factor*[12]:

$$S(\vec{k}) = \frac{1}{N}\left\langle \rho_{\vec{k}}\rho_{-\vec{k}} \right\rangle \tag{3.6}$$

We can conveniently develop expression (3.6) to rewrite the static structure factor in terms of the radial distribution function for homogeneous and isotropic suspensions [43]:

$$S(\vec{k}) = \frac{1}{N}\left\langle \sum_{i=1}^{N}\sum_{j=1}^{N} \exp\left(-i\vec{k}\cdot\vec{r}_i\right)\exp\left(i\vec{k}\cdot\vec{r}_j\right) \right\rangle =$$

[12] Vector $\vec{k}$ in Fourier space will correspond to the scattering vector in the scattering experiments shown in this dissertation (see Papers I-V).

$$
\begin{aligned}
&= 1 + \frac{1}{N}\left\langle \sum_{i \neq j}^{N} \exp\left(-i\vec{k}\cdot(\vec{r}_i - \vec{r}_j)\right)\right\rangle \\
&= 1 + \frac{1}{N}\left\langle \sum_{i \neq j}^{N} \iint \exp\left(-i\vec{k}\cdot(\vec{r} - \vec{r}')\right)\delta(\vec{r} - \vec{r}_i)\,\delta(\vec{r}' - \vec{r}_j)\,d\vec{r}\,d\vec{r}'\right\rangle \\
&= 1 + \frac{1}{N}\iint \exp\left[-i\vec{k}\cdot(\vec{r} - \vec{r}')\right]\rho^{2/N}(\vec{r},\vec{r}')\,d\vec{r}\,d\vec{r}'
\end{aligned}
\tag{3.7}
$$

Where $g(\vec{r})$ is given by the trivial vector generalization of expression (3.3). Conversely we have:

$$
\rho g(\vec{r}) = \frac{1}{(2\pi)^3}\int \exp\left(i\vec{k}\cdot\vec{r}\right)\left[S(\vec{k}) - 1\right]d\vec{k} \tag{3.8}
$$

Finally, if the system is isotropic:

$$
\begin{aligned}
S(k) &= 1 + 2\pi\rho\int r^2 g(r)\int_{-1}^{1}\exp(-ikr\cos\theta)\,d(\cos\theta)\,dr \\
&= 1 + 4\pi\rho\int r^2 g(r)\frac{\sin kr}{kr}\,dr
\end{aligned}
\tag{3.9}
$$

Within this dissertation, the connection given by expression (3.9) as well as the experimental determination of the static structure factor will be widely relevant (see Papers III, IV, and V).

3.2. Point-to-set Correlations

The structural description given by the radial distribution function and its counterpart in Fourier space, the static structure factor, does not only apply to colloidal suspensions but also to classic molecular liquids. In this second case, temperature usually plays an equivalent role as external parameter as volume fraction does in the case of a suspension of colloidal particles.

A phenomenon of special interest, present in both molecular liquids and colloidal suspensions, is the emergence of a glassy "state"[13] when temperature reaches a sufficiently low value or, in the case of colloidal suspensions, when volume fraction is sufficiently increased [44] (see Chapter 5 and Papers V and VI). Under the point of view of the classical pair correlation functions, the microscopic structure of a system near the glassy state does not reveal a significant difference with that associated to a normal liquid despite these systems behave as solidlike materials [44-46]. However, near the *Glass Transition* (GT), a small change in the static structure of a glass-forming liquid (seen by means of the classical pair correlations functions) induces a dramatic change in the system relaxation dynamics. This experimental fact is usually accounted for by the idea of *structural relaxation* [46].

Within this dissertation, a more complete study of some essential features of the GT phenomenon will be discussed experimental and theoretically not only for colloidal suspensions but also for molecular liquids (see again Chapter 5 and Papers V and VI). Nevertheless, we can now anticipate a long standing conundrum behind the structural description of a glass: Is the description of a glass offered by the classical pair correlation functions complete? If the answer is negative: Can we define new static observables showing a spatially increasing structure, different from that of a normal liquid, upon approaching the GT? The emergence of the so-called *point-to-set correlation functions* is focused at the heart of these questions. With them, it is attempted to reveal the structure that, in principle, would be invisible for the classic static observables.

As a way of example, let us consider the radial distribution functions obtained by a molecular dynamics simulation and corresponding to the binary mixture of quasi-hard spheres considered in Paper VI, where the interaction potential is given by $V(r) = 1/2(r-\sigma)^2$ (σ being the range of interaction, i.e. "the particle diameter"). As can be seen in Figure 3.1, the envelopes of the radial distribution functions at different

[13] Here the word "state" appears between quotations marks since the existence of a true glass state still remains elusive (see Chapter 5 and Paper VI).

temperatures decay with a similar exponential rate, ξ, that is, structure does not propagate further upon approaching the GT despite the relaxation times, t_α, present a significant change[14]. Thus, the classical structural description presented in Fig. 3.1 given by $g(r)$ does not show, at least trivially, any evidence of a static correlation length divergent at the glass transition temperature. However, as we will discuss in Chapter 5, there exist thermodynamic arguments supporting the emergence of an increasing static correlation length accompanying the GT [47].

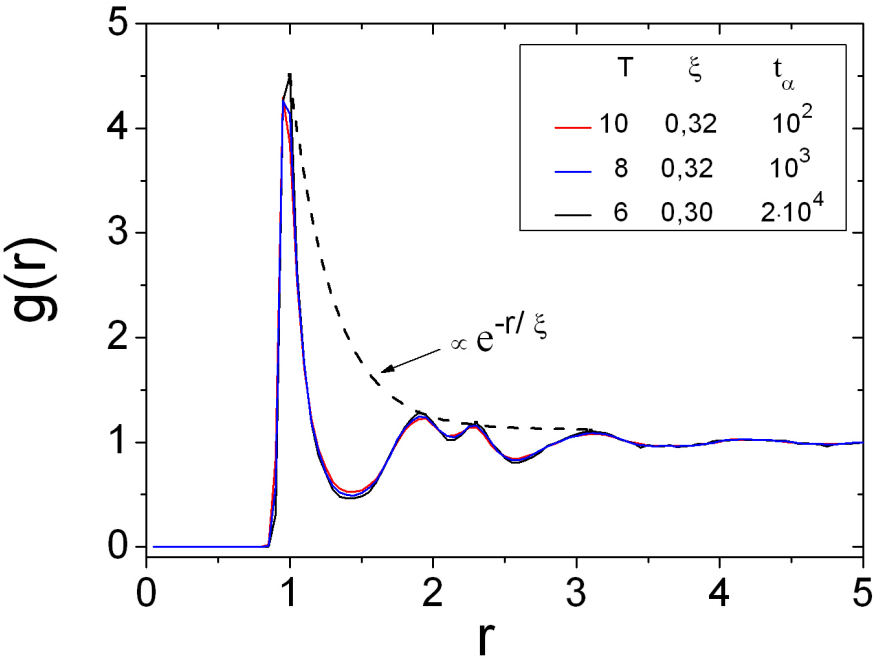

Figure 3.1: Radial distribution functions for a system of elastic spheres (see Paper VI). The glass transition temperature is placed around $T_g = 4.5$. Units for temperature, time and length are conveniently normalized according to the mass, diameter and mean energy of the particles.

To shed light on this puzzle, computer experiments have been proposed to explore the effect of boundary conditions on the structure of a glass-forming liquid [48, 49] (see Chapter 5, section 5.2). On one hand, the boundaries are formed by frozen particles of the studied liquid in an amorphous configuration, acting as pinning fields that "hold"

[14] A formal definition of the relaxation time t_α is presented in Refs. [44-46] and Chapter 5 (section 5.1).

the structure of the unfrozen (liquid) part of the system. On the other hand, to investigate the structure of the liquid, appropriate *multipoint* static correlation functions are introduced to quantify the similarity between local configurations.

One of the main candidates for a *point-to-set* correlation function is constructed as follows [47]: We divide the liquid part of the system in cells, that is, we construct a grid. Each cell will have an occupation number, $n = 1 \text{ or } 0$, according to whether or not the cell is occupied by a particle. Thus, the initial configuration associated to a given region, R, of the liquid will be specified by a set of occupation numbers, $\{n_i : i = 1,..., \text{Number of cells in } R\}$. Now, we proceed in the same way at the long time limit, that is, we assign a new set of occupation numbers to the region R. Finally we measure the overlap, O_R, between these two local configurations separated by a long time as:

$$O_R = \left[\frac{1}{\text{Number of occupied cells at } t = 0} \sum_{i=1}^{\text{Number of cells in } R} \langle n_i(0) n_i(t \to \infty) \rangle \right]_{boundary} \tag{3.10}$$

Here $[\ ]_{boundary}$ denotes an additional average over equivalent but independent frozen boundary realizations. By definition, the larger is the overlap the greater will be the remaining similarity between local configurations.

It is clear that this new observable measures the correlation between a point (cell) and a set of particles (the frozen boundary). For that reason, O_R is considered as a point-to-set correlation function instead of a point-to-point correlation despite both deal with density fluctuations. In Paper VI, we will discuss how, by using this new observable, we can define a static length which increases upon approaching the GT. Thus, the overlap, as point-to-set correlation function, will carry static information which is not contained in the classical pair correlation functions.

Chapter 4

Aggregation: Structure and Kinetics

"*How long is the coast of Britain?*"
B. Mandelbrot[15]

In Chapter 3 we have defined appropriate observables to describe the structure of colloidal suspensions. These suspensions can either be stabilised (e.g. by means of a Coulombic repulsion) or, on the contrary, develop an aggregation process where the particles become stuck (e.g. by virtue of London-van der Waals attraction, see Chapter 2, section 2.2.2). Here we will present the theoretical fundamentals to account for the kinetics of such aggregation processes as well as the structure of the resulting aggregates. This structure is often satisfactorily pictured by the notion of *Fractal*.

4.1. Fractals

Since 1977, when Benoît Mandelbrot left to posterity his book "*The Fractal Geometry of Nature*" [51], the interpretation of natural phenomena in terms of fractal representations has been ubiquitous. In particular, literature where the notion of fractal is applied to aggregated colloidal systems is huge (see for instance [52-54]). Before discussing this specific application, we will first introduce the concept of fractal.

Let us consider a set, A, of a metric space[16] and the covering of this set with the minimal number $N(r)$ of balls[17] of radius r providing that any point of the set is

[15] See Ref. [50].
[16] Although the adjective "metric" only implies the definition of a distance, from now on we will consider as particular case the Euclidean space, E^3, where the distance is given by the Euclidean metric or, in old literature, the Pythagorean metric.
[17] We take as definition of a *ball* of radius r that set of points whose Euclidean distance from a given center does not exceed a prescribed radius r.

included in at least one of the balls. It is clear that with decreasing r the number $N(r)$ grows in general in a nontrivial fashion. If the covering process of A satisfies the existence of the limit:

$$\lim_{r\to 0} -\frac{\log N(r)}{\log r} = D \quad (D \in [0,3]), \tag{4.1}$$

we will call, D, the *Entropy dimension* or, informally, the *Hausdorff dimension* of A, for which non-integer values are permitted. In particular, we call *Fractal* to a set whose Hausdorff dimension is strictly greater than its topological dimension[18] [51]. In this case, D is, roughly speaking, the *Fractal dimension*.

Excursus

The limit (4.1) offers the Hausdorff dimension of a set A of a metric space in almost all cases (in particular, those cases explored within this dissertation) [51]. However, as Hawkes demonstrated [56], the equality between D, given by expression (4.1), and the strict definition of the Hausdorff dimension does not always hold.

To reach a general notion of fractal, that is, a set whose Hausdorff dimension is strictly greater than its topological dimension, we have to consider the formal definition of the Hausdorff dimension [51]. Thus, the *d -dimensional Hausdorff content*, $C_H^d(A)$, of a set A of a metric space is defined by:

$$C_H^d(A) \equiv \text{infimum}\left\{\sum_i r_i^d : \text{There is a cover of } A \text{ by balls of radii } r_i > 0\right\} \tag{4.2}$$

[18] The topological dimension or *Levesgue covering dimension* of a set is an integer m if for every open cover of that set there is an open cover that refines it such that the refinement has order $m+1$ at most [55]. In this respect, the "irregularity" of a fractal results in a Hausdorff dimension (by ball covering) greater than the topological dimension (by open covering). Mandelbrot remarked this intrinsic irregularity through the creation of the word fractal as follows: "I coined *fractal* from the Latin adjective *fractus.* The corresponding Latin verb *frangere* means "to break", to create irregular fragments. It is therefore sensible- and how appropriate for our needs!- that, in addition to "fragmented" (as in *fraction* or *refraction)*, *fractus* should also mean "irregular", both meanings being preserved in *fragment*." [51]

Then, the Hausdorff dimension of A is defined as the infimum of the set of $d \in [0,\infty)$ such that the d-dimensional Hausdorff content of A is zero [51].

4.2. Surface and Mass Fractals: Definitions

In a seminal investigation, Pfeifer and Avnir proposed the application of the fractal theory to characterize heterogeneous chemical surfaces [57]. In their work, the degree of irregularity (or "roughness") was identified by a real number $D \in (2,3)$ according to the limit (4.1), where they considered the ball covering of the surface in three-dimensional space. A surface belonging to that category was called *Fractal Surface*, D being the so-called *Surface Fractal dimension*.

As particular case, we can consider those closed fractal surfaces which define the boundary of a completely compact three-dimensional object (a "walnut" as Martin and Hurd called it [53], see figure 4.1). The resulting geometrical object is now called *Surface Fractal*, having a surface fractal dimension D. Thus, specifically a surface fractal will define a closed fractal surface (see for details Ref. [58]).

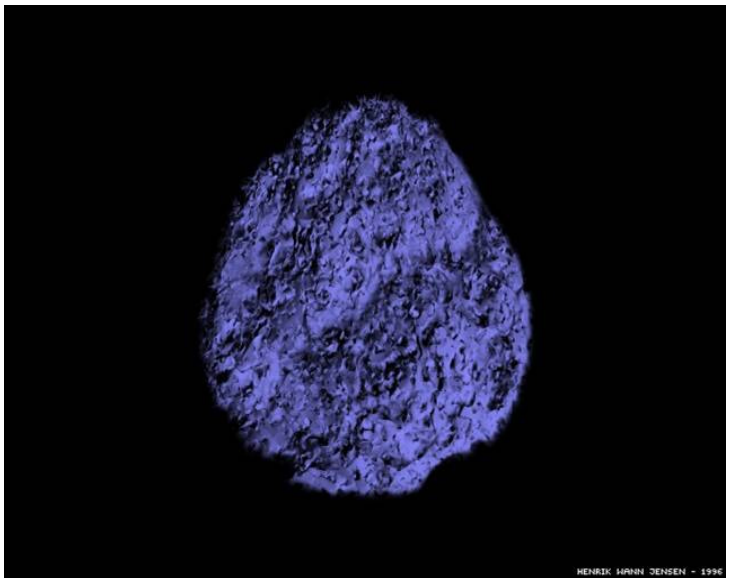

Figure 4.1: "Fractal Egg" as intuitive example of Surface Fractal (reproduced with permission from [59]).

The surface fractal dimension can also be conviently defined if we associate a distinctive length to our surface fractal, e.g., its radius of gyration, R. Then, we obtain an equivalent expression for (4.1) if the surface fractal is expanded by a growth factor, keeping constant the radius of the covering balls. Thus, asymptotically $(R \to \infty)$:

$$S = KR^D \quad (2 < D < 3) \tag{4.3}$$

Where S is the surface that covers the surface fractal, K being a positive real number. Now, from $D \to 2$ (limit of a completely smooth surface), the irregularity of a surface fractal increases upon increasing D (see Paper IV).

This process can be extended by definition to the covering of the volume of a three-dimensional object which in general will not be completely compact, that is, it can be a "ramified" structure. Thus, starting from an inner point, we will cover again the object by increasing R, where we will remain always inside the object. The resulting structure is called V*olume* or *Mass Fractal* if the covering volume, V, scales as [53]:

$$V \propto R^D \quad (0 < D < 3) \tag{4.4}$$

D, the so-called the *Mass Fractal dimension*, will identify the "compactness" of the mass fractal: From $D \to 3$ (limit of a uniform or completely compact object), the compactness of a mass fractal decreases with decreasing D.

From the previous definitions, it is obvious that two different surface fractals show only different properties on their boundaries, that is, they have different surface fractal dimension. However their uniform interiors will present an equivalent fractal description.

Thus, to discrimitate between surface and mass fractals, we will note by $d_s = D$, the fractal dimension corresponding to definition (4.3) and by $d_m = D$ (or simply d_f, see Paper III) when it corresponds to (4.4). With this notation, a surface fractal will be characterized by $2 < d_s < 3$ and $d_m = 3$ [19].

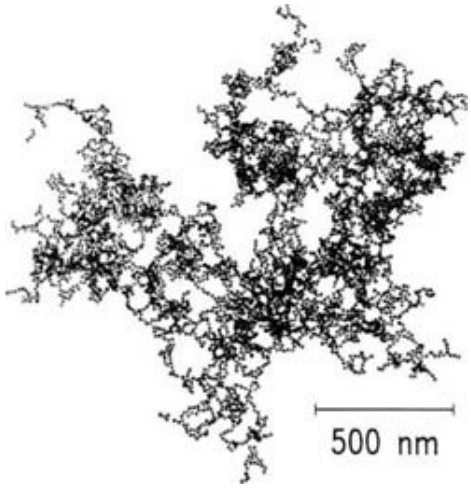

Figure 4.2: Example of a Mass Fractal aggregate of gold particles with radius $a = 7.2 \pm 0.7$ nm and obtained under DLCA conditions (see section 4.4 of this Chapter, Brownian kernel). The experimental mass fractal dimension is $d_m = 1.74$ (reproduced with permission from [60]).

4.3. Surface and Mass Fractals: Connection with Static Observables

Let us start this section with a question: How is the fractal structure of a system of colloidal aggregates manifested when it is examined through the classical static observables? To answer this question, we will next establish the criterion to test the fractal geometry of an aggregate by means of its radial distribution function.

[19] The equality $d_m = 3$ should be understood as a licence to gain intuition on the notion of Surface Fractal, i.e. a compact object ($d_m \to 3$) with $2 < d_s < 3$. We have to remember that, formally speaking, d_m defined by (4.4) is reserved for mass fractals, that is, objects with $d_m < 3$.

We say that an object is *non-trivially scale-invariant* [61] if the radial distribution function describing the structure of this object satisfies:

$$g(br) = b^{-\gamma} g(r) \tag{4.5}$$

Where b and γ are positive real numbers. It is obvious that Expression (4.5) imposes a degree of homogeneity, γ, (not necessarily integer) to the radial distribution function:

$$g(r) \propto r^{-\gamma} \tag{4.6}$$

Using the definition of the radial distribution function (Expression (3.3)) we obtain the mass of the object, whose growth from an inner point (our origin) to a given distance R (remaining inside the object) is governed by γ:

$$M = \int_0^R \rho g(r) d^3 r \propto R^{3-\gamma} \tag{4.7}$$

Identifying (4.7) with (4.4), we partially answer the question posed at the beginning of this section. That is:

$$g(r) \propto r^{d_m - 3} \tag{4.8}$$

Hence, Expression (4.8) is the manifestation of a mass fractal through its radial distribution function. Nevertheless, this result does not consider the finite size of a real object. In that case, we should contemplate an extended expression for (4.8) where the limits of the object are considered [61]:

$$g(r) \propto r^{-\gamma} f(r / R_{obj}) \tag{4.9}$$

Here R_{obj} is the characteristic radius of the real object and $f(x)$ a cut-off function which describes its surface. In general, this "surface" function should satisfy:

$$f(x) = \begin{cases} 0 & x >> 1 \\ 1 & x << 1 \end{cases} \tag{4.10}$$

In the case of surface fractals (where $\gamma = 0$ or $d_m = 3$)[20], the fractal nature of the surface relies on the functional form of $f(x)$. This functional form depends in general on the growing mechanism by which the surface was created (for more details, see [57, 61]). Here we merely consider one of these theoretical approximations, widely applied to real systems, through its manifestation in terms of its representation in Fourier space, that is, through the static structure factor.

As anticipated in Chapter 3 (section 3.1), the direct experimental accessibility to the structure of a system of colloidal particles usually comes from the determination of the static structure factor. By virtue of Equation (3.9), the fractal nature of a structure is also proved by a power law dependence of $S(q)$ within the spatial range limited by the structure, that is, within a given q range[21].

Thus, if a structure presents fractal nature between two characteristic lengths, a power law dependence of $S(q)$ is expected when q^{-1} is included between these characteristic lengths[22]. In this respect, and in order to test the fractal nature of rough surfaces, Bale and Schmidt [62] were the first to propose a functional behavior for $S(q)$ (and then for $f(x)$), applying their model to the study of lignite coal. Similarly, and starting from the seminal work of Schaefer and co-workers [63], several experimental studies have been performed in order to prove the structure of mass fractals through $S(q)$.

[20] See footnote 19.

[21] Within this dissertation we will indistinctly use k or q for the modulus of a vector in Fourier space (see Chapter 3).

[22] By definition, q^{-1} plays the role of an inherent length scale in real space [54].

A compendium of their results is:

$$S(q) \propto q^{-\alpha} \tag{4.11}$$

Where:

$$\alpha = \begin{cases} d_m & \text{(Mass Fractals)} \\ 2d_m - d_s = 6 - d_s & \text{(Surface Fractals)} \end{cases} \tag{4.12}$$

A common case proved on real systems (see Papers III and IV) is that which corresponds to fractal structures of representative radius R formed by subunits (colloidal particles) of radius a. Thus, as mentioned above, Expression (4.11) will be typically satisfied within the range $R^{-1} << q << a^{-1}$.

4.4. Aggregation Kinetics: Smoluchowski's Model

In previous sections we have introduced the essential concepts to describe the structure of colloidal aggregates when they present fractal nature. Our purpose now is to illustrate by a simple model the time evolution of an aggregation process from the initial state, where the particles are regarded as individual entities, to the state at which they form well defined fractal structures. This model will depend at any time not only on the frequency distribution of particles forming the aggregates but also on the fractal structure of these aggregates.

When we consider an aggregating colloidal suspension which is sufficiently diluted, the aggregation process can be understood schematically as a set of binary reactions in the form[23]:

$$A_i + A_j \leftrightarrow A_{i+j} \tag{4.13}$$

[23] A criterion concerning the validity of a binary reaction model in terms of the particle concentration is given in Ref. [64]. Taking as basis this investigation, we will consider the binary assumption as valid when the monomer volume fraction below 1%.

Where A_i represents an aggregate constituted by i monomers (primary particles). The scheme (4.13) can be complemented by the assumption of a proportionality between the increment per unit time of the $(i+j)$-particle aggregates with those constituted by i and j particles:

$$\frac{dN_{i+j}(t)}{dt} \propto N_i(t)N_j(t) \tag{4.14}$$

Where now $N_i(t)$ is the absolute frequency, that is, the absolute number of the i-particle aggregates at time t. If we additionally admit no fragmentation[24], that is, $A_i + A_j \rightarrow A_{i+j}$, a time evolution model for the cluster size distribution, $\vec{N}(t) = (N_1(t), N_2(t), ...)$, arising in an aggregating system is given by the *Smoluchowski Rate Equations* [67, 68]:

$$\frac{dN_n(t)}{dt} = \frac{1}{2}\sum_{i+j=n} k_{ij}N_i(t)N_j(t) - N_n(t)\sum_{i=1}^{\infty} k_{in}N_i(t) \quad ; \quad \forall n \in \mathrm{N}^* \tag{4.15}$$

Where the set of rates k_{ij} $(\forall i, j \in \mathrm{N}^*)$[25], usually known as *kernel*, contains the whole kinetic information through its mass (number of monomers) and geometry cluster dependences. Thus, from a given k_{ij} and an initial condition, $\vec{N}(0) = (N_1(0), N_2(0), ...)$, Equations (4.15) provide a continuous set of frequencies, $\vec{N}(t)$. As anticipated by Equation (4.14), the first term of the right side in (4.15) gives the increment per unit time of $N_n(t)$ due to the reactions $i + j = n$, whereas the second term gives the loss per unit time of $N_n(t)$ due to the formation of clusters with $i + n$ monomers[26].

[24] Literature concerning fragmentation effects is wide (see for instance [65, 66]).

[25] We adopt the convention for the set of the natural numbers by which $0 \in \mathrm{N}$. Then $N^* = N \setminus \{0\}$.

[26] There is a subtlety involved in the factor 1/2 in the Equations (4.15): On one hand, if $i \neq j$, we compute only the reactions $i + j = n$ but not $j + i = n$. On the other hand, if $i = j$, the reaction $i + i$ is slower by a factor 1/2 than that corresponding to the loss of $N_i(t)$ [69].

Apart from these considerations, it is worthwhile to mention two of the inherent assumptions contained in the Equations (4.15):

1- The set of Equations (4.15) describes an aggregation process as a purely deterministic phenomenon, that is, for a given initial condition, $\vec{N}(0)$, $\vec{N}(t)$ is completely specified.

2- The average cluster size diverges with time due to the non-fragmentation assumption.

Equations (4.15) can be conveniently normalized to restate the problem in a non-dimensional form:

$$\frac{dX_n(T)}{dT} = \frac{1}{2}\sum_{i+j=n} K_{ij} X_i(T) X_j(T) - X_n(T)\sum_{i=1}^{\infty} K_{in} X_i(T) \quad ; \quad \forall n \in \mathrm{N}^* \tag{4.16}$$

Here $X_n(T) \equiv N_n(T)/N_1(0)$, $K_{ij} \equiv 2k_{ij}/k_{11}$, and $T \equiv t\left(N_1(0)k_{11}/2\right)$. Where we can associate a characteristic time to our aggregation process corresponding to $T = 1$ or, equivalently, $t_{agg} \equiv 2/N_1(0)k_{11}$. This is the so-called *Aggregation Time*. A simple inspection in (4.15) tell us that this time would be the hypothetical time at which all the initial monomers would become dimers (2-particle aggregates) if only this kind of reaction were allowed[27].

The existence of an explicit solution for the set of Equations (4.16) depends on the chosen kernel. Although, in general, the integration of (4.16) will need the use of numerical calculation, there are kernels with a special physical meaning for which an explicit solution is known. These kernels do not only provide a good approximation to describe real aggregation processes but also constitute a convenient tool for testing the accuracy of numerical calculations involving kernels without explicit solution (see Appendix A). In this respect, we will present three examples of kernels widely studied

[27] The factors 2 and 1/2 in $K_{ij} \equiv 2k_{ij}/k_{11}$ and $T \equiv t\left(N_1(0)k_{11}/2\right)$ are obviously unnecessary to obtain the normalized version of Expression (4.15). In fact, the definition of T includes the factor 1/2 to fix the aggregation time at T=1. Consequently, the factor 2 in $K_{ij} \equiv 2k_{ij}/k_{11}$ leads us to Expression (4.16).

in literature whose solution is known. For further discussion, the reader can consult the advisable review by Leyvraz [70].

1- Constant kernel

$$K_{ij} = 2 \quad \forall i, j \in \mathrm{N}^* \tag{4.17}$$

This simple kernel, for which all the reactions present the same weight, provides an accurate description, especially at short times, for those aggregation processes governed by diffusion (see Paper IV). Although its explicit solution is known for any arbitrary initial condition [70], here we present that corresponding to monomeric initial conditions, which was originally derived by Smoluchowski [67]:

$$X_n(T) = \frac{T^{n-1}}{(1+T)^{n+1}} \;\; ; \;\; \vec{X}(0) = (1,0,0,...) \;\; ; \;\; \forall n \in \mathrm{N}^* \tag{4.18}$$

2- Sum kernel

$$K_{ij} = i + j \quad \forall i, j \in \mathrm{N}^* \tag{4.19}$$

For monomeric initial conditions [71]:

$$X_n(T) = \frac{(nb)^{n-1} e^{-nb-T}}{n!} \;\; ; \; b \equiv 1 - e^{-T} ; \; \vec{X}(0) = (1,0,0,...) ; \forall n \in \mathrm{N}^* \tag{4.20}$$

3- Product kernel

$$K_{ij} = ij \quad \forall i, j \in \mathrm{N}^* \tag{4.21}$$

This kernel presents a remarkable signature since its solution leads us to the formation of an infinite aggregate at a finite time $T = 1/2$. This singularity has been interpreted in terms of a sol-gel transition [72].

Although there are studies including the solution for times $T > 1/2$ [72], we only present here that restricted to the hypothetical sol phase [73]:

$$X_n(T) = \frac{(2nT)^{n-1} e^{-2nT}}{nn!} \quad ; \; T \leq \frac{1}{2} \; ; \; \vec{X}(0) = (1,0,0,...) \; ; \; \forall n \in \mathrm{N}^* \tag{4.22}$$

The sol-gel transition can be accounted for by a non-conservation of the mass of the system, $M(T)$, which is normalized to unity for our relative frequencies, that is, $M(T) = \sum_{i=1}^{\infty} nX_n(T) = 1$. In systems where the distribution $X_n(T)$ decreases smoothly (e.g. as a power law) mass decreases. This decrease in the mass of the system is interpreted in terms of a flux of mass out of the system to an aggregate of infinite size: The "gel". In this respect, Equation (4.22) presents a power law behaviour for $T = 1/2$, $X_n(1/2) \propto n^{-5/2}$, which indicates the emergence of the gel phase[28] [72].

Brownian Kernel

One of the essential aggregation processes is that corresponding to the binary aggregation of two Brownian particles or aggregates whose motion is purely diffusive. Thus, when two aggregates, driven by Brownian motion, are sufficiently close[29] they become stuck by a short range attraction (e.g. London-van der Waals) and form a new aggregate.

This kind of aggregation process is known as *Diffusion Limited Cluster-Cluster Aggregation* (DLCA). Formally, one of the aggregates (cluster) is considered as a sink whereas the other is subjected to Brownian motion, having a diffusion coefficient which is the sum of the two aggregates diffusion coefficients, $D_i + D_j$.

[28] $X_n(1/2) \propto n^{-5/2}$ is obtained by using Stirling's approximation: $n! \approx \sqrt{2\pi n}(n/e)^{-n}$ ($n \to \infty$).

[29] In the light of the Brownian kernel model, "sufficiently close" means "geometric contact".

Then, a primitive expression of the so-called *Brownian kernel* for two aggregates formed by i and j monomers with radii of gyration R_i and R_j respectively, is [74]:

$$k_{ij}^{Br} = 4\pi\left(D_i + D_j\right)\left(R_i + R_j\right) \tag{4.23}$$

First, we note that the diffusion coefficient, D_i, can be expressed in terms of the hydrodymanic radius, R_i^h, by virtue of Stokes-Einstein relation. As second hypothesis, experimentally supported [75], we can consider that the hydrodynamic radius, which is a dynamic observable, equals the radius of gyration, which is a purely geometrical concept. Finally, we use the definition of the mass fractal dimension to obtain $R_i = ai^{1/dm}$, a being the monomer radius. With these assumptions, the Brownian kernel results:

$$k_{ij}^{Br} = k^{Br}\left(i^{1/dm} + j^{1/dm}\right)\left(i^{-1/dm} + i^{-1/dm}\right) \quad ; \quad k^{Br} \equiv 8k_B T / 3\eta \tag{4.24}$$

Since DLCA regime is given by well defined assumptions, it seems pertinent to ask if the resulting mass fractal dimension has also a well defined value. Experimental results [76] and theoretical simulations [77] seem to answer this question in a positive way, where $d_m \cong 1.75$. However, a mathematical proof supporting this result is still elusive. As a way of example, Figure 4.3 shows, using the Brownian kernel with $d_m = 1.75$, the time evolution of those clusters formed by 1 to 7 monomers, where Equation (4.16) was solved numerically for monomeric initial conditions by means of an explicit Runge-Kutta fourth order method (see Appendix A). Additionally, Figure 4.4 presents the monotonic time evolution of the aggregates mean size, $< S >= \sum_j jX_j / \sum_j X_j$, and its corresponding mean diffusion coefficient, D (inset).

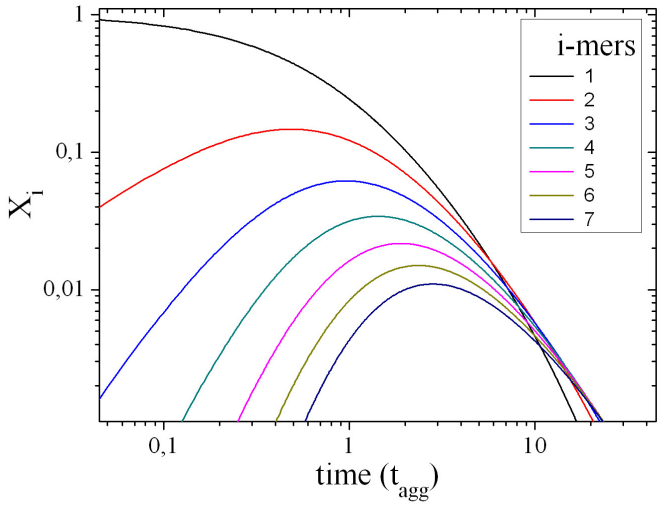

Figure 4.3: Time evolution of those clusters formed by 1 to 7 monomers under DLCA conditions. Time step=0.005 (aggregation time units), where the number of Equations (4.16) is 500.

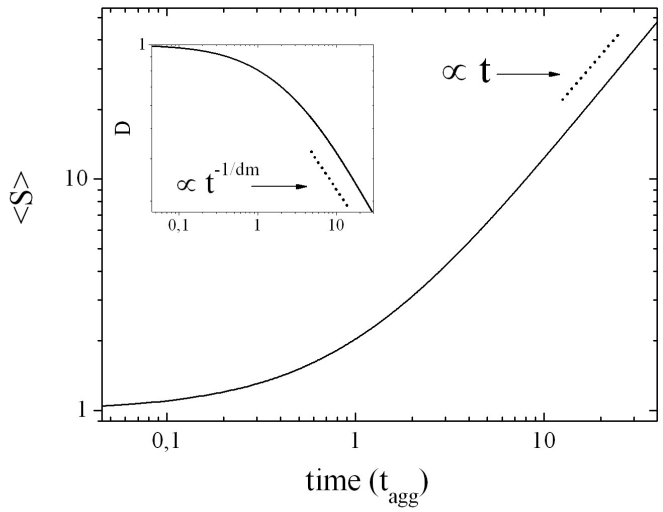

Figure 4.4: Aggregates mean size and mean diffusion coefficient (inset). Computing parameters are as in Fig. 4.3.

Reaction Limited Cluster-Cluster Aggregation (RLCA)

In the previous section we have considered an aggregation process where all the reactions involving two aggregates sufficiently close[30] generate a new aggregate. This situation was plausible since there was not effective repulsive interaction to avoid contact. However, if a remaining repulsive barrier still persists, only those aggregates whose kinetic energy was sufficiently large to overcome the repulsive barrier will become stuck, producing a new aggregate. Although there is a wide literature concerning this *Reaction limited Cluster-Cluster Aggregation* (RLCA) (see for instance the seminal work by Fuchs [78]), here we only consider as RLCA kernel that corresponding to an extension of the Brownian kernel [79]:

$$k_{ij}^{RLCA} = k_{ij}^{Br} P_{ij} \quad ; \quad P_{ij} = p_{11}(ij)^{\beta} \tag{4.25}$$

Where P_{ij} represents the probability of an effective contact, being separated into to contributions: A prefactor p_{11}, representing the effective probability between two monomers, and $(ij)^{\beta}$, which implements the number of combinations between monomers, being controlled by an exponent β. We have two *a priori* limits for β: $\beta = 0$ (associated to $p_{11} = 1$), with which we recover the Brownian kernel, and $\beta = 2$, which gives the maximum number of combinations.

In constract to the DLCA regime, RLCA has not a well defined value for the fractal dimension of the resulting aggregates. This is obviously due to the range associated to the ratio between the repulsive energy barrier and the mean kinetic energy of the aggregates. Nevertheless, a range for the RLCA fractal dimension is assumed, where $1.8 < d_m < 2.1$ [80]. Clusters with fractal dimensions $2.1 < d_m < 3$ cannot usually be explained without appealing to compactification effects (see Paper IV).

[30] See footnote 29.

Excursus

The kernel proposed by Expression (4.25) presents a formal fallacy. At short times, where aggregates are not large, we have $k_{ij}^{RLCA} < k_{ij}^{Br}$, that is, RLCA regime is slower than DLCA regime. However, at long times, when aggregates become sufficiently large, $k_{ij}^{RLCA} > k_{ij}^{Br}$. This last inequality leads to incongruence: RLCA would be faster than DLCA. Therefore, Expression (4.25) fails at the long time limit (i.e. $i, j \to \infty$) and it must be considered only for practical purposes where the aggregation process is not far from the initial monomeric conditions.

Scheme of van Dongen and Ernst

On several real systems, it is difficult to assume a specific model for the reaction kernel. However, it is often possible to extract some general functional behaviors to describe, even quantitatively, those subtle aggregation processes whose kernel cannot be easily presupposed. In this sense, the scheme of van Dongen and Ernst [65, 81] is an attempt to rationalize and classify the kinetics of distinct aggregation processes under a common framework. According to this classification:

$$k_{aiaj} = a^{\lambda} k_{ij} \quad ; \quad \lambda \leq 2 \tag{4.26}$$

$$k_{i<<j} \propto i^{\mu} j^{\nu} \quad ; \quad \lambda = \mu + \nu \quad \text{with } \nu \leq 1$$

Where λ, the so called *homogeneity parameter*, informs on the different reactivity between equally sized clusters. Thus, kernels with $\lambda = 0$ (constant and Brownian kernels) present no different reactivity between small-small and large-large clusters, that is, k_{ij} has a constant diagonal. This is typically the case of those aggregation processes essentially controlled by diffusion, where there is a compensation between the increasing collision cross section and the decreasing diffusivity of the clusters upon increasing j. Restriction $\lambda \leq 2$ is obvious since $k_{jj} = j^{\lambda} k_{11}$ must not increase faster than j^2 (product kernel). Additionally, $\lambda = 1$ (e.g. sum kernel) separates non-gelling

($\lambda \leq 1$) from gelling kernels ($\lambda > 1$). Finally, restriction $\nu \leq 1$ is easily confirmed if we consider the reactivity given by $k_{1j} \propto j^{\nu}$, which cannot be faster than the increment of the cluster volume.

For non-gelling kernels, we have two significant (and connected) results which provide a key point to probe experimental results. On one hand, the time evolution of the mean cluster size is governed by λ as [82]:

$$< S >= \frac{\sum_j jX_j}{\sum_j X_j} \propto t^{(1-\lambda)} \tag{4.27}$$

On the other hand, the mean diffusion coefficient presents an asymptotic behavior ruled by λ and d_m:

$$D \propto t^{-z} \quad ; \quad z = 1/(1-\lambda)d_m \tag{4.28}$$

Where z is usually known as *kinetic exponent*. Figure 4.4 shows both trends for the Brownian kernel with $d_m = 1.75$.

Chapter 5

Glass Transition: Structure and Dynamics

"*La libertad, Sancho, es uno de los más preciosos dones que a los hombres dieron los cielos; con ella no pueden igualarse los tesoros que encierra la tierra ni el mar encubre; por la libertad, así como por la honra, se puede y debe aventurar la vida…*"

Miguel de Cervantes, "Don Quijote de la Mancha",
Capítulo LVIII (Segunda Parte)

If a molecular liquid is cooled below its melting temperature or, in the case of a sufficiently monodisperse colloidal suspension, volume fraction reaches a critical value, both systems crystallize. However, in practice, crystallization can be bypassed when a molecular liquid is supercooled below its melting temperature or a colloidal suspension is led beyond its crystallization volume fraction. Thus, we arrive at a new regime at which both relaxation time and viscosity increase by several orders of magnitude if temperature (or volume fraction) are changed by a small factor. This dramatic evolution would ultimately lead to a divergence of the relaxation time which is associated to the Glass Transition (GT). As a result, it appears a solidlike "state", the glass, whose microscopic structure does not reveal, in principle, any signature to be discriminated from that of a normal liquid. Is the glass a true state? Is the GT a thermodynamic transition or a purely kinetic phenomenon? (Do we need time to define the GT?). Finally, what is a glass? At present, we do not have any conclusive answer to these questions.

5.1. Mode Coupling Theory

A classical observable to describe the dynamics of a liquid and, in particular, of a glass-forming liquid, is the local particle density fluctuation, $\delta\rho(\vec{r},t)$ [43]:

$$\delta\rho(\vec{r},t) = \rho(\vec{r},t) - \langle\rho(\vec{r},t)\rangle \tag{5.1}$$

Where $\rho(\vec{r},t)$ is the local density introduced by Expression (3.4) whereas $\langle...\rangle$ denotes the ensemble average. Similar to the definition obtained for the static structure factor, Expression (3.6), we can define the *Dynamic Structure Factor* of the particle density fluctuations, $S(q,\tau)$, as:

$$S(q,\tau) \equiv \frac{1}{N}\langle\delta\rho(q,t+\tau)\delta\rho(-q,t)\rangle \tag{5.2}$$

From where the static structure factor is easily recovered: $S(q) = S(q,\tau=0)$. As $S(q)$, the dynamic structure factor is again a valuable observable from the experimental point of view since it is essentially what dynamic scattering experiments measure. Nevertheless, any correlation function of a variable only depending on the density fluctuations will present a functional behavior that will remit to that presented by $S(q,\tau)$.

From a pragmatic viewpoint, *Mode Coupling Theory* (MCT) will provide the dynamical information of a glass-forming liquid, e. g. through $S(q,\tau)$, using as input the static information contained in $S(q)$, that is, MCT considers that all the static properties of a glass-forming liquid will be similar to that of a normal liquid. As we will see, MCT offers a picture of the GT in terms of a purely kinetic phenomenon. Since the derivation of the MCT equations is out of the scope of this dissertation, we refer the reader to some excellent reviews [45, 46, 83].

Their expression for a molecular liquid result:

$$\partial_t^2 f(q,t) + \Omega^2(q) f(q,t) + \int_0^t \left(M^{reg}(t-t') + \Omega^2(q) m(t-t')\right) \partial_{t'} f(q,t') dt' = 0 \,; \forall \mathrm{q} \quad (5.3)$$

Where $f(q,t) = S(q,t)/S(q)$ and $\Omega^2(q) = qk_BT/mS(q)$ (k_B being Boltzmann constant, T the absolute temperature and m the mass of any molecule[31]). Equations (5.3) picture the relaxation of our system from the initial condition ($f(q,t=0)=1$) as a formally continuous set of coupled and damped oscillators with memory. Relaxation is governed by the frequencies $\Omega^2(q)$, which depend on the structure of the glass-forming liquid through $S(q)$, whereas the damping is ruled by $M^{reg}(t)$, which controls the regular friction, that is, the friction associated to the modulus of the Fourier component, q, under consideration, while $m(t)$ introduces the coupling between different Fourier components. In principle, both damping terms are integrated in time, that is, they carry the memory of the system.

The set of Equations (5.3) comes from an exact formalism (Zwanzig-Mori operator projection formalism [84, 85]) which can be adapted to colloidal liquids with two convenient assumptions [86]:

- Inertial terms, $\partial_t^2 f(q,t)$, can be neglected assuming that the temporal coarse graining is sufficiently rough and, therefore, $\partial_t^2 f(q,t)$ are small enough due to the large friction coefficients.

- $M^{reg}(t) \propto \delta(t)$, where $\delta(t)$ is again the delta-distribution: Due to the large friction, the regular kernel, $M^{reg}(t)$, is delta correlated since the non-coupled density fluctuations are considered as a Markovian process (see Paper II).

[31] Here we consider MCT for monocomponent systems.

With these approximations, the "colloidal" version of (5.3) results in a set of coupled relaxators:

$$\frac{1}{D_0}\partial_t f(q,t) + \frac{q^2}{S(q)} f(q,t) + \frac{q^2}{S(q)} \int_0^t m(t-t')\partial_{t'} f(q,t')dt' = 0\,;\ (f(q,t=0)=1)\ \forall \mathrm{q} \quad (5.4)$$

Where D_0 is the free diffusion coefficient of the colloidal particles. The final ingredient to close the set (5.4) is the assumption of a functional behaviour for $m(t)$. The standard approximation [86, 87] expands $m(t)$ in terms of a quadratic polynomials combination:

$$m(q,t) = \sum_{\vec{k}+\vec{p}=\vec{q}} V(\vec{q};\vec{k},\vec{p}) f(k,t) f(p,t) \quad (5.5)$$

Where the vertices are static quantities given by:

$$V(\vec{q};\vec{k},\vec{p}) = \frac{n}{q^4} S(q)S(k)S(q)\left(\vec{q}\cdot\left[\vec{k}c(k) + \vec{p}c(p)\right]\right)^2 \quad (5.6)$$

Here n represents the number density of particles and $c(q) = \left(S(q)-1\right)/nS(q)$ (direct Ornstein-Zernike relation). Thus, Expressions (5.4), (5.5) and (5.6) provide a closed set of integro-differential equations to obtain the dynamics of a glass-forming liquid from the static information contained in $S(q)$ [32].

Not surprisingly, in general there is no analytical solution for the MCT equations and they must be solved numerically. In this respect, the reader is referred to Appendix B, where we show a numerical resolution of the theory specialized to a hard-spheres system. There, apart from the q-discretization proposed in reference [86], we offer a simple recipe for the additional time-discretization by an explicit algorithm.

[32] Formally speaking, a more refined model for the vertices would include not only the information contained in $S(q)$ but also multipoint correlations [43].

MCT Predictions

MCT is rich in predictions, many of them being well supported experimentally. Certainly, there are also significant deviations between some of the MCT predictions and data coming from real systems. Here we will remark those successes and failures of the MCT which are significant for our subsequent studies (see Papers V and VI). For a more complete discussion of the MCT predictions, the reader can consult references [44-46].

Let us start with the "high" temperature regime still far from the GT temperature (or the GT volume fraction for colloids). At this regime MCT provides a good quantitative description of the so-called "cage effect", where the particles interaction is solely mediated by a repulsive potential. Under this picture, any particle will be surrounded by their neighbours: The cage. At short times, the intra-cage motion is well described by the first (or early) beta-regime, β_1, where every particle would rattle in its cage. MCT predicts a power law behavior of the form:

$$f(q,t) \approx f(q,\infty) + A(t/t_\sigma)^{-a} \tag{5.7}$$

Where $f(q,\infty)$ is the non-ergodicity parameter, that is, the horizontal asymptotic value that would eventually be reached at the ergodic to non-ergodic transition. A and $a\,(\leq 1/2)$ are real positive parameters, which depend on the system. Here t_σ is an intermediate time which marks the final decay of β_1 (see Paper V). After this first beta-regime, $f(q,t)$ reaches a plateau, reflecting the trapped motion of the particles in their cages even for time decades. This plateau is followed by the escape of the particles and the second (or late) beta regime, β_2, starts. Again, MCT predicts a power law behavior for $f(q,t)$ known as *von Schweidler's law*:

$$f(q,t) \approx f(q,\infty) - B(t/t_\sigma)^{b} \tag{5.8}$$

Where B and $b\,(\leq 1)$ are again positive real numbers. Despite a and b are system dependent, MCT provides a universal, and very useful, constraint (not depending on the system) which links β_1 and β_2:

$$\frac{\Gamma(1-a)^2}{\Gamma(1-2a)} = \frac{\Gamma(1+b)^2}{\Gamma(1+2b)} \equiv \lambda \tag{5.9}$$

Where $\Gamma(x)$ is the Euler-gamma function whereas λ is the so-called exponent parameter [45].

The final decay of $f(q,t)$, known as α-regime, reflects the final escape of the cage. Although not analytically predicted by MCT, the numerical resolution of the MCT equations shows a functional behavior that is satisfactorily approximated by the *Kohlrausch-Williams-Watts* (KWW) stretched exponential function:

$$f(q,t) \propto \exp\left(-(t/t_\alpha)^\beta\right) \tag{5.10}$$

Where t_α is the characteristic time associated to the α-regime whereas the exponent $\beta\,(<1)$ manifests a non-Debye (non pure exponential) decay which is still a matter of debate [45]. As a way of compendium, Figure 5.1 shows $f(q,t)$ obtained from the numerical resolution of a 40-component model, Equations (5.4), at the main peak, q^*, of the static structure factor of a colloidal hard-spheres system. $S(q)$ was taken from a Brownian dynamics simulation [88] for a volume fraction of 0.585 (see details in Appendix B).

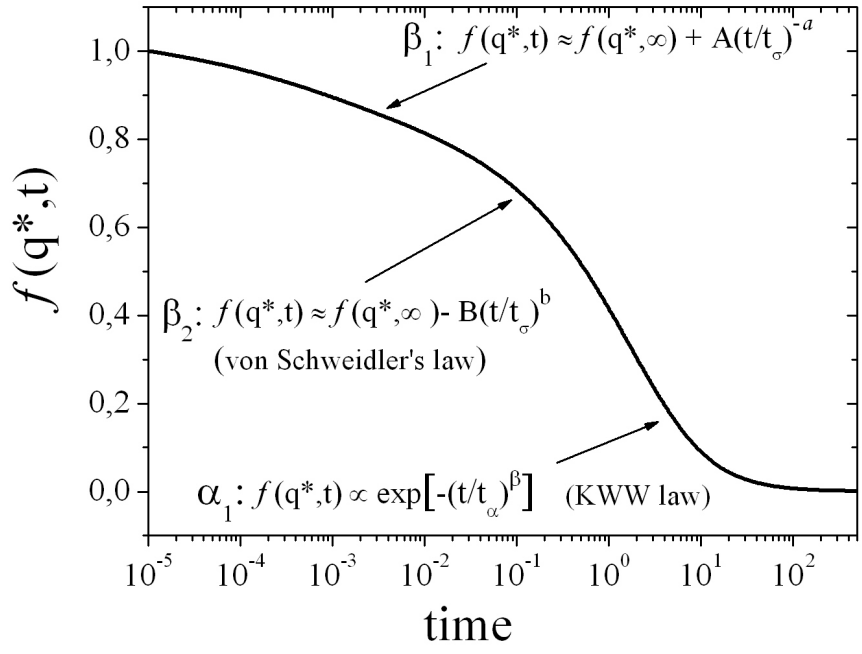

Figure 5.1: Here $\lambda = 0.75$, to be compared with the MCT prediction for hard spheres: $\lambda_{HS} = 0.735$ ($a_{HS} = 0.312$ and $b_{HS} = 0.583$) [86]. For the final α-decay we obtained $\beta = 0.84$. Units of time and length are conveniently normalized fixing the diameter and the free diffusion coefficient in accord with reference [88] (see Appendix B).

We have shown some of the MCT predictions for the high temperature regime (low volume fraction for colloids), still far from the GT, but how is the GT seen by MCT? In the light of MCT, the relaxation time[33] t_α presents a functional behavior which is divergent at a critical temperature[34] T_c [35]:

$$t_\alpha = C(T - T_c)^{-\gamma} \tag{5.11}$$

[33] Here we discuss the MCT divergence in terms of t_α. However, other dynamic observables would hold an equivalent expression to (5.11) (e.g. the relaxation time associated to the self scattering function or the inverse of the effective diffusion coefficient [45]).

[34] An equivalent expression for colloids would consider a critical volume fraction, ϕ_c (see Paper V).

[35] The functional behavior shown by Equation (5.11) is known as the α-scale universality [46].

Where C is a constant which depends on the system as well as on the considered observable whereas γ is a system universal constant[36]. In practice, Expression (5.11) has range of validity when it is contrasted with real systems [45]: The real ergodic to non-ergodic transition temperature, T_g, is found to be around 20% below T_c. Thus, the functional behavior proposed by (5.11) necessarily fails when we approach the real GT. As example of canonical system, it has been shown that for colloidal hard-spheres $\phi_c \approx 0.51$ [86] whereas Brownian dynamics simulations [88] and experiments [89] place the glass transition at $\phi_g \approx 0.59$. As a result, it is frequent to "soften", at least partly, deviations with data coming from experiments or simulations by a convenient temperature or volume fraction rescaling (see Appendix B).

In conclusion, MCT interprets the GT as a kinetic phenomenon where a critical temperature is associated to the divergence of the α-relaxation time, that is, MCT does need time as observable to define "its" own kinetic transition. However, as previously commented MCT fails upon approaching the real ergodic to non-ergodic transition. Therefore, is the GT transition a mere kinetic phenomenon? Has thermodynamics something to say on the GT problem? Next section offers a simplified thermodynamic version of the GT that will be complemented with our results (see Paper VI).

5.2. Random First Order Transition: The mosaic picture

Adam and Gibbs were the first to propose the idea that the relaxation behavior of glass-forming liquids occurs in a cooperative manner [90]. Thus, particles motion would be connected into localized regions whose size would increase upon approaching the GT. In their model, configurational entropy (or complexity) would control the length associated to these domains. This idea started to have support from the 1990's when numerical simulations and experimental phenomenology [91-93] proved the existence of increasingly larger regions that appeared dynamically connected as the glass transition was approached, defining a growing dynamic correlation length. These

[36] MCT establishes an additional constraint between γ, a, and b given by: $\gamma = (1/2a) + (1/2b)$ [46].

regions are now understood as *dynamical heterogeneities* since their relaxation (dynamics) is appreciably different from that of the average. However, the existence of a structural (static) long range order associated to the GT is still hotly debated. On one hand, the static description of a glass-forming liquid given by the classical two-point correlation functions does not show any direct evidence of an increasing length scale (see Chapter 3, section 3.2). On the other hand, inspired by thermodynamic arguments, a static correlation length divergent at the glass transition temperature might be expected. We will briefly discuss one of these arguments in terms of the so-called *Random First Order Transition* (RFOT) theory [94].

In the light of the RFOT theory, the free energy landscape of a glass-forming liquid presents a rough (multivalley) structure. Then, for finite interactions a global state of the system will break into droplets. That is, the system would be composed of amorphous regions each of them associated to a local free energy minimum. Thus, there will be a surface tension between the interfaces of adjacent domains. This surface tension is formally defined as the free energy cost per unit area to create the interface. Then, the free energy cost associated to a region of characteristic length R in a d-dimensional space is:

$$\Delta F_{\cos t} = YR^{\theta} \quad ; \quad \theta \leq d-1 \tag{5.12}$$

In principle, $\theta = d-1$ should be the logical dimensional choice but it has been argued that the very nature of the disordered regions can reduce this exponent [47]. For that reason, the prefactor Y should be understood as a "conveniently" generalized surface tension. Thus, the free energy cost for a region of linear size R to rearrange from one of its available states to another due to thermal fluctuations will be given by Expression (5.12). However, we must pay attention to an additional contribution to the free energy: If our region has many plausible states to be at, there will be an entropic tendency that drives the region to explore its available phase space. This gives us a gain for the free energy:

$$\Delta F_{gain} = -TS_c R^d \tag{5.13}$$

Where S_c is the configurational entropy. We have to note that despite these two opposite contributions given by (5.12) and (5.13), we are dealing with a system (glass forming-liquid) still in equilibrium and, therefore, free energy does not increase nor decrease. Nevertheless, Expressions (5.12) and (5.13) will give us a balance at any given temperature. As a result, we obtain a typical domain size, ξ, by adding both contributions:

$$\xi = \left(\frac{Y(T)}{TS_c(T)} \right)^{\frac{1}{d-\theta}} \tag{5.14}$$

Here we have highlighted all the temperature dependences. Under this picture, our glass-forming liquid would consist in set of regions whose typical size at a given temperature is ξ, or, more intuitively, a mosaic whose tiles have a characteristic linear size given by (5.14). The size of these long-lived metastable regions (the tiles) would increase upon cooling the system reaching an ideal GT that would be associated to a divergence of ξ[37].

To test the mosaic picture, numerical experiments have been suggested to investigate the effect of boundary conditions on the structure of glass-forming liquids which should become long-ranged upon cooling the system [48, 49]. These boundaries would act as pinning fields to retain the hypothetical mosaic tiles. In this respect, the *gedankenexperiment* proposed in Paper VI is an attempt to reconcile the range of validity of the MCT with the emergence of the mosaic picture.

[37] Under this ideal vision of the GT, ξ diverges at the Kauzmann Temperature, that is, at the hypothetical temperature at which the configurational entropy would vanish, see for details [45, 94].

References (Theoretical Background)

[1] G. E. Uhlenbeck and L. S. Ornstein, Phys. Rev. **36**, 823 (1930).

[2] S. Chandrasekhar, Rev. Mod. Phys. **15**, 1 (1943).

[3] M. C. Wang and G. E. Uhlenbeck, Rev. Mod. Phys. **17**, 323 (1945).

[4] R. Brown, Phil. Mag. **4**, 161 (1828).

[5] Einstein, Annalen der Physik **17**, 549 (1905).

[6] M. von Smoluchowski, Annalen der Physik **21**, 756 (1906).

[7] P. Langevin, C.r. hebd. Séanc. Acad. Sci. **146**, 549 (1908).

[8] J. Perrin, *Annales de Chimie et de Physique* **18**, 5 (1909).

[9] R. Kubo, Rep. Prog. Phys. **29**, 255 (1966).

[10] N. G. Van Kampen, *Stochastic Processes in Physics and Chemistry*, Amsterdam: North-Holland (1992).

[11] A. Papoulis, *Probability, Random Variables, and Stochastic Processes, 2nd Ed.* NewYork: McGraw-Hill (1984).

[12] C.W. Gardiner, *Handbook of Stochastic Methods*, Berlin, Springer (2004).

[13] B. J. Alder and T.E. Wainwright, Phys. Rev. Lett. **18**, 988 (1967).

[14] B. J. Alder and T.E. Wainwright, Phys. Rev. A **1**, 18 (1969).

[15] R. Zwanzig and M. Bixon, Phys. Rev. A **2**, 2005 (1970).

[16] A. Widom, Phys. Rev. A **3**, 1394 (1970).

[17] E. J. Hinch, J. Fluid Mech. **72**, 499 (1975).

[18] G.L. Paul and P.N. Pusey, J. Phys. A **14**, 3301 (1981).

[19] C.D. Andriesse, Phys. Lett. **33A**, 419 (1970).

[20] K. Carneiro, Phys. Rev. A **14**, 517 (1976).

[21] A. Boullier, J. P. Boon, and P. Deguent, J. Physique **32**, 159 (1978).

[22] K. Ohbayashi, T. Kohno, and H. Utiyama, Phys. Rev. A **27**, 2632 (1982).

[23] D.A. Weitz, D. J. Pine, P. N. Pusey, and R. J. A. Tough, Phys. Rev. Lett. **63**, 1747 (1989).

[24] J.X. Zhu et al., Phys. Rev. Lett. **68**, 2559 (1992).

[25] B. Lukić et al., Phys. Rev. Lett. **95**, 160601 (2005).

[26] B. V. Derjaguin and L. Landau, Acta Physiochim. USSR, **14**, 633 (1941).

[27] E.J.V. Verwey and J. T. D. Overbeek, *Theory of the stability of Lyophobic Colloids*, Elsevier Publishing Company, Imc., Amsterdam (1948).

[28] R. J. Hunter, *Foundations of Colloid Science*, vol. 1 Oxford University Press, New York (1987).

[29] Lyklema, J. (1995) *Fundamentals of Interface and Colloid Science*, vol. 2. Academic Press, London

[30] P.N. Pusey, *Liquids, Freezing and Glass Transition*, *Lecture Notes for Les Houches, Session LI, Part 2, Course 10: Colloidal Suspensions.* Amsterdam, North-Holland (1989).

[31] G. Nägele, Physics Reports **272**, 215 (1996).

[32] D. Mc Cormack, S. L. Carnie, and D. Y. C. Chan, J. Colloid and Interface Sci. **169**, 177 (1995).

[33] J.N. Israelachvili, *Intermolecular and Surface Forces*, Academic Press, London (1991).

[34] H. C. Hamaker, Physica (Utrecht) **4** (10), 1058 (1937).

[35] S. Marcella, Chem. Phys. Lett. **42**, 129 (1976).

[36] D. N. Petsev and P. G. Velikov, Phys. Rev. Lett. **84**, 1339 (2000).

[37] J. Israelachvili and H. Wennerstrom, Nature **379**, 219 (1996).

[38] D. M. LeNeveu, P. Rand, and V. A. Parsegian, Nature **259**, 601 (1976).

[39] S. Ohki and K. Arnold, Coll. Surf. B **18**, 83 (2000).

[40] J. J. Valle Delgado, *Fuerzas Estructurales en Sistemas Hidrófilos*, Tesis Doctoral, Universidad de Granada (2004).

[41] C.W.J. Beenaker and P. Mazur, Physica A, **120**, 388 (1983).

[42] D. Chandler, *Introduction to modern statistical mechanics*, Oxford University Press (1988).

[43] J. P. Hansen and I. R. Mc Donald, *Theory of Simple Liquids* Academic, London (1986).

[44] F. Sciortino and P. Tartaglia, Advances in Physics **54**, 471 (2005).

[45] W. Kob, Course 5: *Supercooled Liquids, the Glass Transition, and Computer Simulations,* Les Houches, Springer Berlin / Heidelberg (2003).

[46] W. Götze and L. Sjögren, Rep. Prog. Phys. **55**: 241 (1992).

[47] A. Cavagna, arXiv:0903.4264v1 (2009).

[48] A. Cavagna, T. S. Grigera, and P. Verrocchio, Phys. Rev. Lett. 98, 187801 (2007).

[49] G. Biroli, J.-P. Bouchaud, A. Cavagna, T. S. Grigera, and P. Verrocchio, Nature Phys. **4**, 771 (2008).

[50] B. B. Mandelbrot, Science **156**, 636 (1967).

[51] B. B. Mandelbrot, B. B. *The Fractal Geometry of Nature*. W. H. Freeman and Company (1983).

[52] J. Teixeira, J. *Experimental Methods for Studying Fractal Aggregates.* In *On Growth and Form: Fractal and Non-Fractal Patters in Physics.* Proceedings of the Cargèse Summer School 1985. NATO ASI Series E, No. 100. Dordrecht: Martinus Nijhoff Publishers, p.145 (1986).

[53] J. E. Martin and A. J. Hurd, A.J., J. Appl Cryst. **20**, 61 (1987).

[54] C. M. Sorensen, C.M. Aerosol Sci. Technol. **35**, 648 (2001).

[55] E. W. Weisstein http://mathworld.wolfram.com/LebesgueCoveringDimension.html

[56] J. Hawkes, Pro. of the London Mathematical Society (3) **28**, 700 (1974).

[57] P. Pfeifer and J. Avnir, J. Chem Phys. **79**, 3558 (1983).

[58] P. Pfeifer and M. Obert, *The Fractal Approach to Heterogeneous Chemistry,* Chichester, Englad: Wiley (1989).

[59] H. W. Jensen graphics.ucsd.edu/~**henrik**/

[60] D. A. Weitz and J. S. Huang, *Self-similar structures and the kinetics of aggregation of gold colloids Kinetics of Aggregation and Gelation*, ed. F Family and D P Landau (Amsterdam: North-Holland) (1984). Copyright 1984 Elsevier Science Publishers B.V.

[61] T. Vicsek, *Fractal Growth Phenomena*, World Scientific (1988).

[62] H. D. Bale and P. W. Schmidt, Phys. Rev. Lett. **53**, 596 (1984).

[63] D. W. Schaefer et al., Phys. Rev. Lett. **52**, 2371 (1984).

[64] M. L. Broide, Ph.D. Thesis. Massachusetts Institute of Technology (1988).

[65] P. G. J. van Dongen and M. H. Ernst, J.Stat.Phys. **37**, 301 (1984).

[66] F. Family, P. Meakin, and J. M. Deutch, Phys. Rev. Lett. **57**, 727 (1986).

[67] M. von Smoluchowski, Phys.Z. **17**, 557 (1916).

[68] M. von Smoluchowski, Z. Phys.Chem. **92**,129 (1917).

[69] J. M. López, *Electrostatic heteroaggregation processes arising in two-component colloidal dispersions*, Tesis Doctoral, Universidad de Granada (2006).

[70] F. Leyvraz, Physics Reports, **383**, 95 (2003).

[71] Z. A. Melzak, Q. J. Appl. Math **11**, 231 (1953).

[72] R. M. Ziff and G. Stell, J. Chem Phys. **73**, 3492 (1980).

[73] J. B. Mc Leod, Q.J. Math Oxford **13**, 119 (1962).

[74] D. Ramkrishna, *Population Balances: Theory and Applications to Particulate Systems in Engineering*, Academic Press, San Diego, USA (2000).

[75] P. N. Pusey and J. G. Rarity, Mol. Phys. **62**, 411 (1987).

[76] M. Kolb, Phys. Rev. Lett. **17**, 1653 (1984).

[77] M. Y. Lin et al., J. Phys.Condens. Matter **2**, 3093 (1990).

[78] N. Fuchs, Z. Phys. **89**, 736 (1934).

[79] F. Family, P. Meakin, and T. J. Vicsek, Chem. Phys. **83**, 4144 (1985).

[80] M. Y. Lin et al., J. Phys.Condens. Matter **2**, 3093 (1990).

[81] P. G. J. van Dongen and M. H. Ernst, J.Stat.Phys. **50**, 295 (1988).

[82] P. G. J. van Dongen and M. H. Ernst, Phys. Rev. A **32**, 670 (1985).

[83] W. Kob and Kurt Binder, *Glassy Materials and Disordered Solids: An Introduction to their Statistical Mechanics*, World Scientific, Singapore (2005).

[84] H. Mori, Prog. Theor. Phys. **33**, 423 (1965).

[85] R. Zwanzig, *Lectures in Theoretical Physics* Eds. W. E. Britton, B. W. Downs, and J. Downs, Wiley New York (1961).

[86] T. Franosch et al., Phys. Rev. E **55**: 7153 (1996).

[87] L. Sjögren, Phys. Rev. A **22**, 2866 (1980).

[88] Th. Voigtmann, A.M. Puertas, and M. Fuchs, Phys. Rev. E **70**, 061506 (2004).

[89] K. N. Pham, S. U. Egelhaaf, P. N. Pusey, and W. C. K. Poon, Phys. Rev. E **69**, 011503 (2004).

[90] G. Adam and J. H. Gibbs, J. Chem. Phys. **43**, 139 (1965).

[91] M. D. Ediger, Annu. Rev. Phys. Chem. **51**, 99 (2000).

[92] *Dynamical heterogeneities in glasses, colloids, and granular media* Eds.: L. Berthier, G. Biroli, J.-P. Bouchaud, L. Cipelletti, and W. van Saarloos, Oxford University Press, (at press).

[93] L. Berthier et al., Science **310**, 1797 (2005).

[94] T. R. Kirkpatrick, D. Thirumalai, and P. G.Wolynes, Phys. Rev. A **40**, 1045 (1989).

Results

Part 1

Brownian Motion of Rigid and Deformable Particles

Paper I

Nondiffusive Brownian Motion of Deformable Particles: Breakdown of the "Long-Time Tail"

"*While examining the form of these particles immersed in water, I observed many of them very evidently in motion; their motion consisting not only of a change of place in the fluid, manifested by alterations in their relative positions, but also not unfrequently of a change of form in the particle itself; contraction or curvature taking place repeatedly about the middle of one side, accompanied by a corresponding swelling or convexity on the opposite side of the particle.*"

Robert Brown, "*A brief account of microscopical observations made in the months of June, July and August, 1827, on the particles contained in the pollen of plants; and on the general existence of active molecules in organic and inorganic bodies*", Phil. Mag. **4**, 161–173, 1828.

Observation of Nondiffusive Brownian Motion of Deformable Particles: Breakdown of the "Long-Time Tail"

Sándalo Roldán-Vargas[1], Miguel Peláez-Fernández[1], Ramon Barnadas- Rodríguez[2,3], Manuel Quesada-Pérez[4], Joan Estelrich[2] , and José Callejas-Fernández[1]

[1]Grupo de Física de Fluidos y Biocoloides, Departamento de Física Aplicada, Universidad de Granada, E-18071 Granada, Spain.

[2]Departament de Fisicoquímica, Facultat de Farmàcia, Universitat de Barcelona, E-08028 Barcelona, Catalonia, Spain.

[3]Centre d'Estudis en Biofísica, Facultat de Medicina, Universitat Autònoma de Barcelona, E-08193 Cerdanyola del Vallès Bellaterra, Barcelona, Catalonia, Spain.

[4]Departamento de Física, Escuela Politécnica Superior de Linares, Universidad de Jaén, Linares, E-23700 Jaén, Spain.

Abstract

We study the nondiffusive Brownian motion of both rigid and deformable mesoscopic particles by cross-correlated dynamic light scattering with microsecond temporal resolution. Whereas rigid particles show the classical long-time tail prediction, the transition to diffusive motion of deformable particles presents a striking behavior not explained by the existing hydrodynamic treatments. This new observation can be interpreted in terms of a damped oscillatory deformational motion on timescales of the order of the Brownian time. Finally, we show that the nondiffusive Brownian motion depends on the specific flexibility of the particles.

The dynamics of a Brownian particle can be formulated on different levels of description depending on the time scale of interest and the refinement of the hydrodynamic approach [1-3]. Thus, in Einstein's classic investigation [4] no assumptions about the behavior of the particle velocity were made and the motion at long times of a "free" Brownian particle was shown to be diffusive. The initial attempt to incorporate velocity in the description of Brownian motion immediately came with the Langevin equation [5, 6]. Within this approximation, the interaction between the particle and the surrounding fluid was separated into two forces associated with a common origin, a systematic friction and a fluctuating noise, with no considerations of hydrodynamic memory effects. Despite its mathematical significance, this simple model predicts an extremely fast transition from ballistic to diffusive motion which is found to be non-realistic.

The true character of the transition from ballistic to diffusive motion was successfully explored by Alder and Wainwright [7, 8] by means of molecular dynamics simulations assuming a hard-sphere (HS) interaction. They found a "…surprising persistence of the velocities" [8] trough a "long-time tail" ($\propto \tau^{-3/2}$) in the velocity autocorrelation function, with the resultant delay in the emergence of the diffusive motion. In terms of macroscopic fluid dynamics, this observation was explained as a hydrodynamic memory effect due to the circulation of the fluid from the front of the particle, where the fluid is compressed, to the rear, where a rarefaction wave is developed. This vorticity effect pushes the particle resulting in a persistence of its motion. Soon, this finding was mathematically described by detailed hydrodynamics treatments [9-11] and the first real measurements of the long-time tail appeared for simple liquids [12, 13]. For rigid colloidal particles, experiments using dynamic light scattering (DLS) [14-16], diffusing-wave spectroscopy [17, 18], and optical trapping interferometry [19], have consolidated the existence of the long-time tail. Nevertheless, these studies have been based on the assumption of a HS-like interaction (computer simulations) or a fixed, rigid, geometrical shape of the tracer particles (experiments). However, despite their ubiquitous presence, a lack of these investigations devoted to deformable particles still persists.

In this letter, we use cross-correlated DLS to present experimental evidence against the validity of the classic long-time tail prediction in case of mesoscopic deformable particles suspended in a small-molecule solvent. Thus, as opposed to rigid particles, we document an original observation that can be interpreted in terms of the interplay between the translational and the deformational motion of our deformable particles on timescales of the order of the Brownian time. These new data demand a complete theoretical approach to account for the nondiffusive Brownian dynamics of mesoscopic deformable particles. In absence of a theoretical understanding, we show that two deformable particles with similar diffusivity can be distinguished by their specific flexibility through their nondiffusive Brownian motion. As a result, our investigation appears as especially stimulating to be applied to mesoscopic biological objects whose functionality depends on their elastic properties to a great extent [20].

An essential relation holds for the isotropic motion of a Brownian particle between any Cartesian component of its mean-square displacement, $\left\langle \Delta x^2(\tau) \right\rangle$, and its corresponding velocity autocorrelation function, $\left\langle v_x(0) v_x(\tau) \right\rangle$ [6]:

$$\left\langle \Delta x^2(\tau) \right\rangle = 2\int_0^\tau (\tau - t) \left\langle v_x(0) v_x(t) \right\rangle dt \quad , \qquad (1)$$

The brackets denote ensemble averages. Equation (1) applied to the case of a Langevin's particle becomes [6]:

$$\left\langle \Delta x^2(\tau) \right\rangle = 2D_0 \left[\tau - \tau_B + \tau_B \exp\left(-\tau / \tau_B\right) \right] \quad , \qquad (2)$$

where D_0 is the particle's diffusion coefficient and $\tau_B = 2a^2\rho / 9\eta$ the Brownian time. Here a and ρ represent the radius and density of a rigid mesoscopic spherical particle, whereas η is the shear viscosity of the fluid.

In contrast, if we consider a complete hydrodynamic treatment including memory effects, Eq. (1) becomes [11, 15]:

$$\left\langle \Delta x^2(\tau) \right\rangle \cong 2D_0 \left[\tau - 2\left(\frac{\tau_L}{\pi}\right)^{1/2} \tau^{1/2} + \frac{\tau_L}{9}\left(8 - \frac{2\rho}{\rho'}\right) - \frac{\tau_L^{3/2}}{9\sqrt{\pi}}\left(7 - \frac{4\rho}{\rho'}\right)\tau^{-1/2} \right] ; (\tau \geq \tau_L), \quad (3)$$

where $\tau_L = (9/2)(\rho'/\rho)\tau_B$, ρ' being the fluid density. Although both results, Eq. (2) and (3), tend to a common diffusive regime, $\left\langle \Delta x^2(\tau) \right\rangle = 2D_0\tau$ ($\tau >> \tau_B$), the latter presents a slower transition due to its second term ($\propto \tau^{1/2}$), which is associated to the presence of the long-time tail ($\propto \tau^{-3/2}$) in $\left\langle v_x(0)v_x(\tau) \right\rangle$, as can be deduced from Eq. (1). To test these theoretical predictions via DLS, an experimental determination of the normalized autocorrelation function of the scattered field $g_1(q;\tau)$ (q being the magnitude of the scattering vector) can be performed. In case of non-interacting, identical, and rigid spherical particles $g_1(q;\tau) = \left\langle \exp\left(iq\Delta x(\tau)\right) \right\rangle$. If measurements of $g_1(q;\tau)$ are made at short times ($\tau \approx \tau_L$), non-Gaussian effects are hardly appreciable regardless of the statistics of v_x, as can be proved by Taylor's expansion of $g_1(q;\tau)$ [15]. Accordingly [21]:

$$g_1(q;\tau) = \exp\left(-\frac{1}{2} q^2 \left\langle \Delta x^2(\tau) \right\rangle \right) \quad (4)$$

However, instead of using directly $g_1(q;\tau)$ to probe Eq. (2) or (3), an experimental time-dependent "diffusion coefficient" $D_{\exp}(\tau) \equiv \left(-1/q^2\right) d \ln g_1(q;\tau)/d\tau$ is frequently defined [15, 17]. As a result, the slopes of $\left\langle \Delta x^2(\tau) \right\rangle / 2$ obtained from Eq. (2) and (3) are compared with $D_{\exp}(\tau)$, which is determined by numerical differentiation. Nevertheless, we should note that whereas Eq. (2) and Eq. (3) consider uniquely the theoretical translational motion, $D_{\exp}(\tau)$ could also reflect the motion corresponding to non-translational degrees of freedom. This will be a central point in our discussion.

To obtain $D_{\exp}(\tau)$ for the suspensions investigated in this work, we used a three-dimensional DLS spectrometer (LS instruments, Fribourg-Switzerland) with two incident He-Ne laser beams ($\lambda = 632.8$ nm). Suspensions were contained in a cylindrical scattering cell which was immersed in a thermostatized bath. A digital correlator (Flex03lq-OEM) computes the normalized cross-correlation function, $g_C^2(q;\tau)$, of the registered scattered intensities, detected by two avalanche photodiodes (SPCM-AQRH), for which the time-dependent contributions of multiple scattered photons can be neglected. The experimental $g_1(q;\tau)$ were obtained through the relation $g_C^2(q;\tau) = 1 + \beta\left[g_1(q;\tau)\right]^2$ $(0 < \beta < 1)$, with a similar protocol as that described in Ref. [22] for a two-color DLS scheme. The sample time resolved with our correlator is 12.5 ns, with 286 τ-values along the interval $\left[1.25\cdot 10^{-8}, 10^{-4}\right]$ s. For all the experiments, photon counting rates were kept within $\left[10^5, 5\cdot 10^5\right]$ s^{-1} to ensure a maximum dead time of 40 ns, being always under the saturation limit. A reliable statistical estimator of $g_1(q;\tau)$ resulted from the average of 25 independent measurements with 1000 s per measurement. Thus, spurious determinations due to electronic distortions, even at delay times as short as 0.2 μs, are minimized. The magnitude of the scattering vector was fixed at $q_f = 0.026$ nm^{-1}.

For our experimental study, we used three different suspensions which were sufficiently diluted to avoid long-range interactions. First, an aqueous suspension of polystyrene microspheres, denoted as "sample R" (rigid), with mean radius $a_R = 650$ nm, relative standard deviation RSD = 0.04, and particle volume fraction $\phi_R = 0.002\%$. The second sample, "sample D" (deformable), was an aqueous suspension of liposomes made of soybean phosphatidylcholine (SPC) from Lipoid, with mean external radius $a_D = 244$ nm, RSD = 0.15, and $\phi_D = 0.01\%$. The third sample, "sample RD" (rigid-deformable), was an aqueous suspension of liposomes made of dimyristoylphosphatidylcholine (DMPC) from Sigma-Aldrich Inc., with $a_{RD} = 242$ nm, RSD = 0.15, and $\phi_{RD} = 0.01\%$. Due to the extrusion procedure, both SPC and DMPC liposomes show an unilamellar thickness of about 5 nm [23].

The twofold (rigid-deformable) behavior of sample RD comes from the composition of the lipid bilayers, since DMPC membranes exhibit two main phases separated by a threshold temperature (known as main transition temperature): A rigid gel phase and a deformable liquid crystalline phase. Below the main transition temperature, the DMPC membranes retain their rigidity. Above the main transition temperature, that is, in the liquid crystalline phase, it is considered that the majority of the single carbon-carbon bonds of the acyl chains of the lipid bilayers have free rotation [24]. This phenomenon evidences the conversion of the DMPC membrane from the gel to the liquid crystalline phase, where the membrane displays new properties such as an increased permeability and a fluidized state. Thus, we can treat sample RD as rigid or deformable by changing the temperature around its critical value. The main transition temperature of the DMPC bilayers was established at 23.0 ± 0.1 ºC by means of Differential Scanning Calorimetry [24].

Using the described protocol, two examples of the classic long-time tail prediction at 13 ºC and 25 ºC are shown in Fig. 1(a) and 1(b) for sample R. While Langevin's model does not predict the real evolution of $D_{\exp}(\tau)$, the full hydrodynamic model (without fitting parameters) and $D_{\exp}(\tau)$ show a good agreement. Thus, whereas at short times a significant contribution of the long-time tail term ($\propto \tau^{-1/2}$) is apparent, at moderate long times ($\tau \geq 40$ μs) the diffusive regime, $D(\tau)/D_0 \approx 1$, is nearly recovered. In addition, the time evolution of $D_{\exp}(\tau)$ corresponding to sample D at 25 ºC is shown in Fig. 1(c): Neither Langevin's model nor the full hydrodynamic treatment describe satisfactorily these new experimental results. Now $D_{\exp}(\tau)$ shows a clear non-monotonic behavior with at least two marked maxima within our time window over the corresponding Langevin's prediction. After reaching the second maximum ($\tau^* \approx 3.7$ μs), $D_{\exp}(\tau)$ decreases smoothly and tends to its diffusive value, D_0. Since their environments are similar, the distinct trends shown by $D_{\exp}(\tau)$ for the polystyrene spheres and the SPC liposomes should be caused by the different structural properties of these particles.

To support this statement, we present the results obtained for sample RD at different temperatures around the main transition temperature. Thus, the unique significant change in the dynamics of this suspension only involves the elastic properties of the DMPC membranes.

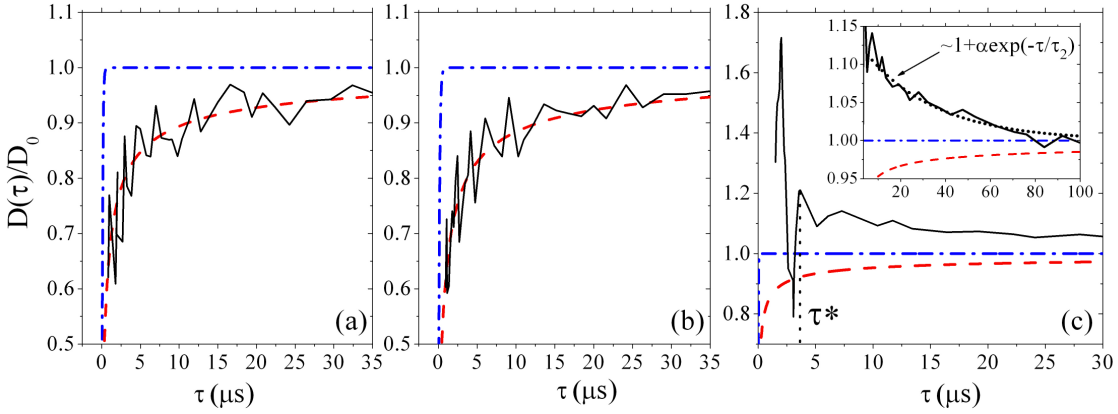

FIG.1 Normalized time-dependent diffusion coefficient $D(\tau)/D_0$ corresponding to sample R at 13 ºC (a) and 25 ºC (b), and sample D at 25 ºC (c). Blue dash-dotted line stands for Langevin's model: $D(\tau)/D_0 = \left(d\left\langle \Delta x^2(\tau)\right\rangle / d\tau\right)/2D_0$, Eq. (2). Red dashed line corresponds to the full hydrodynamic model: $D(\tau)/D_0 = \left(d\left\langle \Delta x^2(\tau)\right\rangle / d\tau\right)/2D_0$, Eq. (3). Black solid line represents the experiment: $D(\tau) = D_{\exp}(\tau)$. D_0 is the experimental free diffusion coefficient corresponding to each temperature. Inset in (c): Dotted line represents the predicted exponential relaxation corresponding to $\tau_2 = 32$ μs and α=0.1.

$D_{\exp}(\tau)$ corresponding to sample RD at 15 ºC, 23 ºC, and 34 ºC are shown in Fig. 2(a), 2(b), and 2(c). In accord with our calorimetric determination, sample RD at 15 ºC is associated to the rigid gel phase of the DMPC membranes. In fact, the full hydrodynamic model and the experimental data show again a common tendency as in the case of sample R (Fig. 2(a)). At 23 ºC, that is, at the main transition temperature, a moderated agreement between theory and experiment still persists although the fluctuations in $D_{\exp}(\tau)$ appear more pronounced (Fig. 2(b)). At 34 ºC the deformable crystalline phase of the lipid membranes is expected, and indeed a noticeable change in the trend shown by $D_{\exp}(\tau)$ occurs (Fig. 2(c)).

As in the case of sample D, we observe a non-monotonic behavior of $D_{\exp}(\tau)$ with a clear maximum at very short times ($\tau^* \approx 0.6$ μs). However, sample RD presents a faster final relaxation than that associated to sample D, almost recovering its diffusive value around $\tau \approx 5$ μs. In our opinion, the complex experimental patterns shown in Fig 1(c) and 2(c) reflect the intricate interplay between the translational and the deformational motion of our flexible particles. At short times, when the translational velocity has not yet been damped, $D_{\exp}(\tau)$ would contain simultaneously the translational and the deformational displacements of the liposomes membrane. Thus, the strong fluid-membrane interaction due to the translational velocity would induce fast changes in the membrane's motion that would be elastically restored, being manifested through the sharp oscillations of $D_{\exp}(\tau)$. In the absence of a dynamic model for $D_{\exp}(\tau)$ in which both translational and deformational motions are considered simultaneously, the latter cannot be easily isolated to be described quantitatively. However, at long times, when the translational velocity is damped, the final relaxation of $D_{\exp}(\tau)$ towards D_0 would reflect essentially the underlying over-damped deformations in the liposome's form.

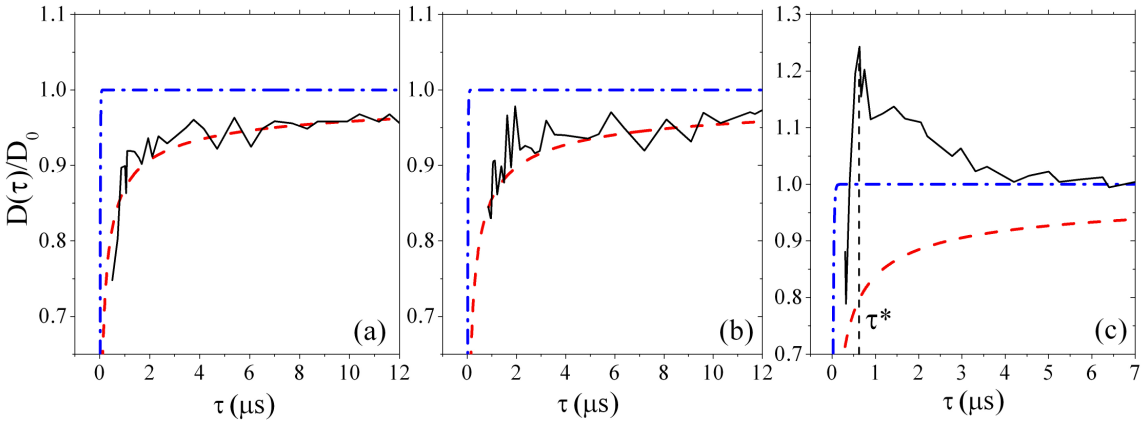

FIG.2 Normalized time-dependent diffusion coefficient $D(\tau)/D_0$ corresponding to sample RD at 15 ºC (a), 23 ºC (b), and 34 ºC (c) with symbols as in Fig.1.

Since we have chosen an adequate q-value for our experiments ($q_f a_{\text{liposome}} \approx 6$), see for details Ref. [25], we are able to explore if this hypothetical deformational motion is present in $D_{\text{exp}}(\tau)$, attempting to reveal the internal modes of deformation of our flexible particles [26, 27]. Hence, we adopt the model proposed by Milner and Safran [26] to describe the small shape fluctuations of a single vesicle in thermal equilibrium, where the translational motion is not considered. Accordingly, the relative displacement of the membrane, $r(\tau,\Omega)$, is expanded into spherical harmonics, $Y_{lm}(\Omega)$, around a fixed radius

a: $r(\tau,\Omega) = a\left(1+\sum_{l>1,m} u_{lm}(\tau)Y_{lm}(\Omega)\right)$, where Ω is the solid angle and $u_{lm}(\tau)$ the amplitude associated to a given mode. By appealing the fluctuation-dissipation theorem, the autocorrelation functions of the amplitudes present an exponential decay $\langle u_{lm}(\tau)u_{lm}(0)\rangle = \left\langle |u_{lm}(\tau)|^2 \right\rangle \exp(-\tau/\tau_l)$, where the relaxation time, τ_l, of a mode driven by bending forces (negligible surface tension [26, 27]) is:

$$\tau_l = \frac{\eta a^3 (2l+1)(2l^2+2l+1)}{k_c l^2 (l+1)^2 (l+2)(l-1)}, \qquad (5)$$

k_c being the bending modulus of the membranes. According to Eq. (5), the slowest relaxation is expected for the second deformational mode. Restricting ourselves to the $l=2$ contribution [25, 27], the final relaxation of $D_{\text{exp}}(\tau)$ would be in first approximation described by an over-damped exponential decay of the form $D(\tau) \approx D_0\left(1+\alpha\exp(-\tau/\tau_2)\right)$, where the damping is mediated by τ_2 as in the case of $\langle u_2(\tau)u_2(0)\rangle$. Here we implicitly assume a small deformations regime, $\left\langle |u|^2 \right\rangle^{1/2} \leq 0.1$, according to the theoretical prediction for standard k_c values of the lipid membranes [26, 28]. In particular, taking the bending modulus of the SPC membranes as $k_c = (1.5 \pm 0.5)\cdot 10^{-19}$ J [28], the relaxation time for a vesicle of $a = 244$ nm suspended in water at 25 ºC is $\tau_2 \approx 32$ μs (Eq. (5)). Using this value, our exponential approximation provides a good description of the final relaxation of $D_{\text{exp}}(\tau)$ even for

amplitudes as big as $\alpha \approx 0.1$ (see inset, Fig. 1(c)). This agreement is certainly encouraging, since it supports quantitatively our interpretation of the relaxation of $D_{\exp}(\tau)$ in terms of an over-damped deformational motion. Regarding sample RD, due to their strong temperature and membrane composition dependence, values for k_c that typically range $\left(2\cdot 10^{-19}, 6\cdot 10^{-19}\right)$J have been documented for the DMPC membranes at the liquid crystalline phase [29]. Accordingly, the corresponding τ_2-range for a vesicle of $a = 240$ nm suspended in water at 34 ºC results $\tau_2 \approx (6,19)\,\mu$s. Although slightly overestimated, this prediction is also in reasonable accord with that observed for the final relaxation time of sample RD, which reaches the diffusive regime around $\tau \approx 5\ \mu$s (see Fig. 2(c)). From the best of our knowledge, these results concerning our flexible particles are the first quantitative observation of the damped deformational motion of a large vesicle under spontaneous nondiffusive Brownian motion. As a result, a powerful practical application emerges: Our methodology is useful to estimate and predict the elastic properties of a great variety of biological deformable particles.

In conclusion, we have revealed the complex scenario present in the nondiffusive motion of a deformable Brownian particle, which is mediated by the coupling between translational and deformational degrees of freedom. As opposed to rigid particles, a complete theoretical understanding of this motion, including its short times description, remains as a challenge.

ACKNOWLEDGEMENTS

The authors are grateful to "MICINN" (Projects No. MAT2006-12918-C05-01 -02, and -05), ERDF Funds, and "Junta de Andalucía" (Project P07-FQM-02496) for financial support. We thank Walter Kob for valuable comments on our manuscript.

Reference List

[1] P.N. Pusey, *Colloidal Suspensions*, Lecture Notes for Les Houches 1989, Session LI (Amsterdam: North-Holland, 1989).

[2] G. Nägele, Physics Reports **272,** 215 (1996).

[3] J. T. Padding and A.A. Louis, Phys. Rev E **74**, 031402 (2006).

[4] A. Einstein, Annalen der Physik **17**, 549 (1905).

[5] P. Langevin, C.r. hebd. Séanc. Acad. Sci. **146**, 549 (1908).

[6] G. E. Uhlenbeck, and L. S. Ornstein, Phys. Rev. **36**, 823 (1930).

[7] B. J. Alder and T.E. Wainwright, Phys. Rev. Lett. **18**, 988 (1967).

[8] B. J. Alder and T.E. Wainwright, Phys. Rev. A **1**, 18 (1969).

[9] R. Zwanzig and M. Bixon, Phys. Rev. A **2**, 2005 (1970).

[10] A. Widom, Phys. Rev. A **3**, 1394 (1970).

[11] E. J. Hinch, J. Fluid Mech. **72**, 499 (1975).

[12] C.D. Andriesse, Phys. Lett. **33A**, 419 (1970).

[13] K. Carneiro, Phys. Rev. A **14**, 517 (1976).

[14] A. Boullier, J. P. Boon, and P. Deguent, J. Physique **32**, 159 (1978).

[15] G.L. Paul and P.N. Pusey, J. Phys. A **14**, 3301 (1981).

[16] K. Ohbayashi, T. Kohno, and H. Utiyama, Phys. Rev. A **27**, 2632 (1982).

[17] D.A. Weitz, D. J. Pine, P. N. Pusey, and R. J. A. Tough, Phys. Rev. Lett. **63**, 1747 (1989).

[18] J.X. Zhu et al., Phys. Rev. Lett. **68**, 2559 (1992).

[19] B. Lukić et al., Phys. Rev. Lett. **95**, 160601 (2005).

[20] R. Lipowsky and E. Sackmann, *Structure and Dynamics of Membranes, Vol. 1* (Elsevier, New York, 1995).

[21] W. D. Davenport and W. L. Root, *Random Signals and Noise* (New York, McGraw-Hill, 1958).

[22] A. Moussaïd and P.N. Pusey, Phys. Rev. E **60**, 5670 (1999).

[23] S. Roldán-Vargas et al., Phys. Rev. E **79**, 011905 (2009).

[24] V.P.Torchillin and V. Weissing, *Liposomes, a practical approach*, (Ed. Oxford University Press. 2003).

[25] J.S. Huang, S.T. Milner, B. Farago, and D. Ritchter, Phys. Rev. Lett. **59**, 2600 (1987).

[26] S.T. Milner and S.A. Safran, Phys. Rev. **A** 36, 4371 (1987)

[27] R. Joannic, L. Auvray, and D.D. Lasic, Phys. Rev. Lett. **78**, 3402 (1996).

[28] M.. B. Schneider, J. T. Jenkins, and W.W. Webb, J. Physique **45**, 1457 (1984).

[29] P. Méléard et al., Biophys. J. **72**, 2616 (1997).

Paper II

Stochastic Description of the Light Scattered by a Polydisperse Colloidal Suspension: Simulation and Experiment

"Have you guessed the riddle yet?" The Hatter said, turning to Alice again. "No, I give it up", Alice replied: "what's the answer?" "I haven't the slightest idea," said the Hatter. "Nor I", said the March Hare. Alice sighed wearily. "I think you might do something better with the time", she said, "than wasting it in asking riddles that have no answers." "If you knew Time as well as I do", said the Hatter, "you wouldn't talk about wasting it. It's him."

Lewis Carroll, "*Alice's Adventures in Wonderland*", Chapter VII (A mad tea-party)

Stochastic Description of the Light Scattered by a Polydisperse Colloidal Suspension: Simulation and Experiment

Sándalo Roldán-Vargas[1], Manuel Quesada-Pérez[2], and José Callejas-Fernández[1]

[1]Grupo de Física de Fluidos y Biocoloides, Departamento de Física Aplicada, Universidad de Granada, E-18071 Granada, Spain.

[2] Departamento de Física, Escuela Politécnica Superior de Linares, Universidad de Jaén, Linares, E-23700 Jaén, Spain.

Abstract

In this work, the stochastic properties of the detected signal in dynamic light scattering experiments are examined in the light of Doob's theorem. For Markovian observations of the Brownian particle position, we prove from this theorem that the electric field scattered by a polydisperse suspension can be accounted for by a linear combination of Ornstein-Uhlenbeck processes. A new algorithm for generating the fluctuating field scattered by a polydisperse system is proposed from this alternative formalism. The statistics of our synthetic data is compared satisfactorily with that resulting from the experimental signal scattered by a binary suspension of polystyrene microspheres.

I. INTRODUCTION

Due to their theoretical and technological significance, Brownian particles systems are still the topic of an impressive number of investigations [1, 2]. From a theoretical viewpoint, different levels of description of the Brownian dynamics are differentiated depending on the time scale of interest [3, 4]. Thus, starting from deterministic Liouville's equation, or its equivalent Newton's second law, the fluid variables can be substituted by an effective noise and the classical Langevin's equation is obtained as an essential theoretical approach. In this context, the description of the dynamics of a "true" Brownian particle becomes stochastic instead of deterministic: The Brownian velocity is given by a well defined Markovian process, the Ornstein-Uhlenbeck process, whereas the particle position is non-Markovian [5, 6]. If the temporal coarse-graining is still increased, and the Brownian velocities are eliminated, we reach the diffusive description. In this theoretical frame, the position of a true Brownian particle is accounted for by the renowned Wiener process [6-8], which is Markovian by definition.

So far, the most widely used experimental technique to probe these dynamic approaches has been Dynamic Light Scattering (DLS) [9]. Knowledge of the autocorrelation function ($g^{(1)}(\tau)$) of the field scattered by a Brownian particles suspension is the cornerstone of this technique. Thus, $g^{(1)}(\tau)$ has been interpreted in terms of the moments of the displacement of the scattering particles, inferring important features such as particle's size and polydispersity [10, 11]. However, the general inversion of such function in terms of dynamic observables still remains as a non resolved problem in which many efforts have been spent [12].

Conversely, the direct generation of $g^{(1)}(\tau)$ based on statistical methods has been investigated as well (although more scarcely). In this respect, examples of Gaussian and non-Gaussian noise models to simulate the statistics of the electric field scattered by monodisperse colloidal suspensions can be found in literature. For instance, Lomakin [13] generated synthetic data normally distributed based on the maximum-likelihood principle for the observed signal. Earlier, Hughes [14] used a Gaussian-Markovian noise

also particularized to monodisperse systems whereas Jakeman and Tough [15] developed a statistical extension to non-Gaussian Markovian processes.

This paper treats the generation of the fluctuating scattered field and its corresponding autocorrelation function from an alternative stochastic formalism. From such formalism, we prove that the fluctuating field scattered by an ideal polydisperse system can be accounted for by a linear combination of Ornstein-Uhlenbeck processes. As a consequence, a new algorithm to simulate the field scattered by these systems is proposed. Some specific and novel aspects of our treatment deserve to be briefly commented in this introduction.

Concerning the underlying physics, we first discuss the properties of the stochastic processes associated to the detected signal in a DLS measurement from Doob's first theorem [16, 17]. The connection between this theorem and DLS has been barely indicated in scattering literature, being almost reduced to the significant work of Phillies [11] which covers the interpretation of $g^{(1)}(\tau)$ under this theoretical frame. However, we show that Doob's treatment can also be used as a tool to propose an algorithm for simulating the fluctuating signal of polydisperse systems separated in different relaxation modes. As far as we know, this constitutes itself a new theoretical insight since such formalism has not been previously applied to generate the synthetic signal associated to DLS measurements. Moreover, as mentioned before, the previous works have been focused on the simulation of the field scattered by monodisperse systems. To the best of our knowledge, however, the formal extension to polydisperse systems has never been investigated.

Concerning practical aspects, our synthetic data can be employed for correlator testing as an alternative to a polydisperse calibration sample. In this way, uncertainties caused by the experimental set up as well as those resulting from the samples preparation [18] can be avoided. Apart from that, statistical errors in experimentally measured correlation functions are also correlated [13]. This additional correlation, which is not desirable in testing procedures, is not present in our simulated correlation functions.

Bearing this application in mind, a comparison with experimental data (which is also innovative) is carried out in the final part of our paper. More specifically, the experimental statistics of the signal scattered by a binary mixture of colloidal particles is compared with that resulting from our simulation. The choice of a binary colloidal suspension to test our stochastic data is due to two main reasons: First, the current technological significance of the binary suspensions in the development of new materials [19, 20]. Second, with the exception of the work of Krause and co-workers in the early nineties [21], this sort of basic DLS studies applied to binary systems are surprisingly scarce in scattering literature.

Accordingly, the paper is organized as follows: In section II our theoretical approach is exposed. Section III presents a description of our simulation method. Section IV introduces the experimental characterization of our binary system. In section V the comparison between experimental and simulated data is presented and discussed. Finally, the conclusions of this research are highlighted.

II. BACKGROUND AND THEORETICAL CONSIDERATIONS

Under quasi elastic light scattering conditions, the instantaneous complex amplitude $E_s(\vec{q};t)$ of the electric field scattered by a N-Brownian particles system at time t for a fixed magnitude of the scattering vector $\vec{q}$ is [9, 22]:

$$E_s(\vec{q};t) = \sum_{i=1}^{N} b_i(q) \exp[i\vec{q} \cdot \vec{r}_i(t)] \ , \qquad (1)$$

where $b_i(q)$ and $\vec{r}_i(t)$ are the scattered field amplitude and the center of mass position associated to particle i, respectively. Since in conventional (homodyne) DLS measurements photo-detectors are sensitive to the flux of energy carried by the scattered wave, the instantaneous intensity of the scattered light $I(t)$ has to be considered [4]:

$$I(t) \equiv \mid E_s(t) E_s^*(t) \mid = \mid E_s(t) \mid^2 , \qquad (2)$$

where $E_s(\vec{q};t)$ is notated as $E_s(t)$, omitting its q-dependence. The information of the temporal fluctuations of $I(t)$ is generally supplied by a digital correlator through the intensity autocorrelation function $g^{(2)}(\tau) =< I(t)I(t+\tau) > / < I(t) >$ within the delay time τ, where $\langle ... \rangle$ represents the time-averaged value.

The stochastic counterparts of the fluctuating observables given by expressions (1) and (2) come from the notion of *stochastic process*, which can be defined as any family of random variables $\{Y(t): t \geq 0\}$, $Y(t)$ being the *observation* at time t [17]. From this definition, the real stochastic process associated to $I(t)$, identified by $\{I(t): t \geq 0\}$, will be conditioned by the stochastic properties of the complex process $\{E_s(t): t \geq 0\}$. Two of these essential properties hold for ideal systems are:

(1) $\{E_s(t): t \geq 0\}$ is a complex *Gaussian* process. Since for non-interacting Brownian particles $E_s(t)$ is given by a sum of a large number of independent random variables identically distributed on time (expression (1)), the c*entral limit theorem* [8, 23] ensures the normal distribution of $E_s(t)$. Thus, its probability density is [22, 24]:

$$P(E_s) = \frac{1}{\pi <| E_s(t) |^2>} \exp\left[-\frac{| E_s(t) |^2}{<| E_s(t) |^2>} \right] \tag{3}$$

By virtue of expression (3), $E_s(t) = \mathrm{Re}\{E_s(t)\} + i\,\mathrm{Im}\{E_s(t)\}$ has two real, uncorrelated, and identically distributed Gaussian components:

$$\begin{aligned} &< \mathrm{Re}\{E_s(t)\} >=< \mathrm{Im}\{E_s(t)\} >= 0 \ ; \\ &< \left(\mathrm{Re}\{E_s(t)\}\right)^2 >=< \left(\mathrm{Im}\{E_s(t)\}\right)^2 >= \frac{1}{2} <| E_s(t) |^2> \ ; \\ &< \mathrm{Re}\{E_s(t)\}\,\mathrm{Im}\{E_s(t+\tau)\} >=< \mathrm{Re}\{E_s(t)\} >< \mathrm{Im}\{E_s(t+\tau)\} >= 0 \end{aligned} \tag{4}$$

Consequently, from expression (4) we have the possibility to model the complex stochastic process $\{E_s(t): t \geq 0\}$ just by attending one of its two real components.

(2) $\{E_s(t):t\geq 0\}$ is a S*tationary* process, that is, $(E_s(t_1),...,E_s(t_n))$ and $(E_s(t_1+h),...,E_s(t_n+h))$ are identically distributed. As long as the observations $E_s(t)$ are determined on an equilibrated system, a DLS measurement larger than the system relaxation time will present a stationary distribution for $\{E_s(t):t\geq 0\}$. As a consequence of expression (2), $\{I(t):t\geq 0\}$ will also hold the stationary property.

II.A) The Markov property and Doob´s Theorem

The applicability of the Gaussian and Stationary properties imposes conditions to our system involving the number of particles, the absence of direct interactions, and the assumption of equilibrium. Apart from these conditions, the temporal coarse-graining of our observation plays an essential role in the stochastic description of the scattering phenomenon. In this respect, we next discuss the validity of our approach, which relies upon the applicability of the Markovian property.

Let us consider a set of ordered times $0<t_1<t_2<...<t_n$, the stochastic process $\{Y(t):t\geq 0\}$ is a *Markov process,* or has the *Markovian property*, if the conditional probability density at time t_n, $P[Y(t_n)\,|\,Y(t_1),...,Y(t_{n-1})]$, is uniquely determined by the value $Y(t_{n-1})$ [6]:

$$P[Y(t_n)\,|\,Y(t_1),...,Y(t_{n-1})]=P_{trans}[Y(t_n)\,|\,Y(t_{n-1})], \qquad (5)$$

where $P_{trans}[Y(t_n)\,|\,Y(t_{n-1})]$ is known as *transition probability*. Therefore, a sequence of Markovian observations (*Markov chain*) can be generated only by two functions: $P[Y(t_1)]$, the initial probability density, and $P_{trans}[Y(t_n)\,|\,Y(t_{n-1})]$. In the context of a DLS measurement, the question is whether a Markovian description of $\{I(t):t\geq 0\}$ and $\{E_s(t):t\geq 0\}$ is appropriate. . Under certain conditions, the answer to this question is provided by Doob's theorem.

The connection between Doob's first theorem [16, 17] and DLS has been indicated very scarcely: As far as we know, Jakeman and Tough [15] were the first to point out this connection whereas, recently, Phillies [11] presented a remarkable discussion on this topic. It is sufficient for our purpose to introduce the restricted real version of this theorem that can be applied separately to $\mathrm{Re}\{E_s(t)\}$ and $\mathrm{Im}\{E_s(t)\}$:

Doob's first theorem [16]: *Let be* $\{Y(t): t \geq 0\}$ *a real, Gaussian and stationary process. If* $Y(t)$ *and* $Y(t')$ *are not independent for all* $t \neq t'$ *then* $\{Y(t): t \geq 0\}$ *is a Markov process (in the sense defined above) if and only if:*

$$< Y(t)Y(t+\tau) >=< Y^2(t) > e^{-\gamma\tau} \; ; \; \gamma > 0 \qquad (6)$$

Therefore, the question considered previously is answered by means of the necessary condition of Doob's theorem: Under the Gaussian and stationary assumptions, an experimental simple exponential decay of $< E_s(t)E_s^*(t+\tau) >$ implies that $\{\mathrm{Re}\{E_s(t)\}: t \geq 0\}$ and $\{\mathrm{Im}\{E_s(t)\}: t \geq 0\}$ have to be treated as Markovian processes. An important consequence is inferred from this statement: Doob's theorem is a test to check whether the observation of the scattered signal during a DLS measurement is Markovian. In addition, from the sufficient condition of Doob's theorem, a Markovian description of $E_s(t)$ for an ideal monodisperse system implies (expressions (1) and (4)):

$$< E_s(t)E_s^*(t+\tau) >=< |E_s(t)|^2 > e^{-\gamma\tau} = N\left(b(q)\right)^2 e^{-\gamma\tau} \; ; \; \gamma > 0 \qquad (7)$$

We should remark that expression (7), which is a familiar result in scattering literature, is here deduced as a consequence of a first-principles description of the stochastic properties of $\{E_s(t): t \geq 0\}$. Thus, the decay rate γ stated in the theorem corresponds to $\gamma = D_0 q^2$, where D_0 is the free diffusion coefficient of the Brownian particles [4, 9].

We can now connect the stochastic description of $\{E_s(t): t \geq 0\}$ to $\{\vec{r}^{\,N}(t): t \geq 0\}$, which is the multivariate stochastic process that represents the system configuration. If the

temporal sensitivity $\tau_{\min}$ of our DLS experiment is much greater than the *Brownian time* τ_B (the characteristic time of the Brownian velocity decay), $\{\vec{r}^{\,N}(t): t \geq 0\}$ will be Markovian: Since many variations of the velocity happen between two successive experimental observations of the position of a particle, the prediction of a future position would be uniquely determined by the last position. As a consequence, $\{E_s(t): t \geq 0\}$ must conserve the Markovian property since the scattered field depends on the system configuration with no explicit dependence on time (expression (1)).

II.B) The Ornstein-Uhlenbeck process

A statement follows readily from Doob's first theorem: The unique real, Gaussian, Stationary, Markovian process that is continuous in probability is the *Ornstein-Uhlenbeck* (OU) process [16, 23].

In fact, OU process is the best known and the most widely applied stationary Markovian process [5, 6, 8, 25-28]. According to definition (5), an OU chain, $Y(t_1),...,Y(t_n)$, can be generated from an initial probability density and a transition probability. Their continuous expressions for a zero-mean and unit variance process are [6]:

$$P(Y_1) = \frac{1}{\sqrt{2\pi}} \exp\left[-\frac{1}{2} Y_1^2\right]$$
$$P_{trans}[Y(t_2) \mid Y(t_1)] = \frac{1}{\sqrt{2\pi(1-e^{-2\gamma\tau})}} \exp\left[-\frac{(Y(t_2) - Y(t_1)e^{-\gamma\tau})^2}{2(1-e^{-2\gamma\tau})}\right] \quad (8)$$

As a result, an OU process is uniquely determined by a ternary set $\{< Y >, < Y^2 >, \gamma\}$. In conclusion, we have reached an alternative calculation of the signal scattered by a suspension of non-interacting particles from Doob's theorem and the formalism of the OU processes: $\{E_s(t): t \geq 0\}$, and then $\{I(t): t \geq 0\}$, can be simulated as discrete OU chains when the Markovian assumption is satisfied.

III. SIMULATION

Generation of discrete OU chains constitutes itself a branch in the field of the numerical resolution of stochastic differential equations. Details about the algorithm used here as well as other algorithms can be consulted in Refs. [27-31]. Our output will be a discrete real OU path within a partitioned time interval $[0,T]$ starting from an input $\{< Y >,< Y^2 >,\gamma\}$:

(1) We divide the interval $[0,T]$ by a large number N, taking as time step $h = T / N$.

(2) According with the Gaussian property, we generate a real set $\{X_0,.....,X_N\}$ normally distributed with zero-mean and $< Y^2 >$ variance.

(3) Starting from $Y_0 = \langle Y \rangle + X_0$, we will construct the real set $\{Y_0, Y_1,..., Y_N\}$ based on the recursive relation:

$$Y_n = \ < Y > \ + \ \kappa\left(Y_{n-1} - < Y >\right) \ + \ \sqrt{(1-\kappa^2)}X_n \ ; \ 1 \le n \le N \ \ (\kappa \equiv e^{-\gamma h}) \qquad (9)$$

Assuming $Y_n = Y(nh) = Y(t_n)$, the generated set $\{Y_0, Y_1,...., Y_N\}$ is a discrete OU chain, consistent with expression (8), satisfying for the continuous limit:

$$\lim_{N\to\infty} < Y_n Y_{n+m} >=< Y^2 > e^{-\gamma m} \qquad (10)$$

Next, this generic recipe will be applied to a monodisperse system. After that, extending the range of applicability of previous works, this recipe will be generalized to polydisperse systems (section III.B).

III.A) Monodisperse System

For a monodisperse system, only one effective decay rate γ has to be considered. So, let $E_s(t_n) = \mathrm{Re}\{E_s(t_n)\} + i\,\mathrm{Im}\{E_s(t_n)\}$ be the simulated instantaneous complex amplitude of the field scattered by a system of identical non-interacting Brownian particles a time t_n. Without loss of generality, we assume the following normalization (see expression (4)):

$$< (\mathrm{Re}\{E_s(t)\})^2 >=< (\mathrm{Im}\{E_s(t)\})^2 >= \frac{1}{2} \quad ; \quad \left(< |E_s(t)|^2 >= N(b(q))^2\right) = 1 \qquad (11)$$

According to expression (9):

$$\begin{aligned} \mathrm{Re}\{E_s(t_n)\} &= \kappa\,\mathrm{Re}\{E_s(t_{n-1})\} + \sqrt{(1-\kappa^2)}\,E_{re,n} \\ \mathrm{Im}\{E_s(t_n)\} &= \kappa\,\mathrm{Im}\{E_s(t_{n-1})\} + \sqrt{(1-\kappa^2)}\,E_{im,n} \\ (1 \le n \le N;\ \kappa &\equiv e^{-\gamma h}) \end{aligned} \quad , \qquad (12)$$

where $E_{re,n}$ and $E_{im,n}$ are the n-components of two uncorrelated Gaussian sets with zero-mean and $1/2$ variance (denoted previously by $\{X_0, ..., X_N\}$). In consequence, the simulated intensity at time t_n is $I(t_n) = \left(\mathrm{Re}\{E_s(t_n)\}\right)^2 + \left(\mathrm{Im}\{E_s(t_n)\}\right)^2$. As example, a simulated chain according to expression (12), and assuming a relaxation time $1/\gamma = 1$ ms, is shown in Fig. 1(a) for a normalized intensity $< I(t) >=< |E_s(t)|^2 >= 1$.

III.B) Polydisperse System

In his work, Phillies [11] discusses the emergence of measurable non-exponential decays of $< E_s(t)E_s^*(t+\tau) >$ for polydisperse systems which are provoked by the different mobilities of the large and small particles present in the scattering volume. Thus, if a slow change in $E_s(t)$ is observed within a short time interval during a DLS measurement, that change will be mainly due to the fluctuations in the scattering volume involving large, and then less mobile, particles. The memory of this fluctuation

will persist to the next short time interval and $E_s(t)$ will not be Markovian. However, this non-Markovian behavior is due to a temporary unbalance between large and small particles in the scattering volume, that is, to a phase fluctuation. Therefore, this effect can be avoided if we consider a large scattering volume with non-significant finite size effects. Under this assumption, to describe the polydispersity of our system we will assume a M-modal particle distribution. Then, $\{E_s(t):t\geq 0\}$ will be separated in M different relaxation modes by generalizing expressions (11) and (12).

Let us consider a polydisperse system described by a M-modal distribution, $(N_1,...,N_M)$, where the number of particles corresponding to the species j, N_j, will be large enough for any $j=1,...,M$. At the same time, the optical and geometrical properties of the particles of species j, contained in $b_j(q)$, are considered as identical. Then, from expression (1):

$$E_s(q;t)=\sum_{i1=1}^{N_1} b_1(q)\exp[i\vec{q}\cdot\vec{r}_{i1}(t)] \ +...+ \ \sum_{iM=1}^{N_M} b_M(q)\exp[i\vec{q}\cdot\vec{r}_{iM}(t)] \qquad (13)$$

Now, the stochastic process associated to $E_s(q;t)$ is a sum of uncorrelated complex processes:

$$\{E_s(q;t):t\geq 0\}=\{E_s^1(q;t):t\geq 0\} \ +...+ \ \{E_s^M(q;t):t\geq 0\} \ , \qquad (14)$$

where each individual process $\{E_s^i(q;t):t\geq 0\}$ ($i=1,...,M$) is determined by its two uncorrelated real components, $\mathrm{Re}\{E_s^i(q;t)\}$ and $\mathrm{Im}\{E_s^i(q;t)\}$. Due to the equivalent stochastic description of both components, we present only the recipe for $\mathrm{Re}\{E_s^i(t)\}$. As OU process, its corresponding ternary set is:

$$\left\{ < \mathrm{Re}\left\{E_s^i(t)\right\} >= 0, < (\mathrm{Re}\left\{E_s^i(t)\right\})^2 >= \frac{N_i\left(b_i(q)\right)^2}{2\sum_{j=1}^{M} N_j\left(b_j(q)\right)^2}, \gamma_i \right\} \quad ; \ \forall i = 1,...,M \ , \qquad (15)$$

where the value of $< (\mathrm{Re}\left\{E_s^i(t)\right\})^2 >$ has been established to fix $< | E_s(t) |^2 >= \sum_{i=1}^{M} \left[< (\mathrm{Re}\left\{E_s^i(t)\right\})^2 > + < (\mathrm{Im}\left\{E_s^i(t)\right\})^2 > \right] = 1$.

Expression (12), applied now to each $\mathrm{Re}\left\{E_s^i(q;t)\right\}$ results:

$$\mathrm{Re}\left\{E_s^i(t_n)\right\} = \kappa_i \, \mathrm{Re}\left\{E_s^i(t_{n-1})\right\} + \sqrt{\left(1-\kappa_i^2\right)} E_{re,n}^i \qquad (16)$$
$$(1 \le n \le N \ ; \ \kappa_i \equiv e^{-\gamma_i h} ; \ i = 1,...,M)$$

Here $E_{re,n}^i$ is the n-component of a Gaussian set with zero-mean and $N_i\left(b_i(q)\right)^2 / 2\sum_{j=1}^{M} N_j\left(b_j(q)\right)^2$ variance. In this situation, the system will present M effective decay rates γ_i, $i = 1,...,M$. As a result, expressions (14) to (16) give again $I(t_n) = \left(\mathrm{Re}\left\{E_s(t_n)\right\}\right)^2 + \left(\mathrm{Im}\left\{E_s(t_n)\right\}\right)^2$. Finally, the non-correlation between different modes can be expressed as:

$$< E_s^i(t) E_s^{j*}(t+\tau) >= \left[N_i N_j\right]^{1/2} b_i(q) b_j(q) \exp\left(-\gamma_i \tau\right) \delta_{ij} \ ; \forall i, j = 1,...,M \ , \qquad (17)$$

where δ_{ij} is the Kronecker symbol. From expressions (14) and (17), the orthodox field autocorrelation function is recovered:

$$< E_s(t) E_s^*(t+\tau) >= \sum_{i=1}^{M} b_i^2(q) N_i \exp\left(-\gamma_i \tau\right) \qquad (18)$$

IV. EXPERIMENTAL SETUP

To test experimentally our simulation algorithm given by expressions (14) to (16), we used two samples of charge-stabilized highly monodisperse polystyrene spheres with identical refractive indexes. Size and polydispersity were estimated separately by means of static light scattering (SLS). In this respect, two aqueous suspensions were prepared, one for each sample at 0.01% volume fraction.

The experimental form factors $P(q)$ were evaluated within the angular range $[10º,150º]$ as the average of three independent measurements from [4]:

$$\frac{P(q)}{P(q_0)} = \frac{\langle I(q)\rangle}{\langle I(q_0)\rangle} \;;\; P(q) \equiv \left(\frac{b(q)}{b(0)}\right)^2, \qquad (19)$$

where $q_0 = (4\pi n/\lambda)\sin(\theta_0/2)$ and $\theta_0 = 10º$, n being the suspension refractive index. The SLS characterizations were performed using a slightly modified Malvern 4700 System (UK) working with a He-Ne laser beam (wavelength *in vacuo* $\lambda = 632.8$ nm). Polydispersity was theoretically accounted for by a trimodal Pseudo-Schulz's distribution as in reference [32]. As a result, a mean radius of $a_A = 40$ nm with a relative standard deviation of 0.07 was obtained for the "small" particle sample (sample A) whereas $a_B = 240$ nm and 0.05 were the optimum radius and polydispersity for the "big" particle sample (sample B).). Henceforth, A and B will be the labels for the corresponding sample.

As in the case of the previous SLS measurements, our DLS essay with a binary suspension was performed with the same scattering device for a fixed scattering angle $\theta_f = 80º$ at 25 ºC. The experimental normalized intensity autocorrelation function $g^{(2)}_{\exp}(\tau) = \langle I(t)I(t+\tau)\rangle / \langle I(t)\rangle^2$ was provided by a digital correlator and analyzed by our own computer software. The corresponding normalized field autocorrelation function

$g^{(1)}_{\exp}(\tau) = \left\langle E_s(q_f;t)E_s^*(q_f;t+\tau)\right\rangle / \left\langle I(q_f;t)\right\rangle$ was then obtained via Siegert relation from $g^{(2)}_{\exp}(\tau)$ [22]:

$$g^{(2)}_{\exp}(\tau) = 1 + c\left(g^{(1)}_{\exp}(\tau)\right)^2 \qquad (20)$$

c being an apparatus constant that in our case is close to 1.

V. RESULTS: SIMULATION AND EXPERIMENT

The aim of this section is to compare the experimental statistics of the field scattered by a bidisperse Brownian particles system obtained from a mixture of samples A and B with that resulting from our simulation method for $M = 2$ (section III.B).

To perform our DLS essay, a bidisperse suspension was prepared by mixing samples A and B resulting in a ratio $N_A / N_B = 90$ for a total volume fraction of 0.01%. The ratio N_A / N_B was adjusted to have $3\left(b_A(q_f)\right)^2 N_A = \left(b_B(q_f)\right)^2 N_B$ within the experimental uncertainty for the fixed scattering angle $\theta_f = 80°$. This ratio was chosen arbitrarily to have different mean intensities coming from the A and B particles ($\left\langle I^B(t)\right\rangle / \left\langle I^A(t)\right\rangle = 3$).

From an experimental viewpoint, the validity of a Markovian description of a physical observable, the scattered intensity $I(t)$ in our experiment, depends entirely on the temporal coarse-graining of our observation. In this respect, a Markovian description is not appropriate if the temporal observation is sensitive enough to estimate the value of the physical observable as well as its "true" temporal variation at a given time. The estimation of a temporal variation implies a memory knowledge of the "immediate" past that will condition the prediction of the "imminent" future, breaking the Markovian

assumption. As mentioned in the last paragraph of section II.A, if $\tau_B << \tau_{\min}$ $\left\{\vec{r}^{\,N}(t) : t \geq 0\right\}$ and $\left\{E_S(t) : t \geq 0\right\}$ (as well as $\left\{I(t) : t \geq 0\right\}$) will be Markovian. In our experiment, the Brownian times associated to each species are $\tau_{\mathrm{B}}\,(\text{sample A}) \approx 5 \cdot 10^{-10}$ s and $\tau_{\mathrm{B}}\,(\text{sample B}) \approx 10^{-8}$ s, obtained from $\tau_B = 2a^2\rho / 9\eta$ [4]. Here $\rho = 1.054\ \mathrm{g/cm^3}$ is the polystyrene density, $\eta = 0.891 \cdot 10^{-3}$ Pa·s the shear viscosity of the aqueous medium at 25 ºC, and a the mean radius of the corresponding sample. Additionally, the experimental delay time τ provided by our correlator run within the range $[10^{-5}, 1]$ s.

Thus, the "true" velocity of the particles of both species is damped many times during our minimum delay time since $\tau_{\min} = 10^{-5}$ s $\approx 10^3 \cdot \tau_B\,(\text{sample B})$. Therefore, a Markovian description for the particle position, and then for the detected signal is a plausible assumption.

To obtain our simulated field we used as input the inverse decay rates $\gamma_{\mathrm{A}}^{-1} = 0.57$ ms and $\gamma_{\mathrm{B}}^{-1} = 3.4$ ms, admitting the free Brownian motion assumption $\gamma = D_0 q_f^2$ [4]. Here $D_0 = k_B T / 6\pi\eta a$ was evaluated via Stokes-Einstein's equation from the particles radii obtained from SLS, T being the absolute temperature and k_B Boltzmann´s constant. The OU processes associated to each real component of the simulated scattered field corresponding to each species were generated considering the experimental ratio $\left(b_B(q)\right)^2 N_B / \left(b_A(q)\right)^2 N_A = 3$. From expression (15), the ternary sets associated to each sample are:

$$\left\{ < \mathrm{Re}\left\{E_s^A(t)\right\} >= 0, < (\mathrm{Re}\left\{E_s^A(t)\right\})^2 >= \frac{N_A\left(b_A(q)\right)^2}{2\sum_{j=1}^{2} N_j\left(b_j(q)\right)^2} = \frac{1}{8}, \gamma_A = \frac{1}{0.57}\ \mathrm{ms^{-1}} \right\}$$
$$\left\{ < \mathrm{Re}\left\{E_s^B(t)\right\} >= 0, < (\mathrm{Re}\left\{E_s^B(t)\right\})^2 >= \frac{N_B\left(b_B(q)\right)^2}{2\sum_{j=1}^{2} N_j\left(b_j(q)\right)^2} = \frac{3}{8}, \gamma_B = \frac{1}{3.4}\ \mathrm{ms^{-1}} \right\} \qquad (21)$$

Once expression (16) is applied for $M = 2$, the simulated intensity at time t_n results (expressions (2) and (14)):

$$I(t_n) = \left(\mathrm{Re}\left\{E_s^A(t_n) + E_s^B(t_n)\right\}\right)^2 + \left(\mathrm{Im}\left\{E_s^A(t_n) + E_s^B(t_n)\right\}\right)^2 \qquad (22)$$

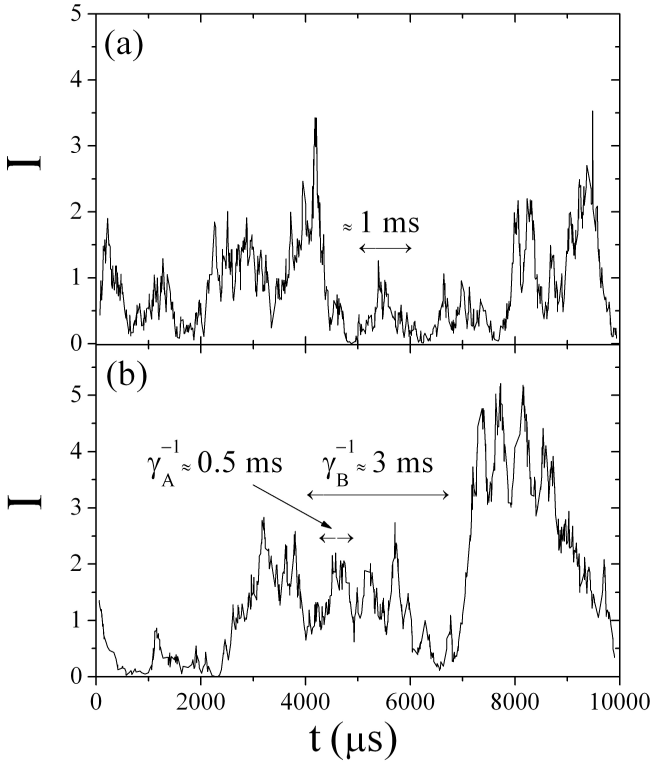

FIG.1 (a) Simulated $I(t)$ for a monodisperse system (section III.A) according to expression (12) with $1/\gamma = 1$ ms. (b) Simulated $I(t)$ for the bidisperse system (section V) according to expressions (16), (21), and (22). In both figures, the time step for the simulation is $h = 1\ \mu$s.

To illustrate the fluctuating behavior of this simulated signal, Fig. 2(b) shows $I(t_n)$ according to expressions (16), (21) and (22) for a time step $h = \gamma^{-1}(\text{sample A})/500 = 1\ \mu$s. Qualitatively, the difference between the generated signals for the monodisperse (Fig. 1(a)) and bidisperse systems (Fig. 1(b)) is apparent. Whereas Fig. 1(a) shows a simple fluctuating pattern typically correlated within times

of the order of 1 ms , a more complex fluctuating behavior is presented in Fig. 1(b). Because of the two separated correlation times, the latter can be seen as a fast fluctuating pattern, typically correlated during a delay time of the order of γ_{A}^{-1}, which is enveloped by a slow one, correlated within delays of the order of γ_{B}^{-1}.

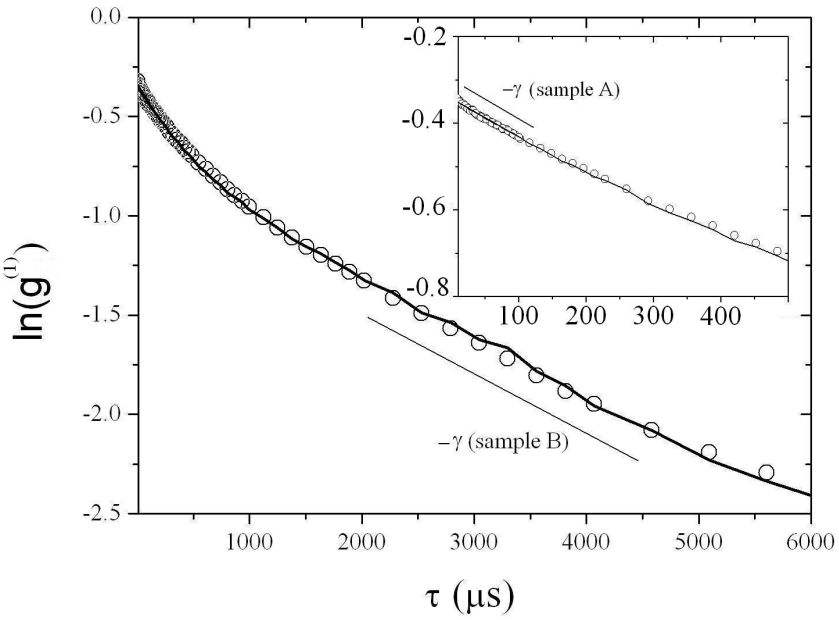

FIG.2 Experimental and simulated field autocorrelation functions for the bidisperse system (section V). Line stands for the simulated field autocorrelation function $g_{sim}^{(1)}(\tau)$ whereas empty dots represent the experimental autocorrelation function $g_{\exp}^{(1)}(\tau)$. The inset shows the decay associated to the small particles. The time step for the simulation was $\mathrm{h} = 1\ \mu\mathrm{s}$ whereas both, experimental and simulated, autocorrelation functions were evaluated during 25 s.

From the simulated bidisperse signal, we obtained the normalized field autocorrelation function $g_{sim}^{(1)}(\tau) = \left\langle E_s(t_n)E_s^*(t_n+\tau)\right\rangle / \left\langle I(t_n)\right\rangle$ which was compared with $g_{\exp}^{(1)}(\tau)$ obtained from expression (20). Figure 2 shows $\ln\left(g^{(1)}(\tau)\right)$ for the simulated and the experimental signals, where both $g_{\exp}^{(1)}(\tau)$ and $g_{sim}^{(1)}(\tau)$ were evaluated for an identical time interval of $T = 25$ s. The inset in Fig. 2 shows a detail of the fast decay corresponding to the motion of the small particles, sample A, whereas the slow decay associated to the big particles has also been remarked through its slope, given by $-\gamma_{\mathrm{B}} \approx -0.29\ \mathrm{ms}^{-1}$. Both

slopes are the obvious manifestation of the correlation times present in Fig. 1(b). From Fig. 2, an excellent accord between experiment and simulation is found: The slopes and the temporal ranges where these slopes are obvious agree completely. Furthermore, an additional remark is pertinent: Formally, the convergence to an analytic model, e.g. a cumulant expansion [33], of an experimental correlation function as $g^{(1)}_{\text{exp}}(\tau)$ is approached after an infinite time of observation. Therefore, from such analytic models it is not possible to estimate *a priori* the duration of finite time experiment in order to obtain a given accuracy. However, a direct stochastic simulation as that presented here confirms and quantifies the accuracy reached from a finite time experiment. In summary, these results are certainly encouraging since they suggest that our synthetic data, particularized in this section for $M = 2$, can be used as a substitute of a polydisperse calibration sample. Moreover, the theoretical frame from which expressions (14) to (16) have been deduced could be considered as a starting point for the simulation of complex systems where non-Gaussian and non-Markovian behaviors are present.

VI. CONCLUSIONS

In this work, the stochastic properties of the signal detected in conventional DLS experiments have been revisited from an alternative stochastic viewpoint. For Markovian observations of the particle position, we have shown that the electric field scattered by a polydisperse Brownian particle system can be generated from a linear combination of Ornstein-Uhlenbeck processes. Doob's theorem plays a key role in this proof connecting the plausibility of a Markovian description with the statistical properties of the detected signal.

From this alternative formalism, a new algorithm for simulating the signal scattered by a polydisperse suspension has been proposed. Its practical realization has been illustrated for a binary mixture of colloidal particles. We have reported excellent agreement between the (synthetic) data generated by this algorithm and those resulting from the real bidisperse sample. Consequently, our simulation method could be a useful tool for analyzing and characterizing polydisperse mixtures of variable composition.

ACKNOWLEDGEMENTS

The authors are grateful to "Ministerio de Educación y Ciencia, Plan Nacional de Investigación, Desarrollo e Innovación Tecnológica (I+D+i)", Projects MAT2006-12918-C05-01and-02, the European Regional Development Fund (ERDF) and "Consejería de Innovación, Ciencia y Tecnología de la Junta de Andalucía" (Project P07-FQM-02496) for financial support. We thank Lorenzo Rovigatti for the critical reading of our manuscript. S.R-V also wants to thank J.M. Angulo Ibáñez for helpful discussions.

Reference List

[1] Y. Han, A. M. Alsayed, M. Nobili, J. Zhang, T. C. Lubensky, and A. G. Yodh, Science, **314**, 626 (2006).

[2] G. D'Anna, P. Mayor, A. Barrat, V. Loreto, and F. Nori, Nature, **424**, 909 (2003).

[3] G. Nägele, Physics Reports **272,** 215 (1996).

[4] P.N. Pusey, *Colloidal Suspensions*, Lecture Notes for Les Houches 1989, Session LI (Amsterdam: North-Holland, 1989).

[5] G. E. Uhlenbeck and L. S. Ornstein, Phys. Rev. **36**, 823 (1930).

[6] N. G. Van Kampen, *Stochastic Processes in Physics and Chemistry* (Amsterdam: North-Holland, 1992).

[7] N. Wiener, J. Math. Phys. **2**, 131 (1923).

[8] C.W. Gardiner, *Handbook of Stochastic Methods* (Berlin: Springer, 2004).

[9] B. J. Berne, and R. Pecora, *Dynamic Light Scattering* (New York: Wiley, 1976).

[10] W. D. Davenport and W. L. Root, *Random Signals and Noise* (New York, McGraw-Hill, 1958).

[11] G. D. J. Phillies, J. Chem. Phys. **122**, 224905 (2005).

[12] H. Schnablegger and O. Glatter, Appl. Opt. **30**, 4889 (1991).

[13] A. Lomakin, Appl. Opt. **40**, 4079 (2001).

[14] A. J. Hughes, E. Jakeman, C. J. Oliver, and E. R. Pike, J. Phys. A, Math and Gen. **6**, 1327 (1973).

[15] E. Jakeman, and R.J.A. Tough, Adv. in Physics **37**, 471 (1988).

[16] J. L. Doob, Annals of Math. **43**, 351 (1942).

[17] J. L. Doob, *Stochastic processes, 2nd ed.* (New York: John Wiley and Sons Ltd., 1990).

[18] F. Ferri and D. Magatti, Rev. Sci. Instr. **74**, 4273 (2003).

[19] S. K. Rhodes and J.A. Lewis, J.Am.Ceram.Soc. **89** (6), 1840 (2006).

[20] K. P. Velikov, C.G. Christova, R.P.A. Dullens, and A. van Blaaderen, Science, **296**, 106 (2002).

[21] R. Krause, G.Nägele, J.L. Arauz-Lara, and R. Weber, J. Colloid. Interface. Sci. **148**(1), 231 (1992).

[22] P. N. Pusey, in *Photon Correlation Spectroscopy and Velocimetry-Chapter: Statistical properties of scattered radiation* (eds. Cummins, H. Z. & Pike, E. R.) (New York: Plenum, 1977).

[23] J. W. Strutt (Lord Rayleigh), Philos. Mag., 5th series, **10,** 73 (1880).

[24] A. Papoulis, *Probability, Random Variables, and Stochastic Processes, 2nd ed.* (NewYork: McGraw-Hill, 1984).

[25] M. Lax, Rev. Mod. Phys. **32**, 25 (1960).

[26] M. C. Wang and G. E. Uhlenbeck, Rev. Mod. Phys. **17**, 323 (1945).

[27] S. Finch, *Ornstein-Uhlenbeck Process*, `http://algo.inria.fr/csolve/ou.pdf` (2004).

[28] W. Feller, *An introduction to Probability and its Applications, 2nd ed.* (New York Wiley, 1971).

[29] L. Bartosch, Int. J. Mod. Phys. C **12**, 851 (2001).

[30] R. L. Honeycutt, Phys.Rev. A **45**, 604 (1992).

[31] D. J. Higham, SIAM Rev. **43**, 525 (2001).

[32] S. Roldan-Vargas, A. Martín-Molina, M. Quesada-Pérez, R. Barnadas-Rodríguez, J. Estelrich, and J. Callejas-Fernández, Phys. Rev. E **75**, 021912 (2007).

[33] D. E. Koppel, J. Chem. Phys. **57**, 4814 (1972).

Part 2

Aggregation in Suspensions of Charged Liposomes

Paper III

Aggregation of Liposomes Induced by Calcium: A Structural and Kinetic Study

Aggregation of Liposomes Induced by Calcium: A Structural and Kinetic Study

Sándalo Roldán-Vargas[1], Alberto Martín-Molina[1], Manuel Quesada-Pérez[2], Ramon Barnadas-Rodríguez[3], Joan Esterlrich[3], José Callejas-Fernández[1]

[1]Grupo de Física de Fluidos y Biocoloides, Departamento de Física Aplicada, Universidad de Granada, E-18071 Granada, Spain.

[2]Departamento de Física, Escuela Politécnica Superior de Linares, Universidad de Jaén, Linares, E-23700 Jaén, Spain.

[3]Unitat de Fisicoquímica, Facultat de Farmàcia, Universitat de Barcelona, E-08028 Barcelona, Catalonia, Spain.

Abstract

In this work, the calcium-induced aggregation of phosphatidylserine liposomes is probed by means of the analysis of the kinetics of such process as well as the aggregate morphology. This novel characterization of liposome aggregation involves the use of static and dynamic light scattering techniques to obtain kinetic exponents and fractal dimensions. For salt concentrations larger than 5mM, a diffusion limited aggregation regime is observed and the Brownian kernel properly describes the time evolution of the diffusion coefficient. For slow kinetics, a slightly modified multiple contact kernel is required. In any case, a time evolution model based on the numerical resolution of Smoluchowski´s equation is proposed in order to establish a theoretical description for the aggregating system. Such model provides an alternative procedure to determine the dimerization constant, which might supply valuable information about interaction mechanisms between phospholipid vesicles.

I. INTRODUCTION

Phospholipid vesicles (liposomes) are colloidal systems that present a major interest in the pharmaceutical, cosmetic and food industry since they are biocompatible structures to encapsulate proteins, nucleic acids, drugs, etc. Moreover, liposomes are considered as model systems of the cellular membrane. In particular, they have been widely applied to the study of biological transport through membranes, induced aggregation phenomena, etc...[1-3]. Therefore, liposomes play an important role in many research areas since the early 60s. Besides their numerous medical applications, liposomes could be considered as model colloidal systems since magnitudes such as size, charge and rigidity can be easily controlled during their synthesis. In this sense, vesicular suspensions present the typical properties of colloidal dispersions from a physicochemical point of view. This twofold role of liposomes is precisely the main advantage of this system. Namely, a colloidal formalism of aggregation applied to phospholipid vesicles appears as a crucial step for a better understanding of complex phenomena in cell biology such as the membrane fusion. In this sense, knowledge about the temporal evolution of an aggregating colloidal system, as well as the study of the geometrical properties of the resulting aggregates, have demonstrated to be a key to understand and control the interaction mechanism between individual particles.

Due to the importance of the aggregation-fusion between vesicles, in the last decades a considerable progress has been made towards the comprehension of the underlying mechanisms and factors involved in these processes [1, 4-6]. In most of these works, it is well established that the ion-induced vesicular aggregation and fusion depend essentially on the composition, charge, size and concentrations of the liposomes as well as on characteristics of the dispersion media such as pH, ionic strength, temperature and type of ions presented therein. In particular, the well known fact that Ca^{+2} is involved in many biological membrane fusion phenomena results in a numerous research works devoted to the study of aggregation and fusion of pure bovine brain phosphatidylserine (PS) liposomes by effect of the divalent cations [4,5,7,8]. Accordingly, the main goal of this research work is dedicated to deepen into the study of the Ca^{+2}-induced aggregation

between PS liposomes by means of a novel *modus operandi* based on the analysis of the aggregation kinetics as well as the morphology of the resulting aggregates.

From the point of view of colloidal science, an enormous effort has been done in the past in order to reach a whole knowledge of the particle aggregation phenomena from theoretical, simulation and experimental approaches. However, in reviewing the literature, the aggregation of "biological particles" such proteins or vesicles have been scarcely studied using the well developed techniques from colloidal aggregation. This is the main interest of this work, to describe the aggregation of vesicles using some methods from colloidal science. This is the primal reason why in this work the aggregation kinetics and cluster structure of the liposomes are analyzed. On one hand, the term *cluster structure* refers to the spatial distribution of the monomers into the aggregate. When a scale-invariant growth appears the geometrical description can be expressed in terms of a cluster fractal dimension, d_f. In colloidal science, this magnitude can be straightforwardly determined by means of scattering techniques hence it is surprising that this magnitude has been rarely employed in the studies of aggregation of liposomes as Lasic claims [7]. Certainly, there are previous works in which liposomes and their aggregation processes are studied by light scattering. However, the number of them that apply the notion of fractal dimension is considerably scarce. For instance, Bordi *et al*. [9] offers an advisable work in which light scattering becomes a powerful tool to investigate polyion-induced aggregation but fractal dimensions are not considered by them. Stauch *et al*. [10] do apply this concept to the study of the inner structure of chemically modified liposomes (but as individual entities). As far as we know, only Linch *et al.* looked into the kinetics of liposome aggregation (induced by proteins in this case) by means of turbidity measurements with the help of this concept [11].

On the other hand, *aggregation kinetics* addresses to the possibility to do a whole description of the aggregating dispersion, *i.e*, to know at a fixed time the number of clusters $N_n(t)$ having n particles each one. A feasible approach to solving this nontrivial problem is the resolution of the Smoluchowski equation at which the key parameters are

the "aggregation kernels", *i.e.* a set of kinetic rate constants for all possible cluster-cluster reactions. Additionally, the van Dongen-Ernst homogeneity parameter, λ , can be useful to complete the description of an aggregating system [12,13].

Historically, two limiting regimes have been identified in colloidal aggregation: a rapid diffusion limited cluster aggregation (DLCA) and a slow reaction limited cluster aggregation (RLCA). Salt-induced aggregation of electrically stabilized bare particles aggregating at low and high electrolyte concentration is an example where these limiting regimes have been successfully obtained. To date, both the resolution of Smoluchowski´s equation (via the selection of an adequate kernel) and the kinetics description in the van Dongen-Ernst scheme have not been applied to liposomes aggregation.

Bearing all this in mind, the paper is organized as follows: Firstly, an overview of the colloidal aggregation theory is presented. Next, a section in which the experimental procedures are described. Finally, experimental and numerical results are shown. Namely, the spatial distribution of liposomes into the clusters is estimated via measurements of the aggregates fractal dimension obtained by means of Static light scattering (SLS). On the other hand, Dynamic light scattering (DLS) technique is used to describe the kinetics of the liposomes aggregation induced by calcium. In addition, an evolution kinetic model based in the numerical resolution of Smoluchowski´s equation is proposed in order to establish a theoretical description for the aggregating system.

II. THEORETICAL BACKGROUND

A. Fractal Geometry and Static Light Scattering (SLS)

The spatial correlations between particles of a structure are usually accounted for the *pair correlation function* $c(\vec{r})$:

$$c(\vec{r}) = \frac{1}{V}\sum_{r'} \rho(\vec{r}+\vec{r}')\rho(\vec{r}'), \qquad (1)$$

where V is the volume of the structure and $\rho(\vec{r})$ the local density ($\rho(\vec{r})= 1$ if $\vec{r}$ belongs to the structure, otherwise it is equal to zero). The functional behaviour of $c(\vec{r})$ can be used as a criterion to determine the fractal growth of an object (aggregate). An isotropic finite object presents a non-trivial scale-invariant growth if [14]:

$$c(r) \propto r^{df-d} f(r / R_{obj}), \tag{2}$$

where d is the topological spatial dimension, d_f is the fractal dimension, R_{obj} the average radius of the object and $f(x)$ is a cutoff function in which the finite size of the object is considered, satisfying $f(x) \approx 1$ for $x << 1$ and $f(x) \approx 0$ for $x >> 1$.

According to its definition in scattering theory, the *structure factor* $S(q)$ is related with the pair correlation function through a Fourier transform [14]. This relationship gives an equivalent condition for (2) expressed via $S(q)$:

$$S(q) \propto q^{-df} \quad 1/R_{obj} << q << 1/a, \tag{3}$$

where the finite size of the constituent particles of the object has been considered through the domain given by the inequality, $\vec{q} = \vec{k}_i - \vec{k}_s$ is the scattering vector, defined as the difference between the incident and the scattered wave vectors, and a is the average radius of the particles.

Thanks to this equivalent description in the q-space given by the structure factor, the fractal geometry of a distribution of aggregates in a 3D-suspension can be determined by means of a SLS experiment, where experimental values for $S(q)$ and, in the case that fractal nature appears, d_f, are obtained. This experimental access is given by:

$$S(q) = \frac{\rho_0 \langle I(q) \rangle}{\rho \langle I_0(q) \rangle}, \tag{4}$$

where we assume $q = \frac{4\pi}{\lambda_m}\sin(\theta/2)$ (elastic light scattering), being λ_m the wavelength of the incident light beam in the medium, θ is the scattering angle, ρ is the particle concentration and $\langle I(q)\rangle$ is the time-averaged light intensity scattered by the particle dispersion. The lower index $_0$ indicates the corresponding values to the diluted and disordered suspension.

B. Diffusion and Dynamic Light Scattering (DLS)

The temporal fluctuations in the instantaneous electric field, $E(q,t)$, scattered by a particle suspension and detected in a far-field position are the measurable effect of the diffusive motion of the particles. The time correlations of these fluctuations are studied in terms of the *normalised field autocorrelation function* $g(\tau)$, its expression for a polydisperse cluster system adopts the form [15]:

$$g(\tau) = \frac{\langle E(q,0)E^*(q,\tau)\rangle}{\langle I(q)\rangle} = \frac{1}{\langle I(q)\rangle}\sum_n b_n(q)\exp(-\Gamma_n\tau), \qquad (5)$$

where $b_n(q)$ contains the relative frequency and the structure of a n-particle cluster and Γ_n is its associated decay rate, in which rotational and translational diffusions are included,

$$\Gamma_n = D_n q^2 + 6D_n^{rot}, \qquad (6)$$

where D_n and D_n^{rot} are the translational and rotational diffusion coefficients of a *n*-particle cluster, assuming that D_n and D_n^{rot} are uncoupled. Taking into account the typical values for q and the average cluster size, through its hydrodynamic radius, we can assume that rotational and translational diffusions happen in two separated time scales and

$$D_n\, q^2 >> D_n^{rot}, \qquad (7)$$

can be considered as a plausible assumption [13].

In order to obtain the average value for the translational diffusion coefficient $\overline{D}(q)$ over the system at any time, the experimental autocorrelation function is treated as an expansion in powers of τ, this treatment is known as cumulant method [16]. The expression for its logarithm results:

$$\ln\left(g_{\exp}(\tau)\right) = -\kappa_1\tau + \frac{1}{2}\kappa_2\tau^2 + \ldots, \tag{8}$$

where κ_i is the i-order cumulant. Relating (5) with (8) and assuming (7) we find that κ_1 represents the average decay rate, κ_2 contains the standard deviation while $\overline{D}(q)$ is given by:

$$\overline{D}(q) = \frac{\sum_n b_n(q) D_n}{\sum_n b_n(q)} = \frac{\kappa_1}{q^2}, \tag{9}$$

which is the basis for the access, through a DLS experiment, to the aggregation kinetics of a particle suspension.

C. Aggregation kinetics and Smoluchowski´s equation

A time evolution model for the cluster size distribution arising in an aggregating system may be obtained by solving Smoluchowski's rate equation [17, 18]:

$$\frac{dN_n}{dt} = \frac{1}{2}\sum_{i+j=n} k_{ij} N_i N_j - N_n \sum_{i=1}^{\infty} k_{in} N_i, \tag{10}$$

where $N_n(t)$ can be used as a frequency distribution in order to obtain the mean value of any function of n. k_{ij} is a set of constants called kernel, hypothetically infinite, inwhich the whole kinetic information is contained. The aggregation kernel, k_{ij}, quantifies the

average rate (for all orientational and structural configurations) at which two *i*- and *j*-particle clusters react and form an (*i*+*j*)-particle cluster. The above equation, in which fragmentation does not occur, is applied to diluted systems where only binary reactions are contemplated.

A general scheme to classify the aggregation kernels attending their homogeneity was proposed by van Dongen and Ernst [19]. This classification can be expressed as follows:

$$k_{aiaj} \propto a^{\lambda} k_{ij} \quad ; \quad (\lambda \leq 2)$$
$$k_{i<<j} \propto i^{\mu} j^{\lambda-\mu} \quad ; \quad (\lambda - \mu \leq 1) \qquad (11)$$

The homogeneity parameter, λ, correlates the aggregation rates involving two different reactions between similar sized clusters, while μ controls the rates for the reactions involving different sized clusters. Restrictions over λ and μ come from the non-physical possibility for which cluster reactivity cannot rise faster than its mass. Restricting ourselves to nongelling-kernels ($\lambda \leq 1$), the scaling theory [20] gives us the asymptotic behaviour in time for the number-average cluster-size, $\overline{n}_n(t)$, as a function of λ:

$$\overline{n}_n(t) = \frac{\sum_j jN_j}{\sum_j N_j} \sim t^{1/(1-\lambda)}, \qquad (12)$$

On the other hand, the *n*-dependence for the *n*-particle cluster translational diffusion coefficient, D_n, was estimated assuming the aggregates to be fractal objects [19],

$$\frac{D_n}{D_0} = (n)^{-1/df}, \qquad (13)$$

where D_0 is the diffusion coefficient of the free individual particles. Considering (12) and (13), the following asymptotic behaviour for $\overline{D}(t;q)$ can be predicted:

$$\overline{D}(t;q) \sim t^{-\alpha}, \tag{14}$$

where $\alpha = 1/(1-\lambda)d_f$. This behaviour is the key to associate a type of kernel to the results obtained for an experimental aggregation kinetics. In order to describe DLCA regime, mentioned in the introduction, the Brownian kernel is commonly accepted [17, 18]:

$$k_{ij}{}^{Brown} = \frac{1}{4} k_{11}{}^{Brown} (i^{1/df} + j^{1/df})(i^{-dh} + j^{-1/dh}), \tag{15}$$

where $k_{11}{}^{Brown}$ is the dimer aggregation rate, d_f is the previously defined cluster geometric fractal dimension and d_h is the cluster hydrodynamic fractal dimension. In this work, we assume for liposomes $d_h = d_f$ as others authors do for rigid particles [21, 22]. In any case, the plausibility for this assumption will be argued later.

A common kind of kernels for describing slow-type regime evolution usually consider the Brownian kernel as a limit, introducing function P_{ij} (depending on a sticking probability, p_{11}) in order to impose a rate of effective contacts[23],

$$k_{ij} = k_{ij}{}^{Brown} P_{ij}, \quad (P_{ij} = p_{11}(ij)^{\beta}), \tag{16}$$

where the probability for an effective monomer-monomer contact, p_{11}, has been separated from the total effective combinations of contacts between two i and j-clusters, through the β parameter, where $\lambda = 2\beta$. β lies in general between the limiting values 0 and 0.5, but an expected value comes from the hypothesis that only particles at the surface of the cluster contribute in the collision [12].

For this multiple contact (MC) diffusionlike case, β becomes:

$$\beta = 3(d_f - d_{fD}) / d_f d_{fD}, \qquad (17)$$

here d_f is the fractal dimension for the slow aggregates while d_{fD} is the diffusive fractal dimension. As expected, this non-diffusive kernel reduces to the Brownian case when $d_f = d_{fD}$.

III. MATERIALS AND METHODS

PS from bovine spinal cord was obtained from Lipid Products (Nutfield, UK). Phospholipid at the proportions indicated below were dissolved in a mixture (2:1, volume ratio) of chloroform and methanol in a round-bottom flask and dried in a rotary evaporator under reduced pressure at 40 ^{0}C to form a thin film on the flask. The film was hydrated with desionized water (MilliQ, Millipore, USA) to give a lipid concentration of 30mM. Multilamellar liposomes (MLV) were formed by constant vortexing for 4 min on a vortex mixer and sonication in a Transonic Digitals bath sonifier (Elma, Germany) for 10 min. MLV were downsized in an Extruder device (Lipex Biomembranes, Canada) through polycarbonate membrane filters of variable pore size under nitrogen pressures of up to 55x10^5 N.m^{-2} [24]. Liposomes were extruded in three steps: first, three consecutive extrusions through a 0.8 μm pore diameter filter and three other consecutive extrusions through two stacked 0.4 μm membranes. The resulting lipid suspension was then extruded fifteen consecutive times through two stacked 0.2 μm filter. After preparation, a nitrogen stream was passed to displace the air, and, finally, liposomes were stored at 4-7 ^{0}C in a refrigerator in quiescent conditions until their use.

A. Characterization of the liposomes

To characterize a liposome suspension two different requirements are necessary. The first involves their characterization in size and shape while the second concerns the

determination of the initial liposomes concentration, which is a troublesome problem when vesicles are used as colloidal particles.

In order to determine liposome size, several DLS experiments were performed for different diluted liposomes volume fractions and angles verifying a constant value (in time and experiment) for the mean particle diffusion coefficient, $\overline{D}_{\exp}(t;q)$, obtained using the cumulant analysis given by (8). The experimental field autocorrelation function results from the scattered intensity autocorrelation function, $g_I(\tau)$, through the Siegert relation, being $\gamma < 1$ a constant,

$$g_I(\tau) = 1 + \gamma^2 \left(g_{field}(\tau)\right)^2 \qquad (18)$$

An approximated value for the mean liposome external radius comes from the hydrodynamic radius R_h associated to $\overline{D}(t;q)$ via Stokes-Einstein relation. Combining these previous DLS experiments with a SLS experiment, an alternative size determination can be done by fitting the *form factor, P*(*q*), realising $\langle I_0(q) \rangle \propto P(q)$. Theoretically, a hollow sphere is usually accepted as simple geometrical model to describe the form of a liposome. Form factor for a hollow sphere in the context of the Rayleigh-Gans-Debye theory is given by the expression:

$$P(q) = \left[3 \frac{\sin(qR) - qR\cos(qR) - \sin(tqR) + tqR\cos(qR)}{(1-t^3)(qR)^3} \right]^2, \qquad (19)$$

where *R* is the inner radius of the sphere and *R(t-1)* the thickness of the shell, which value applied to unilamellar liposomes is closed to 4.5 nm. [25]. Since a direct estimation for the size distribution in a polydisperse suspension is an ill conditioned problem, a probability distribution has to be assumed. In order to consider the intrinsic size polydispersity, Schulz's distribution is commonly used as a semiempirical model, where thickness remains constant. This continuous distribution is defined by two parameters, the mean inner diameter, $\overline{\sigma}$, and the relative standard deviation *s* [26,27] .

In this work, however, the polydispersity description has been done by using an alternative discrete trimodal distribution, characterized by three modal values and their weights, and related with a Schulz distribution asking for equal values for the five first moments for both distributions (the sixth condition is the normalization condition for the weights). The best estimation comes from the optimum values for $\overline{\sigma}$ and s that minimize mean quadratic error between the linear combination given by the trimodal distribution

$$P_{tri}(q) = \sum_{i=1}^{3} a_i P_i(q) \tag{20}$$

and the experimental data, where $P_i(q)$ is the form factor for a vesicle with modal inner radius R_i according with (19) weighted by a_i. Figure 1 shows the best fitting for the form factor (normalized by the value corresponding to 30º) of the PS vesicles used within this study and its optimum trimodal distribution, best agreement was reached for $\overline{\sigma} = 2R = 184$ nm. and 20% polydispersity. The previous DLS experiments commented above, averaging six individual measures, presented a similar value, $\overline{\sigma} = 2R = 179$ nm, for the same suspension.

In order to verify the initial liposomes concentration, we have followed the procedure by Haro-Perez et al. [28]. If we consider a homogeneous distribution of vesicles in space, we can define a typical distance, L, between a pair of neighbour particles associated to a volume fraction ϕ_v:

$$L = \left[\frac{\frac{4}{3}\pi R_{ext}{}^3}{\phi_v} \right]^{\frac{1}{3}}, \tag{21}$$

where R_{ext} is the mean external radius of the vesicles.

On the other hand, if the whole PS mass is forming vesicles, mass fraction, *x*, can be related with ϕ_v through:

$$\phi_v = \frac{x}{\frac{4\pi(R_{ext}{}^3 - R^3)}{3}\rho'} \frac{4\pi R_{ext}{}^3}{3}, \qquad (22)$$

where $\rho' = 1.015$ is the relative density PS/water [29].

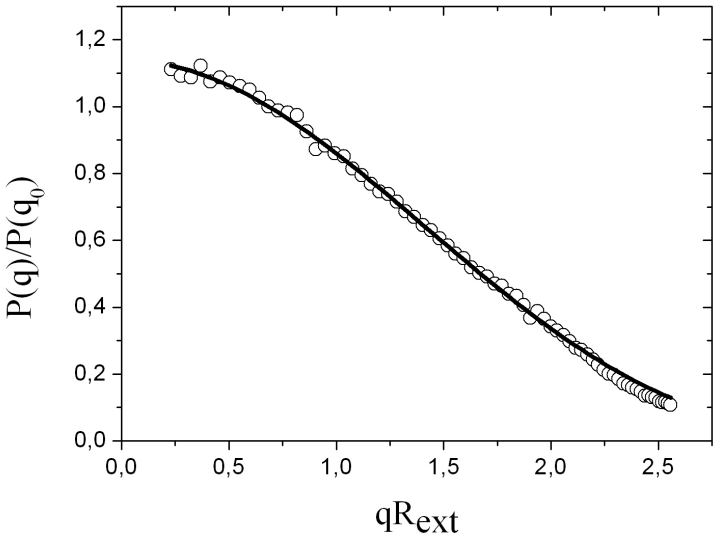

FIG.1 Normalized Form Factor *P(q)/P(q$_0$)*. Open circles stand for experimental values, according to $\langle I_0(q) \rangle \propto P(q)$, whereas solid line denotes the best trimodal fit given by Equation (20).

Although the structure factor contains the whole information of the interparticle distance distribution through its relationship with the pair correlation function, it is useful to give an interpretation in terms of *Bragg's law* for the interference peak in a non-aggregating and structured dispersion in order to check the expected value for the volume fraction from a known mass fraction. We have obtained the experimental structure factor corresponding to a mass fraction $x = 0.0031$, where three individual measures were done at each angle. Bragg's law gives *an experimental approach to the*

most frequent distance, L, for a pair of vesicles in the suspension related with a difference in phase, $\Delta\varphi$, for the field intensity scattered by them:

$$\Delta\varphi = q_m L = 2\pi \qquad (23)$$

The maximum value for $S(q)$ in the previous structure accounts for q_m= 0.0120 nm^{-1}, corresponding to $\phi_v = 0.0219$ using (21) and (23). By means of (22) we obtained $\phi_v = 0.0227$, where only a relative deviation of 3.5% comes out.

B. Experiment

The light scattering experiments presented in this paper were performed using a slightly modified Malvern 4700 System (UK) working with a 632.8 nm wavelength He-Ne laser. Aggregation was monitored simultaneously by SLS and DLS. For SLS experiments, the photomultiplier arm was previously located at the reference position in order to set the zero angle. After that, the mean scattered intensity was obtained for different angles in the range 10º-100º. For DLS experiments, the scattered intensity autocorrelation functions were determined at different times and a fixed angle of 90º during aggregation and registered by the same computer which controls the instrument. Data analysis was performed using our own computer software.

Aggregation was induced by adding electrolyte to the initially stable aqueous suspensions of liposomes. The water used for sample preparation was purified by inverse osmosis using Millipore equipment. The different electrolyte-particle mixtures were prepared by mixing equal amounts of buffered electrolyte solution and particle suspension through a Y-shaped mixing device in a cylindrical quartz glass cuvette. The electrolyte concentration was varied from 1mM to 7mM of $CaCl_2$.

The cluster fractal dimension was obtained by measuring the time-averaged scattered light intensity, $\langle I(q)\rangle$, as a function of the scattering vector. Inequality present in Expression (3) conditions the range for data interpolation, a correct choice for this range deserves explanatory comments. The q-range at which Expression (3) is strictly

accurate is $1/R_{aggr} << q << 1/R_{ext}$ (where R_{aggr} is the radius of the aggregate). However, in practice, a commonly accepted criterion to choose the highest q-value is $q_{max} \leq 1/R_{ext}$ whereas the election for the lowest q considers $q_{min} \geq 1/R_{aggr}$. This effective range ensures a non-incursion into Porod and Guinier regimes respectively [30].

For the DLS results obtained in this work, even in the most unfavourable case (2,5mM), the ratio $\overline{D}_{exp}/D_0$ is lower than 0,2 (when the fractal regime holds), this implies that, in a crude calculus, the corresponding R_{aggr} reaches about 1000 nm and $q_{min} \approx 0.001\, nm^{-1}$, in accord with the mentioned condition. In our experiments, the smallest value for the modulus of the scattering vector has been, in all cases, $q_{min} \geq 0.002\ nm^{-1}$, at which reliability is guaranteed. A right election for the interpolation interval discards possible misinterpretations between fractal dimensions closed to 2 (e.g. see Table I where d_f =1.91 at 2.5mM) and the exponent at the Guinier regime, which typically operates at $1/R_{aggr} >> q$.

TABLE I. Experimental Kinetic Exponents, Fractal Dimensions and van Dongen-Ernst homogeneity parameter.

$[Ca^{++}]$ (mM)	α	d_f	λ
2.5	0.85 ± 0.03	1.91 ± 0.07	0.38± 0.04
3.5	0.76 ± 0.02	1.84 ± 0.07	0.28± 0.04
5	0.54 ± 0.02	1.75 ± 0.06	-0.06± 0.07
7	0.52 ± 0.02	1.75 ± 0.05	-0.10± 0.08

$\langle I(q) \rangle$ measurements were performed for different electrolyte initial concentrations stopping the aggregation in an advanced stadium by diluting the original mixture under a non-aggregating electrolyte concentration, where a previous DLS experiment was done in order to probe the stabilization in time for the mean diffusion coefficient value.

Special attention has to be paid in order to determine the time required by an aggregating system to evolve to a stable state in which its self-similar growth becomes patent, reaching a constant value for the fractal dimension. The necessity to stop the aggregation is obviously imposed by the fact that a complete I(q)-scan takes additional time. In consequence, a rigorous measurement protocol has to be chosen. To determine the time at which the SLS-scan starts, we made previous experiments, for each sample, stopping the aggregation at different times in order to find out the *sufficient* time for which a permanent value for the fractal dimensions were verified. With the exception of the 2.5mM-sample, 1h. resulted enough in all cases for the initial monomeric concentrations. The results presented within this work were obtained for this self-similar aggregation stadium, according with the commented experimental protocol, averaging 10 I(q)-scans for each sample.

It is essential to confirm, when we deal with deformable and potentially fusionable particles, the permanence of the individuality, as well as the form, of the initial monomers during the aggregation process. The well correlated results obtained for the fractal dimension via SLS constitute themselves an indirect confirmation. We have to take into account that, according to expression (4), the detected signal for the aggregating system is normalized by the detected signal for the diluted system, in which only a monomer information is contained. The resulting signal will have the structural cluster information, with the expected potential behaviour, only if the initial monomers are still present in the clusters. In order to have additional evidence, parallel fluorescence experiments, based in the so-called ANTS/DPX assay [31], were performed. No significant reduction in the fluorescent intensity due to the quenching of ANTS by DPX was registered for the electrolyte and particle concentrations used within this work.

IV. RESULTS AND DISCUSSION

A. Liposome aggregation: Kinetic exponents

In a preliminary set of experiments, we found that aggregation took place for [$CaCl_2$] ≥ 2.5mM. For lower values, neither the diffusion coefficient nor the form factor underwent significant changes. At any rate, similar aggregation salt concentrations were reported by other authors [4]. Apart from that, we have determined the optimal liposome volume fractions to carry out aggregation experiments above this salt concentration, 0.15% for 2.5 and 3.5mM, and 0.08% for 5 and 7mM. The liposome volume fraction is a critical parameter from experimental point of view: it should be chosen to avoid too fast or slow aggregation kinetics.

Time resolved DLS was employed for monitoring the experimental average diffusion coefficient of the aggregates, $\overline{D}_{\exp}(t;q)$. In Figure 2, the time evolution of $\overline{D}_{\exp}(t;q)$ is plotted in a double logarithmic scale for [$CaCl_2$] = 2.5, 3.5, 5 and 7mM. The curve decreases as time increases and is characterized by a power law at large times. This suggests that the cluster size distribution may be described by the dynamic scaling approach in this time interval. As can be observed, the data align on a straight line even for quite small clusters. This observed power law, $\overline{D}(t;q) \sim t^{-\alpha}$, is also obtained in all cases. Accordingly the α parameters were obtained by fitting the experimental data. Table I contains the obtained values. It should be pointed out that the values for 5-7mM are in good agreement with the theoretical prediction given for the diffusion regime ($\alpha = 1/d_f \approx 0.57$, since $d_f = 1.75$ is widely accepted for DLCA) [32, 33]. DLCA is considered as the result of the absence of a repulsive barrier of potential between particles in which aggregation happens at any contact due to an attractive well between the particles, typically operating at very short distances. Regarding the kinetic exponent, α, this parameter decreases with increasing the salt concentration, reaching a stable value at 5mM.

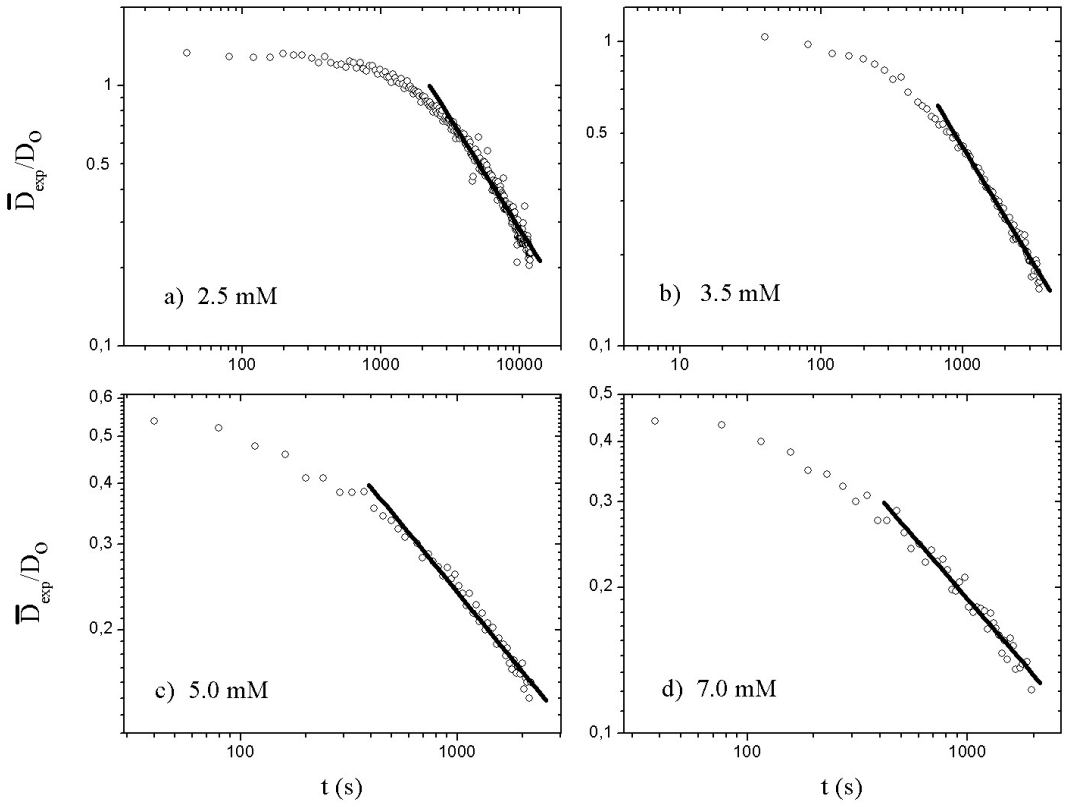

FIG.2 Normalized experimental mean diffusion coefficient $\overline{D}_{exp}/D_0$ as a function of time for: a) 2.5mM; b) 3.5mM; c) 5mM; d) 7mM. Open circles stand for experimental values whereas solid lines denote the asymptotic fit according to (14).

B. Liposome aggregation: Fractal dimension

Although an implicit *single scattering* assumption is considered in the determination of fractal dimensions via SLS, it is clear that any monomer inside an aggregate scatters a field proceeding from the incident beam radiation in addition with the fields scattered by the rest of the monomers in the cluster. The relevance of this *intra-cluster multiple scattering* yields to a coupled problem that still remains open. A complete theoretical approach to this problem would involve the size and geometry of the aggregates, as well as the monomers, the optical properties of the scatterers (through their refractive index) and the wave length of the incident light [30]. Early theoretical work by Chen et al. [34] shows no influence due to multiple scattering for the measurement of fractal dimensions

through the potential behavior of $S(q)$ for the range considered in Eq. (4), even for $d_f > 2$. This theoretical prediction was experimentally confirmed by Lattuada et al. [35] for clusters and monomers comparable in size and refractive index to the particles used within this work (n=1.36 [36]). Additionally, efficiency of SLS essays to determine fractal dimensions has been proven for aggregating suspensions of polystyrene latexes, involving large clusters and particles, in which the refractive index of the scatterer particles is considerablely greater (n=1.49) [37,38]. These experimental accesses confirm the values for the fractal dimension obtained by computer simulations, which are not related with light scattering, under rapid and slow aggregation regimes. Apart from that, we consider the experimental *convergence* to a DLCA fractal dimension ($d_f \approx 1.75$) as an indication of self-consistency for a SLS essay under our suspension conditions, providing the single scattering assumption.

Having determined the structure factor from light scattering data (Eq. (4)), d_f was obtained by fitting the experimental data to the power law given in Eq.(3). Good agreement was reached in all cases. Figure 3 shows typical plots of the structure factor for $[CaCl_2]$ = 2.5, 3.5, 5 and 7mM. It can be clearly seen that this function presents a functional behaviour from which the cluster fractal dimension can be easily obtained. In Table I the fractal dimensions estimated at different electrolyte concentrations are summarized. As can be concluded, the fractal dimension decreases with increasing electrolyte concentration and ranges from 1.91 to 1.75. It should be noted that the latter fractal dimension is the well established value for DLCA regime so, at 5-7mM, the liposomes have reached such regime and form ramified open structures. For lower salt concentration, more dense structures will be formed, as the increase in fractal dimension reveals (1.84-1.91).

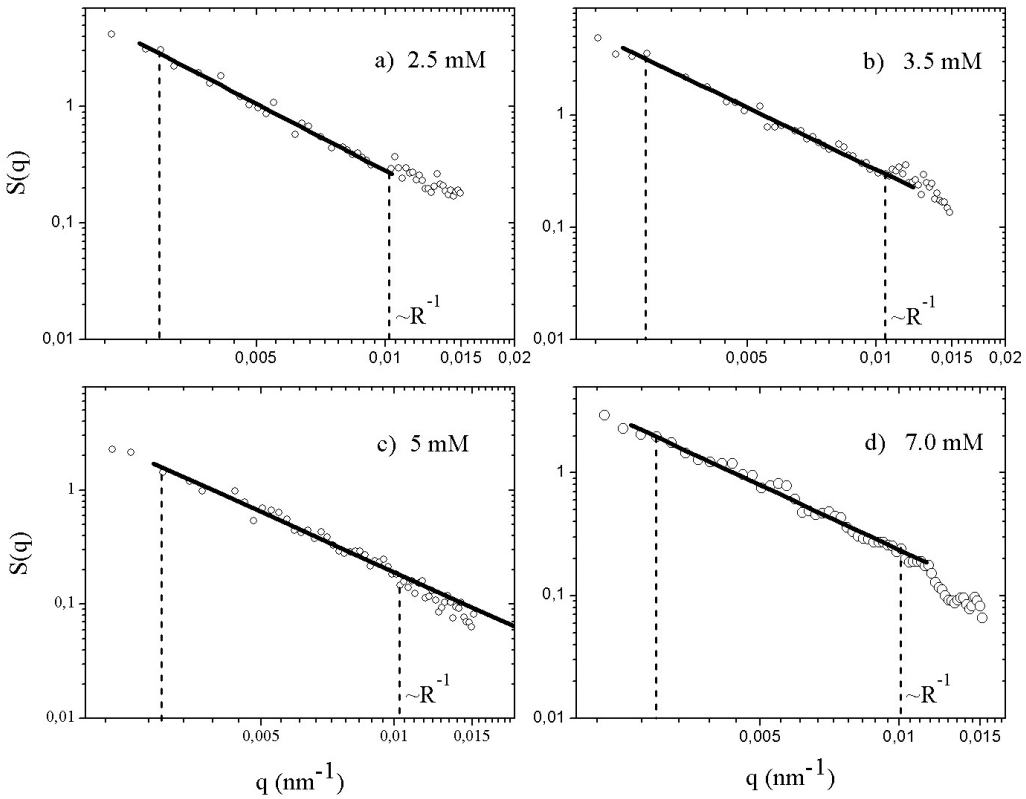

FIG.3 Structure Factor *S(q)* for: a) 2.5mM; b) 3.5mM; c) 5mM; d) 7mM. Experimental values (open circles) result from Equation (4). Solid lines represent the theoretical fit according to the expected behaviour given by (3). Vertical dash lines denote the interpolation q-ranges.

Consequently, SLS experiments provide us a direct access to the aggregate structure and a clear observation of the different aggregation regimes. In a previous work by Lynch *et al.*, a fractal dimension value was reported by fitting the time evolution of turbidity protein-induced liposome aggregation although these authors did not analyze the aggregate morphology.

Once the α parameter is known, and using the fractal dimension obtained from independent SLS experiments, the homogeneity λ parameter was determined by (14). The results are also summarized in Table I. For the 5 and 7mM, the λ value is practically 0 within the experimental uncertainty. This is the well-accepted value for DLCA kinetics. The λ-values between 0.3 and 0.4 point towards a relatively slow aggregation kinetics.

C. Liposome aggregation: Time evolution of the diffusion coefficient

The values of fractal dimensions obtained in the preceding section will be used as input in our time evolution model, which involves the resolution of Smoluchowski's equation. As mentioned in the theoretical background, we are assuming $d_h \approx d_f$. Such assumption is well admitted for hard particles (see, for instance, references [21,22]). Although no experimental contrast has been reported in that way for liposomes, however, we have found that the vesicle sizes determined by static light scattering and dynamic light scattering are practically identical, which suggests that the liposome flexibility does not affect the diffusive behavior of the monomers. On the other hand, the fluorescence assays (mentioned above) points to the absence of fusion after aggregation, that is, monomers conserve their individuality inside the aggregates. Regarding the good correlation for the results of the SLS experiments, the form factor of the monomers appears to be contained in the signal scattered by the aggregating system. Therefore, in the light of our experiments, liposomes aggregates seem to behave as hard objects structures (for which this assumption holds).

The experimental values for λ and d_f obtained above for 5-7mM suggest a DLCA regime while a slow regime can be assumed for smaller salt concentration values. At this point we are going to corroborate these features for the whole time evolution with the appropriated kernel model at Smoluchowski's rate equation.

First, we describe the numerical calculation procedure used here. The existence and uniqueness for the solution of Smoluchowski´s equation depend on the election for the kernel and the initial condition. For the different proposed kernels, a normalized evolution problem was resolved in terms of the relative concentrations, $X_n(T) = N_n(T)/N_1(0)$, where $T = t\,(N_1(0)k_{11}/2)$, $K_{ij} = 2k_{ij}/k_{11}$ and initial monomeric conditions were assumed:

$$\frac{dX_n(T)}{dT} = \frac{1}{2}\sum_{i+j=n} K_{ij} X_i X_j - X_n \sum_{i=1}^{\infty} K_{in} X_i, \quad \left(\vec{X}(0) = (1,0,...)\right) \tag{24}$$

In order to obtain the master curve ($\vec{X}(T)$), which is associated to a $\{d_f,\lambda\}$ input and solution to this dimensionless problem, numerical calculations were carried out by cutting off the number of equations, *Nc*, for the previous system, taking under consideration the error related with the non-computed equations. In order to neglect this cutting-off error, the conservation for the number of monomers was imposed within the whole integration process. This conservation condition can be expressed as:

$$abs\left(\sum_{i=1}^{Nc} iXi(T) - 1\right) \leq \varepsilon \approx 0, \forall T \tag{25}$$

being ε the imposed accuracy. The numerical algorithm was based in a Runge-Kutta fourth-order explicit iterative method.

The estimation for the numerical diffusion coefficient, $\overline{D}_{num}(t;q)$, was done according to light scattering theory in which $\overline{D}(q)$ may be expressed, at any time, as

$$\overline{D}(q) = \frac{\sum_{n=1}^{Nc} b_n(q) D_n}{\sum_{n=1}^{Nc} b_n(q)}, \tag{26}$$

where $b_n = N_n n^2 S(qR_g)$ and $S(qR_g)$ is the structure factor of an n-particle aggregate with radius of gyration R_g [15]. In literature, several functional forms for $S(qR_g)$ can be found. The main difficulty lies in obtaining an expression for the structure factor valid for the whole range $qR_g > 1$. We adopt the expression calculated by Lin et al. [39] directly from computer generated clusters obtained under diffusion and reaction limited conditions.

In order to compare experimental data for the diffusion coefficient $\overline{D}_{\exp}(t;q)$ with those obtained from the expressions (26) and the solution of (24) for $\overline{D}_{num}(t;q)$, a transformation between the normalized time in the numerical model into the real one for

the experimental data should be done. The relationship must adopt the form of an afin transformation,

$$T = m\,t + n, \tag{27}$$

where $m = N_1(0)k_{11}/2 \equiv t_{agg}^{-1}$, t_{agg} is the so called *aggregation time* and *n/m* gives us the possible delay between the start of the experimental measure and the start of the aggregation process. The values for *m* and *n* were determined by imposing the minimum distance between numerical and experimental data through their mean quadratic error over the whole time evolution. This optimization problem takes the form:

$$\min_{m,n} E(m,n) = \min_{m,n} \sum_i (\bar{D}_{num}(mt_i + n) - \bar{D}_{\exp}(t_i))^2 \tag{28}$$

According to λ and d_f values obtained, we will analyze the results for 5mM as a representative case of DLCA regime using the Brownian kernel. Figure 4 shows a good accord between the theoretical curves and the experimental data in the whole time range. This best fitting between numerical and experimental data corresponds to $k_{11} = k_{11}^{Brown} = (9.3 \pm 1.1)10^{-20}\, m^3 s^{-1}$. Although this value agrees with those determined by other authors for liposomes [40], it is significantly smaller than the value predicted from Smoluchowski's *diffusion* model [17, 18] and obtained for other systems (latexes). This model assumes that free diffusion works at distances larger or equal than 2*a* (i.e., geometrical contact). Our λ- and d_f -data suggest that this hypothesis is valid at large distances. In our opinion, however, the disagreement mentioned above might be due to the fact that this free diffusion model is not properly working at short distances for liposomes. Although the scope of this paper does not go beyond the geometrical and kinetic properties, this result points to differences in the interaction mechanisms between liposomes and other model systems at short distances.

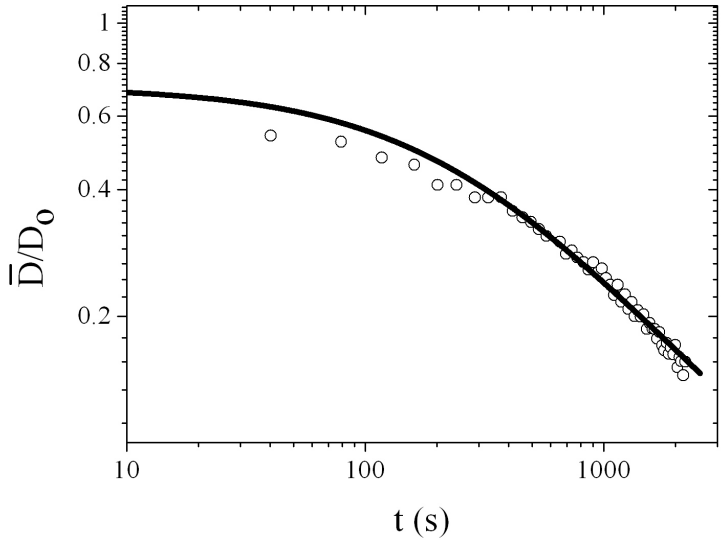

FIG.4 Normalized mean diffusion coefficient $\overline{D}/D_0$ as a function of time (5mM).Solid line shows the numerical solution for Smoluchowski's Equation assuming the Brownian Kernel. Open circles denote the experimental values.

Now we will investigate a first case of slow aggregation regime (3.5mM). Figure 5 shows the experimental data and three different theoretical fittings. As expected the solution obtained using the Brownian kernel is not able to capture the asymptotic behaviour. In the attempt to improve the agreement between experimental data and the theoretical model, the MC kernel given by the expression (17) was applied. Here d_f =1.84 and d_{fD} =1.75. Certain improvement is achieved but at very large times the agreement is still rather poor. Taking into account the general slow aggregation model given by (16) in which $\lambda=2\beta$ and having experimental access to λ, we explore if using this value, a complete description over the whole time range can be done. This is somewhat logical since the experimental λ successfully captures the asymptotic behaviour. This result (with λ = 0.28) is also plotted in figure 5. As can be seen, the agreement is considerably improved. In this case, $k_{11} = (3.6 \pm 0.4)10^{-20} m^3 s^{-1}$, which implies $p_{11} = k_{11}/k_{11}^{Brown} = 0.32 \approx 1/3$. These quantities are of the order of those reported by other authors practically at the same conditions [41]. p_{11} can also be interpreted in terms of a energy barrier with the help of the Arrhenius equation. In this case, such barrier would be of the order of $\frac{3}{2}k_B T$ (where k_B is Botlzmann's constant and T the absolute temperature). In fact, a slow aggregation regime is characterized by a

residual repulsive barrier with height comparable to the mean kinetic energy of the reacting particles.

Concerning the other slow aggregation (2.5mM), the same fittings as those mentioned previously were tried. Unfortunately, the accord was not so good. In our opinion, this bad description comes from the possibility of fragmentation, which is not accounted for Smoluchowski's approach considered here.

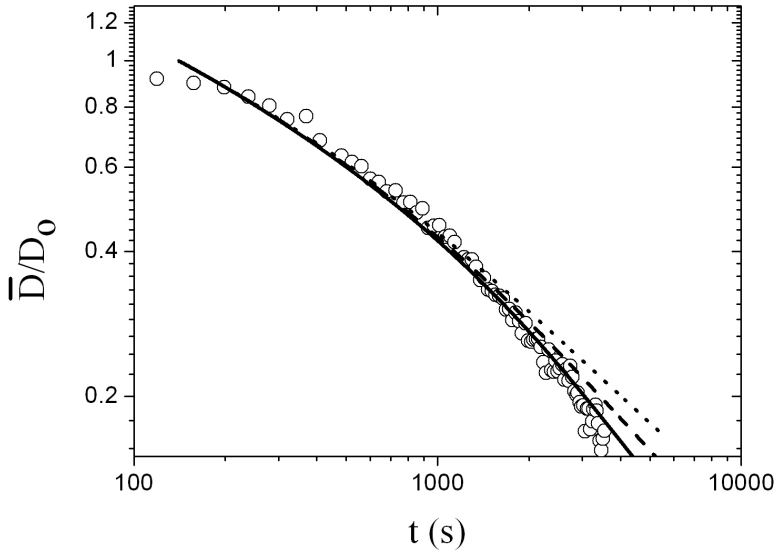

FIG.5 Normalized mean diffusion coefficient $\overline{D}/D_0$ as a function of time (3.5mM). Three numerical solutions for Smoluchowski's Equation are plotted: Dot line for the Brownian Kernel, Dash line for MC Kernel, (17), and solid line for the general slow aggregation kernel, (16), using the experimental value obtained for β. Open circles denote the experimental values.

V. CONCLUSIONS

The aggregation of PS liposome dispersions has been studied in terms of the fractal dimension and the homogeneity parameter of the van Dongen–Ernst. Cluster structure and aggregation kinetics found at 5-7mM of divalent Ca indicate that the DLCA regime was reached. For these salt concentrations, the Brownian kernel was able to describe the time evolution of the effective diffusion coefficient. For lower calcium concentrations,

the fractal dimension and the homogeneity parameter suggest a transition from DLCA to a slow aggregation regime.

The Brownian kernel does not explain the whole time evolution of the effective diffusion coefficient for the slow kinetics. Although the multiple contact kernel improves the predictions, a slightly modified kernel is required. In this framework, an alternative procedure to determine the dimerization constant has been put forward in both rapid and slow cases. The values here obtained are in good agreement with others reported previously by different methods.

ACKNOWLEDGEMENTS

The authors are grateful to "Ministerio de Educación y Ciencia, Plan Nacional de Investigación, Desarrollo e Innovación Tecnológica (I+D+i)", Projects MAT2006-12918-C05-01 -02, and -04, the European Regional Development Fund (ERDF) and "Consejería de Innovación, Ciencia y Tecnología de la Junta de Andalucía" (Project FQM-392 and incentives for research groups) for financial support. A. M.-M. also thanks the "Programa Ramón y Cajal, 2005, Ministerio de Educación y Ciencia (RYC-2005-000829)".

Reference List

[1] Cesv G. Biochim.Biophys. Acta **311**:1031-3 (1990).

[2] Barenholz, Y. Curr. Opin. Colloid Interface Sci. **6**: 66 (2001).

[3] Chrai, S. S., R. Murari, and I. Ahmad. Biopharm-the Applied Tech. Biopharm. Development **15**: 40 (2002).

[4] Nir, S. et al. Progress Surface Sci. **3**: 1 (1983).

[5] Bentz, J. and H. Ellens. Colloids and Surfaces **30**: 65 (1988).

[6] Blumenthal, R. et al. Chemical Reviews **103**: 53 (2003).

[7] Lasic D.D. "Handbook of Biological Physics" (London: Elsevier, 1995).

[8] Wilschut, J., N. Duzgunes, and D. Papahadjopoulos. Biochemistry **20**: 3126 (1981).

[9] Bordi, F. et al. Biophys. J. **91**: 1513 (2006).

[10] Lynch N. J., P. K. Kilpatrick and G. Carbonell. Biotechnol. Bioeng. **50**: 151(1996).

[11] Stauch O. and R. Schubert. Biomacromolecules **3**: 565 (2002).

[12] Schmitt, A. et al. Physical Rev.E **62**: 8335 (2000).

[13] Odriozola, G. et al. J. Colloid Interface Sci. **240**: 90 (2001).

[14] Vicsek T. "Fractal Growth Phenomena". (World Scientific, 1988).

[15] Lin, M. Y. et al. J. Phys.Condens. Matter **2**:3093 (1990).

[16] Koppel, D. E. J. Chem. Phys. **57**: 4814 (1972).

[17] Smoluchowski M.Z. Phys.Z.**17**: 557 (1916).

[18] Smoluchowski M.Z. Phys.Chem. **92**:129 (1917).

[19] van Dongen, P. G. J. and Ernst M. H. J.Stat.Phys. **50**: 295 (1988).

[20] van Dongen, P. G. J. and Ernst M. H. Phys. Rev. A.**32**: 670 (1985).

[21] Meakin, P., Z. Y. Chen, and J. M. Deutch. J. Chem. Phys. **82**: 3786 (1985).

[22] Pusey, P. N. and J. G. Rarity. Mol. Phys. **62**: 411 (1987).

[23] Broide M.L. Ph.D. Thesis. Massachusetts Institute of Technology, (1988).

[24] Hope, M. J. et al. Biochimica et Biophysica Acta **812**: 55 (1985).

[25] Roy, M. T., M. Gallardo, and J. Estelrich. Bioconjugate Chemistry **8**: 941(1997).

[26] D'Aguanno, B. and Klein R. J.Chem.Soc.Faraday Trans.**87**: 379 (1991).

[27] D'Aguanno, B. and Klein R. Phys. Rev. A.**46**: 7652 (1992).

[28] Haro-Perez, C. et al. J. Chem. Phys. **119**: 628 (2003).

[29] Lasic D.D. "Liposomes: From Physics to Applications" (Amsterdam: Elsevier,1991).

[30] Sorensen, C.M. "Light Scattering by Fractal Aggregates: A review". Aerosol Sci. Technol., **35**: 648 (2001).

[31] Düzgünes, N. Bagatolli L. A. Meers P. Oh J-K Straubinger R. M. "Liposomes. A Practical Approach." (Oxford University Press, 2003).

[32] Meakin, P. Phys. Rev. B **29**: 4327 (1984).

[33] Kolb, M. Phys. Rev. Lett. **53**: 1653 (1984).

[34] Chen, Z. et al. Physical Rev. B **37**: 5232 (1987).

[35] Lattuada, M., Wu, H., Morbidelli, M. Phys. Rev. E **64**: 61404 (2001).

[36] Haro-Perez, C. Ph.D. Thesis. Universidad de Granada (2005).

[37] Tirado-Miranda, M. et al. Phys. Rev.E **67**: 11402 (2003).

[38] Tirado-Miranda, M. et al. Colloids and Surfaces A **162**:67 (2000).

[39] Lin, M. Y. et al. Phys. Rev. A. **4**: 2005 (1990).

[40] Nir,S., Wilschut, J. and Bentz, J.. Biochim. Biophys. Acta **668**:275 (1982).

[41] Day, E. P., Kwok, A. Y. W., Hark, S. K., Ho, J. T., Vail, W. J., Bentz, J. and Nir, S.. Proc. Natl. Acad. Sci. USA **77**:4026 (1980).

Paper IV

Surface Fractals in Liposome Aggregation

Surface Fractals in Liposome Aggregation

Sándalo Roldán-Vargas[1], Ramon Barnadas-Rodríguez[2,3], Manuel Quesada-Pérez[4], Joan Estelrich[2], José Callejas-Fernández[1]

[1]Grupo de Física de Fluidos y Biocoloides, Departamento de Física Aplicada, Universidad de Granada, E-18071 Granada, Spain.

[2]Departament de Fisicoquímica, Facultat de Farmàcia, Universitat de Barcelona, E-08028 Barcelona, Catalonia, Spain.

[3]Centre d'Estudis en Biofísica, Facultat de Medicina, Universitat Autònoma de Barcelona, E-08193 Cerdanyola del Vallès Bellaterra, Barcelona, Catalonia, Spain.

[4]Departamento de Física, Escuela Politécnica Superior de Linares, Universidad de Jaén, Linares, E-23700 Jaén, Spain.

Abstract

In this work, the aggregation of charged liposomes induced by magnesium is looked into. Static and Dynamic Light Scattering, Fourier-Transform Infrared Spectroscopy, and Cryo-Transmission Electron Microscopy are used as experimental techniques. In particular, multiple intracluster scattering is reduced to a negligible amount using a cross-correlation light scattering scheme. The analysis of the cluster structure, probed by means of static light scattering, reveals an evolution from surface fractals to mass fractals with increasing the magnesium concentration. Cryo-Transmission Electron Microscopy micrographs of the aggregates are consistent with this interpretation. In addition, the comparative analysis of these results with those previously reported in the presence of calcium suggests that the different hydration energy between lipid vesicles when these divalent cations are present plays a fundamental role in the cluster morphology. This suggestion is also supported by Infrared Spectroscopy data. The kinetics of the aggregation processes is also analyzed through the time evolution of the mean diffusion coefficient of the aggregates.

I. INTRODUCTION

Aggregation of mesoscopic biological objects such micelles, vesicles, and large macromolecules has generally a great relevance: In Physics, it could shed light on the relationship between structure and kinetics of the aggregates with the relative strength of diverse interaction forces (electrostatic, magnetic, steric, depletion, ...). In Biology, knowledge of the interaction mechanism at short distances between these objects immersed in an electrolyte solution is a key to elucidate essential biological processes involved in many cellular phenomena, e.g. membrane fusion [1, 2]. Here, we focus on the morphological and kinetic aspects of the aggregates formed by liposomes made of phosphatidilserine (PS), which is the major anionic phospholipid of many cell membranes.

Fractal Geometry can be used to describe the morphology of the clusters through the measurement of their fractal dimension [3]. In this framework, many of the morphologies formed in aggregating colloidal systems have been identified as *mass fractals*: Their mass M scales with their radius R as $M \propto R^{d_m}$ $(d_m < 3)$, d_m being the *mass fractal dimension*. In this way, more or less branched clusters $(1.75 \le d_m \le 2.1)$ has been reported in irreversible aggregation [4] whereas dense cluster structures have been documented, even with $d_m > 2.5$, when internal restructuring is allowed [5,6]. In particular, it is a common place to speak of *dense* morphologies when d_m is larger than 2.5. In that case, the underlying physics of this high d_m values has been rarely explored. Moreover, we suspect that some of these large d_m could be attributed to a wrong interpretation of the experimental data, due to the non-considered effect of the multiple scattering on the experimental determination of the fractal dimensions of dense objects.

In addition to mass fractals, another class of dilation symmetry has been described for uniform structures $(d_m \to 3)$ limited by a fractal rough surface S which scales with the radius of the object as $S \propto R^{d_s}$ $(2 < d_s < 3)$ [7]. These objects are known as *surface*

fractals and d_s is their *surface fractal dimension*. In literature, and from an experimental viewpoint, it is difficult to find aggregation phenomena (or others related to them) described using the concept of *surface fractal*. A noticeable exception is the work of Keefer and Shaefer [8] on the growth of silicate particles in solution.

In a recent study on PS liposome aggregation induced by calcium, a transition from $d_m = 1.91$ to $d_m = 1.75$ for the mass fractal dimension of the resulting structures was observed, by means of Static Light Scattering (SLS), when the calcium concentration increased from 2.5 to 5 mM. A convergence to a diffusion-limited cluster aggregation (DLCA) regime, $d_m = 1.75$, was also experimentally documented [9]. More recently, we have described in a short communication a transition from surface fractal to mass fractal structures in a suspension of aggregating liposomes using the divalent cation Mg^{2+} as aggregating agent [10]. This change in the morphology of the clusters is controlled by the amount of magnesium added and shows a final stable value of the mass fractal dimension appreciably larger, $d_m = 2.6 - 2.7$, than that corresponding to the DLCA regime previously documented in our calcium study.

In this paper, a considerably detailed description and analysis of both structural and kinetic aspects of this surface- to mass-fractal transition controlled by the magnesium concentration are presented. The interaction energies involved in these aggregation processes are also discussed in the light of the experimental data. In this way, the previous report [10] is fairly completed. From the experimental point of view, the influence of the Multiple Intracluster Scattering (MIS) and polydispersity of the aggregates on the measured fractal dimensions are widely discussed. The morphologies revealed by our SLS study are also supported by Cryo-Transmission Electron Microscopy (Cryo-TEM) micrographs. At the same time, our analysis of the aggregation phenomenon is completed with a study of the aggregation kinetics. To do that, the experimental time evolution of the mean cluster diffusion coefficient is measured by means of Dynamic Light Scattering (DLS) and compared with the theoretical result obtained from the resolution of Smoluchowski´s equation.

Discussing the influence of the total interaction energy between liposomes on the resulting cluster morphologies, we will also argue why the classical Derjaguin-Landau-Verwey-Overbeek (DLVO) theory (which only considers the Coulomb and van der Waals interactions [11, 12]) is not suitable in this case. In this respect, it is well known in biophysics that the phospholipid head groups belonging to the surface of the lipid vesicles are more or less hydrated. Thus, a hydration energy may appear. In fact, some authors claim [13-15] that this hydration interaction energy could play a key role in the liposome aggregation. Hence, we decided to analyze the dehydration effect due to magnesium and calcium ions from Fourier-Transform Infrared Spectroscopy (FTIR). This analysis suggests that the hydration grade of the lipid molecule in presence of these two divalent cations plays an essential role in the vesicles short-range interaction mechanism and conditions the resulting cluster morphology.

The rest of the paper is organized as follows: First, the theoretical background is outlined. Section III contains a detailed description of the experimental procedures and methods. Then, the main results of the work and the corresponding discussion are presented and, finally, some conclusions of this research are highlighted.

II. BACKGROUND

A. Surface and mass fractals: Concept and measurement

In a pioneering work, Pfeifer and Avnir proposed the application of Fractal Theory to characterize heterogeneous chemical surfaces [7]. In that investigation, surfaces with different degrees of irregularity (roughness) were labelled by a real number d, where $2 < d < 3$, if certain conditions were satisfied.

Let us specify these conditions by considering the usual ball-covering process of a rough surface in three-dimensional space, i.e. the covering of the whole surface with the minimal number $N(r)$ of balls of radius r providing that any point of the surface will

be included in at least one of the balls. It is clear that with decreasing r the number $N(r)$ grows generally in a non-trivial fashion. If the covering process satisfies the existence of the limit:

$$\lim_{r\to 0} - \frac{\log N(r)}{\log r} = d \quad ; \quad d \in (2,3), \qquad (1)$$

the surface will be called *fractal surface* and its roughness, which is persistent at different spatial scales, will be described by d, the *surface fractal dimension*. If the fractal surface under consideration is closed and it defines the boundary of a completely compact three-dimensional object (a "walnut" [16]), this object will be called *surface fractal*, having a surface fractal dimension d. Therefore, from these definitions, the distinction between a fractal surface and a surface fractal is evident (for more details see Ref. [17]).

If we associate a characteristic length to our surface fractal, e.g. its radius of gyration R, an equivalent expression for (1) can be found if we dilate the object by a growing factor, keeping constant the radius r of the covering balls. Then, asymptotically ($R \to \infty$):

$$S = K R^d \quad (2 < d < 3), \qquad (2)$$

where S is the covering surface of the surface fractal and K is a positive real number. Accordingly, from $d \to 2$ (smooth surface) the roughness of a surface fractal increases with increasing d.

Certainly, as it is well known, the process described above can be extended to the covering of the volume of a three-dimensional object which in general will not be completely compact. If we start now the covering process in an inner point of the object and we continue our covering from this point by increasing the distance R, remaining always inside the object, we shall called this object a *volume* or *mass fractal* if the

covering volume V scales as:

$$V = R^d \quad (0 < d < 3) \tag{3}$$

Similarly, d, called now *mass fractal dimension*, is an estimation of the compactness (not the roughness) of the mass fractal: from $d \to 3$ (uniform object), the compactness of a mass fractal decreases with decreasing d.

Nevertheless, it must remain clear that two different surface fractals show only different fractal properties on their boundaries whereas their interiors are uniform. Then, for clarity, we shall identify by $d_s = d$ the fractal dimension corresponding to definition (2) and by $d_m = d$ when it corresponds to (3). With this notation, a surface fractal will be always described by $2 < d_s < 3$ and $d_m = 3$.

In order to probe the emergence of fractal structures in colloidal aggregation as those described by (2) or (3), a widely used technique is Static Scattering in its different versions (X-rays, neutrons or light). In this sort of measurements an experimental value of the structure factor $S(q)$ of the analyzed sample is accessible [18]:

$$S(q) = \frac{1}{N}\left\langle \sum_{i=1}^{N}\sum_{j=1}^{N} \exp\left(i\vec{q}\cdot(\vec{r}_i - \vec{r}_j)\right)\right\rangle, \tag{4}$$

where $\vec{q}$ is the scattering vector, $\vec{r}_i$ and $\vec{r}_j$ represents the positions of i and j-th scatterers, N is the number of particles (scatterers), and $\langle\cdots\rangle$ represents the ensemble-averaged value. Thus, the term $\vec{q}.(\vec{r}_i - \vec{r}_j)$ informs if the scattering waves combine constructively or randomly at the detector. Then, $S(q)$ reveals, through its q-dependence, the structure of the system. Here we focus on the light scattered by a system of aggregates constitute of colloidal particles.

From a general point of view, the fractal nature of a structure within a given spatial scale is proved by a "power law" dependence of $S(q)$ within a given q-range. Thus, if a structure presents a fractal nature between two characteristic lengths, a "power law" dependence of $S(q)$ is expected when q^{-1} is included between these characteristic lengths. In this respect, and in order to test the fractal nature of rough surfaces, Bale and Schmidt [19] were the first to propose a functional behavior for $S(q)$, applying their model to the study of lignite coal. On the other hand, starting from the work of Schaefer and co-workers [20], several experimental studies have been performed in order to prove the structure of mass fractals. A compendium of their results is:

$$S(q) \propto q^{-\alpha} \quad , \qquad (5)$$

where $\alpha = d_m$ $(Mass\ Fractals)$ and $\alpha = 2d_m - d_s = 6 - d_s$ $(Surface\ Fractals)$.

In the case that the fractal structures are aggregates of representative radius R made of subunits of characteristic radius a, expression (5) will be typically satisfied within $R^{-1} << q << a^{-1}$.

From a physical point of view, the scattering phenomenon comes from the fluctuations in the density of the scatterers. In a mass fractal, essentially all the primary particles are on the surface, there are not inner particles, and the density fluctuations come from any point of the structure. In a surface fractal, only a fraction of the primary particles belong to the surface, the rest are inner particles. In this kind of fractal, internal fluctuations do not contribute significantly to the scattered intensity [21].

B. Structure factors in aggregated systems: Effect of the multiple scattering

In a lighted colloidal dispersion, a fraction of the incident photons is scattered twice or more in passing through the sample, which is known as Multiple Scattering. This phenomenon is always present even though the initial non-aggregated suspension is

diluted enough, having a small concentration of "scatterer material", i.e. when First Born approximation is satisfied [4, 22]. In aggregation, however, the light scattered by an aggregate is rarely scattered again by others if the suspension is sufficiently diluted. In contrast, multi-reflections inside the aggregates do take place. This is called Multiple Intracluster Scattering (MIS). To clarify the incidence of this MIS on the determination of fractal dimensions, great efforts have been done from theoretical and experimental point of views, at least for mass fractal, see for instance [21, 23, 24]. In this respect, experimental designs based on cross-correlation schemes [25-27] have proved to be successful reducing to a negligible amount the Multiple Scattering in stabilized dense colloidal suspensions. Here we provide a basic theoretical description of one of these schemes, three-dimensional dynamic light scattering (3D-DLS) [26], which will be applied to an aggregating system. This description has been essentially adapted from [28].

Accordingly, two laser beams with equal wavelength and intensities coming from above and below of an average scattering plane are focused onto a colloidal dispersion. At the same time, a digital correlator computes the cross-correlation function of the scattered intensities registered by two detectors (1 and 2) which are positioned at an equal scattering angle (i.e. they are positioned at an equal q-value). For a dilute a non-aggregated system, the time-averaged single scattered intensity $< I_{1,2}^{0}(q) >_{Single}^{volume}$ coming from the scattering volume is:

$$< I_{1,2}^{0}(q) >_{Single}^{volume} = A_{1,2}\, \phi\, P(q) \quad , \tag{6}$$

where $A_{1,2}$ includes the incident laser intensities and other constants of proportionality whereas ϕ and $P(q)$ are the particle volume fraction and the form factor of the primary particles respectively. Similarly, for a dilute aggregated system, the corresponding timeaveraged single scattered intensity coming from the scattering volume, denoted now by $< I_{1,2}^{a}(q) >_{Single}^{volume}$, results:

$$< I_{1,2}^{a}(q) >_{Single} = A_{1,2}\, \phi\, P(q)\ S(q) \ , \tag{7}$$

where $S(q)$ is the Structure Factor of the aggregated system.

By virtue of the statistical properties of the scattered signal, $< I_{1,2}^{system}(q) >_{Single}^{volume}$ $(system \in \{a,0\})$ can be factorized as a product of the registered signals: $< I_{1,2}^{system}(q) >_{Single}^{volume} = \sqrt{< I_1^{system}(q) >_{Single}^{volume} < I_2^{system}(q) >_{Single}^{volume}}$, $< I_i^{system}(q) >_{Single}^{volume}$ being the time-averaged single scattered intensity coming from the scattering volume and registered at detector i ($i = 1$ or 2). Then we would obtain $S(q)$ from expressions (6) and (7):

$$S(q) = \sqrt{\frac{< I_1^a(q) >_{Single}^{volume} < I_2^a(q) >_{Single}^{volume}}{< I_1^0(q) >_{Single}^{volume} < I_2^0(q) >_{Single}^{volume}}} \qquad (8)$$

Note that ϕ was removed because the initial and the aggregated samples have identical particle volume fractions.

However, on propagating from the scattering volume to the wall of the scattering cell, the scattered signals suffer attenuation and only a fraction of the scattered photons will reach the detectors. This fraction is accounted for the system's transmission coefficient $T_i^{system} = \frac{< I_i^{system}(q) >_{Single}^{out}}{< I_i^{system}(q) >_{Single}^{volume}}$, where $< I_i^{system}(q) >_{Single}^{out}$ is the time-averaged single scattered intensity that would reach detector i after the attenuation effect. At the same time, although the structure and form of the primary particles are related through (6) and (7) to the single scattered intensities, in practice we detect a mixture of intensities (single + multiple). Although we do not have a direct access to the single scattered intensities, a cross-correlation scheme as 3D-DLS allows us to obtain the ratio between the required single intensities and the total measured intensities as it will be discussed in section III.C. This ratio is represented by $\left[\beta^{system}(q)\right]^2$:

$$\left[\beta^{system}(q)\right]^2 = \frac{< I_1^{system}(q) >_{Single}^{out} < I_2^{system}(q) >_{Single}^{out}}{< I_1^{system}(q) >< I_2^{system}(q) >} \quad , \qquad (9)$$

where $< I_i^{system}(q,t) >$ is the total (single + multiple) time-averaged intensity registered at detector i for a given system. Therefore $\beta^{system}(q)$ computes the contribution of the Multiple Scattering. It is clear that for a dilute system $\beta(q) \approx 1$.

Substitution of equation (9) and $T_i^{system} = \dfrac{< I_i^{system}(q) >_{Single}^{out}}{< I_i^{system}(q) >_{Single}^{volume}}$ in equation (8), finally gives:

$$S(q) = \sqrt{\frac{< I_1^a(q) >< I_2^a(q) >}{< I_1^0(q) >< I_2^0(q) >}} \sqrt{\frac{T_1^0}{T_1^a}\frac{T_2^0}{T_2^a}} \frac{\beta^a(q)}{\beta^0(q)} \qquad (10)$$

Thus $S(q)$ is expressed in terms of measurable quantities.

C. Aggregation kinetics

Regarding the aggregation kinetics, it is possible to consider the movement of an aggregate as a solid body by distinguishing a rotational and an isotropic translational diffusion. For the q-range and the mean cluster sizes studied in this work (mean hydrodynamic radius greater than 1 μm), the relaxation time associated to the rotational diffusion is at least two orders of magnitude greater than the relaxation time associated to the translational diffusion [29], then we assume that these two diffusions are temporally separated. On the other hand, the restructuring movement due to cluster compactification should be considered, at least *a priori*, if the bound between two particles of an aggregate is weak enough. Although this effect has a great influence on the value of the fractal dimension (as we will comment later), we will assume (as other authors do [30]) that restructuring happens during a time of the order of the aggregation process, being conditioned by the cluster size. Therefore, the translational diffusion of an *n*-particle cluster will be temporally separated from the dynamics of the rest of the system. Thus, the time scale corresponding to our aggregation kinetics study will be associated to the temporal evolution of the translational diffusion coefficient of the clusters with a typical length scale associated to their mean hydrodynamic radius.

In order to obtain the experimental average of the translational diffusion coefficient $\bar{D}_{\exp}(q;t)$ over the system at any time, the *normalized electric field autocorrelation function* $g_E(\tau) = \dfrac{\left\langle E(q,0)E^*(q,\tau)\right\rangle}{\left\langle |E(q)|^2 \right\rangle}$ is treated as an expansion in powers of τ [31]:

$$\ln(g_E(\tau)) = -\kappa_1\tau + \frac{1}{2}\kappa_2\tau^2 + \ldots, \qquad (11)$$

where κ_i is the i-order cumulant. Thus, κ_1 gives the average decay rate whereas κ_2 contains the standard deviation. In this context:

$$\bar{D}_{\exp}(q;t) = \kappa_1 / q^2 \qquad (12)$$

From a theoretical viewpoint, an estimation of the mean translational diffusion coefficient $\bar{D}(q;t)$ can be performed at any time by means of an average of the diffusion coefficients D_n of the n-particle clusters:

$$\bar{D}(q;t) = \frac{\sum_{n=1}^{Nc} b_n(q;t) D_n}{\sum_{n=1}^{Nc} b_n(q;t)}, \qquad (13)$$

where $b_n(q;t) = N_n(t)\, n^2 S(qR)$ contains the frequency and the structure of the n-particle clusters [32], $N_n(t)$ is the frequency of the n-clusters at time t and $S(qR)$ their corresponding structure factor, R being again the radius of gyration of a n-particle cluster. At long times, i.e. when the aggregates reach a non-evolving fractal morphology, an estimation of D_n can be done by assuming that the cluster compactness is given by the final mass fractal dimension d_m:

$$\frac{D_n}{D_0} = (n)^{-1/d_m} \propto R^{-1} \ , \qquad (14)$$

where D_0 is the diffusion coefficient of the free individual particles.

The assumption of a functional form for $S(qR)$ within all accessible values of qR involves a problem with an unknown analytical solution that has only been estimated by means of computer simulations [32]. However, this difficulty can be overcome if our estimation of $\bar{D}(q;t)$ is performed for $qR >> 1$. In that case, the fractal structure is resolved and $S(qR) \propto (qR)^{-d} \propto n^{-1}q^{-d}$. Therefore, only an *a priori* knowledge of $N_n(t)$ is needed in order to obtain the theoretical mean translational diffusion coefficient given by (13) and (14).

The frequency $N_n(t)$ can be predicted if the aggregating suspension is diluted enough (monomer volume fraction usually below 1%). In this respect, the aggregation process can be considered as a set of binary reactions $A_i + A_j \rightarrow A_{i+j}$ (A_i denotes an aggregate formed by i monomers) neglecting the simultaneous reactions involving 3 or more clusters [33]. A widely used mean-field aggregation model based on the binary reaction assumption is Smoluchowski´s Rate Equation [34, 35]. Its expression for reactions in which fragmentation does not take place is:

$$\frac{dN_n(t)}{dt} = \frac{1}{2}\sum_{i+j=n} k_{ij} N_i(t) N_j(t) - N_n(t)\sum_{i=1}^{\infty} k_{in} N_i(t) \qquad (15)$$

The set of rates k_{ij} ($i, j = 1,...,\infty$), usually known as *kernel*, contains the whole kinetic information through its mass (number of monomers) and geometry cluster dependences. From a known k_{ij} and an initial condition, e.g. $\vec{N}(0) = (N_1(0) = 1, N_2(0) = 0,...,0)$, expression (15) gives a continuous and deterministic set of frequencies $\vec{N}(t)$ at any time.

Due to the difficulty of assuming a functional form for the reaction kernel, it is useful to consider its asymptotic behaviour under the homogeneous scheme of van Dongen and Ernst [36]. In this context, small-large and large-large cluster interactions are governed by two exponents ν and λ: $k_{1j} \propto j^{\nu}$ and $k_{jj} \propto j^{\lambda}$ (large j). This scaling theory applied to nongelling-kernels $(\lambda \leq 1)$ also provides the asymptotic behavior of $\bar{D}(q;t)$:

$$\bar{D}(q;t) \propto t^{-z} \; ; (z = 1/(1-\lambda)\, d_m) \qquad (16)$$

In fact, expression (16) is a key to associate a type of kernel to the results obtained from the experimental kinetics of an aggregation process.

Pure diffusion aggregation processes have also a special interest under this formalism: On one hand, these processes are dominated by small-large cluster interactions whereas interactions between identical sized clusters do not show any dependence on j for large j ($k_{jj} \propto j^{\lambda=0} \approx$ constant) due to the compensation between the increasing collision cross-section and the decreasing diffusivity of the clusters when j grows [37].

D. Interactions between liposomes

From a physicist's viewpoint, charged liposomes can be considered as colloidal particles whose interactions can be treated with the help of a well-known mean-field approach: The DLVO theory. Accordingly, the lipid vesicles would interact through Coulomb repulsive forces (characterized by an interaction energy E_{elec}) and short-range van der Waals attractive forces (whose interaction energy will be denoted by E_{vW}). Usually, E_{elec} is modelled as a Yukawa decaying function that contains as input parameters the Debye-length and the surface potential (or charge). For E_{vW}, Hamaker´s constants of water, hydrocarbon and polar phase, together with the thickness of the surface phospholipids layer, have been used as input parameters.

Apart from classical DLVO theory, when colloidal particles have a surface with certain degree of hydrophobicity, different experimental techniques and theoretical approximations [13-15] have pointed out the existence of a hydration energy, E_{hyd}, which is generally repulsive. In the 70´s, the origin of this hydration or structural force was mainly attributed to the strongly bound and oriented layers of water molecules on the surfaces [13]. However, there are other possible explanations such as the local variation of the dielectric permittivity in the electric double layer [14] or an entropic repulsion arising from the confinement of thermally mobile surface groups [15]. Thus, a conclusive comprehension of E_{hyd} is still lack and to find an analytical expression for E_{hyd} is not a straightforward task. For that reason, experiments and computer simulations based on statistical mechanics incorporating even quantum effects should be used in the next years. In absence of them, some authors use semi empirical exponential expressions for E_{hyd} that also introduce fitting parameters [38, 39] in order to explain experimental results. In particular, Okhi and Arnold define a hydrophobic index that represents the degree of hydrophobicity of the membrane surface [39]. They propose to model the hydration energy from a purely repulsive interaction (the surface is hydrophilic and tends to be completely hydrated) to an attractive interaction (the surface is hydrophobic and then it is largely dehydrated). In this model, the surface tension of the present interfaces also appears as input parameter, together with the hydrophobic index.

In our work, the importance of E_{hyd} in the aggregation processes mediated by divalent cations will be experimentally analyzed via FTIR spectroscopy. Thus, we will conclusively show that the dehydration of the superficial lipid headgroups exerted by some metallic cations must be considered. Due to the large number of parameters involved in the total interaction energy, $E = E_{elec} + E_{vW} + E_{hyd}$, a qualitative (rather than quantitative) analysis will be preferred in order to explain our experimental results.

III. MATERIALS AND METHODS

A. Synthesis and characterization of liposomes

Phosphatidilserine (PS) from bovine spinal cord was obtained from Lipid Products (Nutfield, UK). Phospholipid at the proportions indicated below were dissolved in a mixture (2:1, volume ratio) of chloroform and methanol in a round-bottom flask and dried in a rotary evaporator under reduced pressure at 40 ^{0}C to form a thin film on the flask. The film was hydrated with desionized water (MilliQ, Millipore, USA) to give a lipid concentration of 30mM. Multilamellar liposomes (MLV) were formed by constant vortexing for 4 min on a vortex mixer and sonication in a Transonic Digitals bath sonifier (Elma, Germany) for 10 min. MLV were downsized in an Extruder device (Lipex Biomembranes, Canada) through polycarbonate membrane filters of variable pore size under nitrogen pressures of up to $55\text{x}10^5$ N.m^{-2} . Liposomes were extruded in three steps: first, three consecutive extrusions through a 0.8 μm pore diameter filter and three consecutive extrusions through two stacked 0.4 μm membranes. The resulting lipid suspension was then extruded fifteen consecutive times through two stacked 0.2 μm filter. After preparation, a nitrogen stream was passed to displace the air, and, finally, liposomes were stored at 4-7 ^{0}C in a refrigerator in quiescent conditions until their use.

To characterize a liposome suspension as a colloidal dispersion, two different requirements are necessary: The characterization of particles in size and shape and the determination of the initial liposome concentration, which is a troublesome problem when vesicles are used as primary particles. In order to determine the liposome size, DLS and SLS experiments were performed for different dilute liposome volume fractions and angles. In the case of DLS, the size was obtained from the mean particle diffusion coefficient, $\bar{D}_{\exp}(q;t)$, which was in turn determined using the cumulant analysis (expression (12)), by averaging six individual measures at different scattering angles. By means of SLS, the particle size was determined fitting the particle form factor of a three modal distribution of hollow spheres, since liposomes were assumed to be unilamellar vesicles within certain degree of polydispersity (see Ref. [9] for a more

detailed explanation). The best agreement was reached for a mean radius $a = 75$ nm and 0.2 of polydispersity (standard deviation of the particle radius divided by the mean). This size and a thickness of 4.5 nm, contrasted by means of small angle X-ray scattering, typify our liposomes as *large unilamellar vesicles*.

To measure the initial liposomes concentration, the procedure proposed by Haro-Perez et al. [40] has been followed. This method compares the volume fraction obtained assuming that the whole PS mass is forming vesicles with that obtained considering a homogeneous distribution of repulsively structured vesicles. The obtained values differ about 3.5 %.

B. Aggregation experiments

Aggregation was induced by adding electrolyte to the initially stable aqueous suspensions of liposomes at 25ºC. The water used for sample preparation was purified by inverse osmosis using a Millipore equipment. The different electrolyte-particle mixtures were prepared by mixing equal amounts of buffered electrolyte solution and particle suspension through a Y-shaped mixing device in a cylindrical quartz glass cuvette. The magnesium concentration was varied from 5 mM to 150 mM of $MgCl_2$. In all cases, the final liposome volume fraction was 0.1%. The experimental threshold salt concentration to induce aggregation was $[Mg\,Cl_2] = 4\,\mathrm{mM}$. No change on time of the first cumulant of the field autocorrelation function was observed for smaller salt concentrations, which confirms the existence of such threshold.

C. Experimental measurement of the Structure factor and the Diffusion Coefficient

On the basis of the 3D-DLS scheme discussed in section II.B, our light scattering experiments were performed with the help of a 3D-DLS spectrometer equipped with a rotatory arm, supplied by LS instruments (Fribourg, Switzerland). Formally, in this design the scattering volume is defined by the intersection between the collecting optics and the cross of two incident incoherent He-Ne laser beams (wavelength *in vacuo* $\lambda = 632.8$ nm) coming from above and below the average scattering plane. A

digital correlator computes the *normalized cross-correlation function* $g_{12}^{system}(q,\tau) = \frac{< I_1^{system}(q,t) I_2^{system}(q,t+\tau) >}{< I_1^{system}(q) >< I_2^{system}(q) >}$ of the intensities registered by the two detectors for a given system. These scattered intensities are photomultiplied by two avalanche photodiodes coupled to the arm. The cross-correlation function $g_{12}^{system}(q,\tau)$ is also recorded by the same computer that controls the spectrometer.

In order to obtain $S(q)$, and according to Section II.B, the function $\beta^a(q)/\beta^0(q)$, that corrects the magnitude of the structure factor due to the disturbance of multiple scattering, has to be evaluated (see expression (10)). Expression (9) is not applicable since we do not have a direct access to the single scattered intensities. In this respect, as it was mentioned above, our cross correlation scheme provides an experimental determination of $g_{12}^{system}(q,\tau)$.

The cross-correlation function is related to the normalized single scattering dynamic structure factor $g_E(\tau)$ [28] by:

$$g_{12}^{system}(q,\tau) = 1 + C\beta^{system}(q)\left[g_E(\tau)\right]^2 \quad , \qquad (17)$$

where $C \le 1$ is constant that accounts for the different scattering volumes seen by the two detectors and the ratio of the size of the detector apertures to the size of the coherent areas of the scattered light. Expression (17) can be used to determine $\beta^{system}(q)$ taking advantage of the zero-limit $\lim_{\tau\to 0} g_E(\tau) = 1$ [28] and then $g_{12}^{system}(q,\tau=0) = 1 + C\beta^{system}(q)$. Thus, if the measurements on the aggregated and non-aggregated systems are performed under identical experimental conditions C will remain invariant and:

$$\left[\frac{\beta^a(q)}{\beta^0(q)}\right]^2 = \frac{g_{12}^a(q\ ,\tau=0)-1}{g_{12}^0(q\ ,\tau=0)-1} \qquad (18)$$

By means of expression (18) we make a quantitative measurement of $\beta^a(q)/\beta^0(q)$.

At the same time, we consider as constant factors, within the explored *q*-range, the transmissions ratios between the aggregated and non-aggregated samples (expression (10)). So, their influence on the scattering exponents as a multiplicative constant can be discarded (expression (5)). Therefore, we adopt the experimental determination of an "effective" structure factor $S^*(q)$:

$$S^*(q) = \sqrt{\frac{< I_1^a(q,t) >< I_2^a(q,t) >}{< I_1^0(q,t) >< I_2^0(q,t) >}} \frac{\beta^a(q)}{\beta^0(q)} \qquad (19)$$

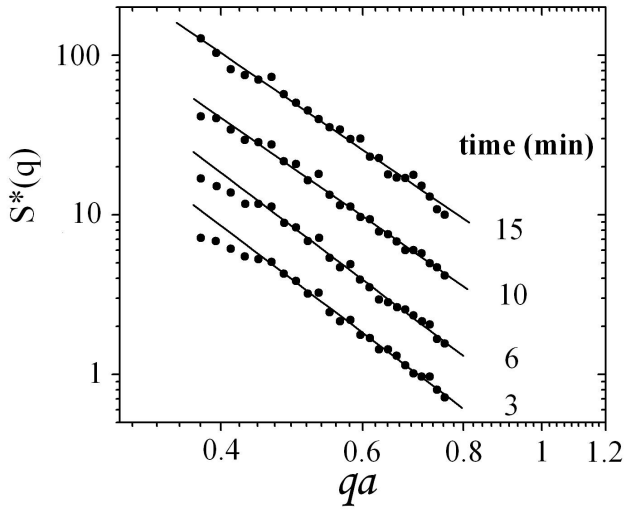

FIG. 1 Experimental $S^*(q)$ according to expression (19) at 5mM of magnesium. The diverse measurements correspond to different times (stadiums) at which the aggregation process was stopped. Differences in the slope of $S^*(q)$ are negligible after 10 min from the beginning of the aggregation process. From that moment, $S^*(q)$ presents a power-law behaviour over the entire q-range with a non-evolving slope of -3.46 (see also figure 5 and table I). At previous times, $S^*(q)$ presents an evolving behaviour, thus the lines corresponding to 3 and 6 min are guides to the eye.

With the aim to obtain a reliable determination of $S^*(q)$ for each electrolyte concentration, the aggregation processes were stopped at different stadiums until a constant value for the fitting scattering exponent was reached (expression (5)). The stops were carried out by diluting the evolving system below the threshold aggregating

salt concentration. At their final states, the apparent mean hydrodynamic radius of the aggregates exceeded 1.5 μm for all the samples. Figure 1 shows an example of the time evolution of $S^*(q)$.

Certainly, the q-range employed to determine the scattering exponents appears as a crucial point. In this respect, sufficient, but not necessary, conditions have been proposed by different authors in order to obtain reliable values for the scattering exponents, see for instance Ref. [41]. Here, in addition to the constraint introduced by the primary particle radius a ($q < a^{-1}$), we have an experimental difficulty due to the rapid increment of the scattered intensity for small q values, which is caused by the large scattering exponents. In this situation, the saturation limit of the detectors is promptly achieved when q decreases and the proportionality between the scattered intensity and the photomultiplied signal becomes broken. This difficulty seems to be present in other SLS measurements involving large scattering exponents, see for instance Ref. [42] where the authors found a characteristic scattering exponent of -3.38 using a similar q-range as we do.

In order to overcome this problem, we performed our measurements under the saturation limit of the detectors, i.e. in the linear range. Thus, we extended our q-range to large q-values for which the saturation limit is not achieved. At the same time, we tested the reliability of the employed q-range by reproducing satisfactorily the universal DLCA fractal dimension ($d_m = 1.75$) obtained in our previous study at 5 mM of calcium [9]. This diffusive regime at 5 mM of calcium had been also proved from aggregation kinetics data obtained via independent DLS measurements (see again [9]). At the same time, we confirmed for the explored q-range that a reliable and reproducible statistical estimator to determine our structure factors resulted from the average of 5 independent measurements per q-value and 1min per measurement.

With respect to the system aggregation kinetics, the experimental average value for the translational diffusion coefficient $\overline{D}_{\exp}(q;t)$ at any time was evaluated from expressions

(11) and (12). In this case, the scattered field autocorrelation function $g_E(\tau)$ was obtained from the intensity autocorrelation function via Siegert relation, and was recorded with our computer in intervals of 25s during the aggregation processes. The measures were performed at a fixed angle of 90º.

D. Cryo-TEM measurements

With the aim of complementing our structural study based on light scattering experiments, we took Cryo-TEM images from an aggregated sample containing a small concentration of magnesium which is similar to that used in some of our light scattering experiments. At the same time, Cryo-TEM measurements were performed for a non-aggregated sample, i.e. in absence of salt. For the case of the sample containing magnesium, the appropriate volume of a concentrated salt solution was added to the liposome suspension and vortexed. After 5 minutes, a drop of the mixture was deposited on a perforated grid (Quantifoil, Germany), previously ionized by glow discharge in air, and, after removing part of the drop with a filter paper strip, it was immediately frozen dipping it in ethane at -182ºC using a Cryo Work Station EM CPC (Leica Microsystems GmbH, Germany). This lag time allows us to obtain liposome aggregates whose size is bigger that 1 μm. This size was previously verified by means of DLS. For the case of non-containing salt samples, a drop of the initial liposome suspension was employed, and the same treatment was done. The obtained grids containing the samples were maintained frozen with liquid nitrogen in a cryo holder and loaded into a transmission electron microscope Jeol JEM-1400 (Jeol Ltd, Tokyo, Japan) working at 120 kV.

E. FTIR measurements

The FTIR spectra of liposomes prepared in D_2O containing the appropriate amounts of the desired cations were acquired with a Mattson Polaris spectrometer. The intensity of the infrared absorption was quantified by means of a cooled liquid nitrogen mercury-cadmium-telluride detector. Each spectrum was a mean of 1,000 individual scans performed at 25 ºC, at a resolution of 2 cm^{-1} and using two CaF_2 windows with a 50 μm spacer containing the sample. The final spectra were obtained subtracting the spectra of

the corresponding solvent acquired in the same conditions. It is known that chemical groups of the phospholipid molecule, as phosphate or carboxylate, can interact with cations resulting in a change in their vibrational state [43] but the stretching band of the carbonyl ester, located at 1,720 cm^{-1}, have been proved to be very sensitive to environmental factors as, for example, the hydration grade of the molecule [44], the phase state of the bilayers, or the temperature. For these reasons, we focused our attention on the stretching band of the carbonyl ester. This stretching band presents a fine structure composed by minor bands corresponding to the hydrated and non-hydrated carbonyl ester groups. We analyzed the contribution of the non-hydrated carbonyl band, which is located at 1744 cm^{-1}, to the multicomponent band quantifying its relative area after Fourier deconvolution. The fit of the component bands was done using the Grams 3.2 program (Galactic Inc.).

IV. RESULTS AND DISCUSSION

A. Effect of MIS and Polydispersity

To understand the cluster morphologies, a precise and undoubted determination of the α-exponent must be achieved. To do that, the effects of the aggregate polydispersity and MIS on the measured scattering exponents must be evaluated.

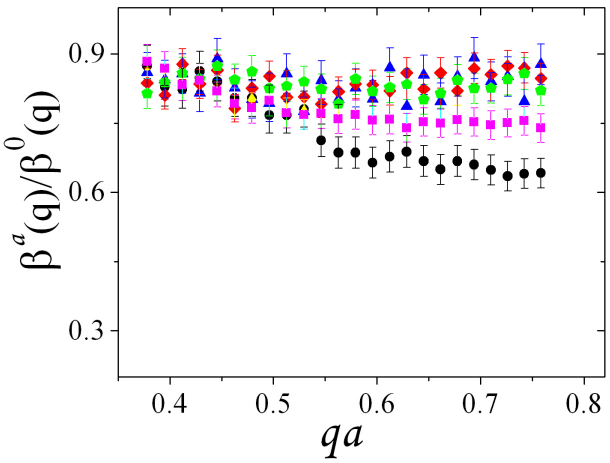

FIG. 2 Experimental ratio $\beta^a(q)/\beta^0(q)$ from Expression (18). [$MgCl_2$]: 5 mM (black circles), 7.5 mM (magenta squares), 10 mM (blue triangles), 30 mM (red diamonds) and 100 mM (green pentagons). This figure has been shown in Ref. [10].

In relation to the MIS, the *normalized cross-correlation functions* $g_{12}^{system}(q,\tau)$ were measured and the ratio $\beta^a(q)/\beta^0(q)$ was calculated using expression (18) for all the examined electrolyte-liposomes samples. In Figure 2, the q-dependence of $\beta^a(q)/\beta^0(q)$ is plotted for several samples. A remarkable q-dependence of $\beta^a(q)/\beta^0(q)$ was observed for 5 mM (and a slight dependence for 7.5 mM). The rest of the samples exhibited a constant $\beta^a(q)/\beta^0(q)$ quotient over the explored q-range. In these cases, therefore, the MIS has a constant contribution, which means that the values of the scattering exponents are not significantly affected by MIS. On the contrary, the 5 mM sample is very influenced by MIS. This is illustrated in Figure 3, in which the effective structure factors determined with and without the MIS correction are plotted for such sample. As can be seen, if this correction is not performed we would obtain $\alpha^{spurious}(5\text{ mM}) = 3.12$ instead of 3.46 (the true value). This wrong result was also confirmed within the experimental uncertainty by a conventional light scattering device with a single He-Ne laser beam (Malvern 4700IIC). Consequently, the use of a cross-correlation scheme based on a three-dimensional light scattering design provides, under our experimental conditions, the necessary accuracy to discern the differences between dense clusters.

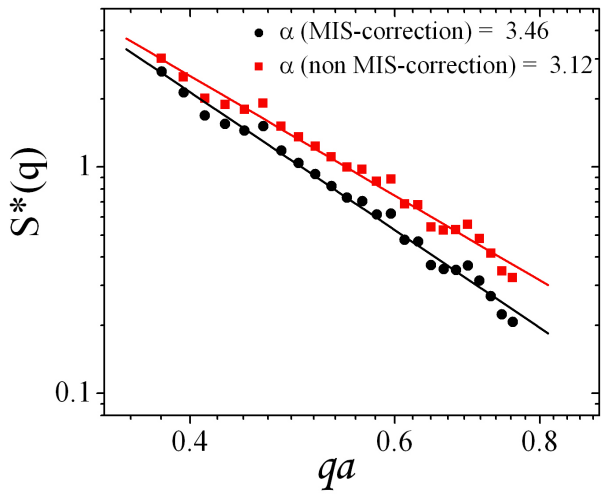

FIG. 3 Experimental $S^*(q)$ at 5mM of magnesium. Black circles correspond to expression (19) whereas red squares do not consider the MIS correction accounted for by $\beta^a(q)/\beta^0(q)$. Black and red solid lines stand for the corresponding linear fits.

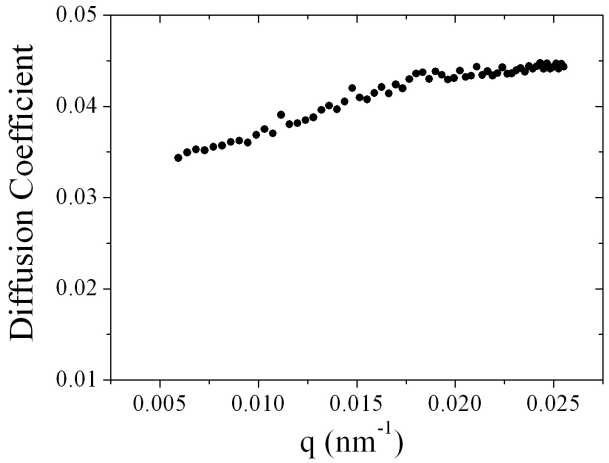

FIG. 4 Normalized mean translational diffusion coefficient $\bar{D}_{\exp}(q;t)/D_0$ corresponding to the 100 mM magnesium concentration. A weak q-dependence is revealed by a relative increment of $\left|\bar{D}_{\exp}(q_{\max};t)-\bar{D}_{\exp}(q_{\min};t)\right|/\bar{D}_{\exp}(q_{\min};t)\approx 0.3$. D_0 is the free diffusion coefficient of the individual monomers.

On the other hand, the polydispersity reached in an aggregation process can introduce a drastic disturbance on the scattering exponents determined by means of SLS when the cluster size distribution is broad. In these situations, a direct interpretation of the scattering exponents as fractal dimensions can cause misunderstandings. According to the work by Martin et al. [37], we have examined the experimental q-dependence of the first cumulant of the field autocorrelation function divided by q^2, κ_1/q^2, for all the stopped suspensions (expressions (11) and (12)). As it was previously discussed, this ratio can be interpreted as an apparent mean translational diffusion coefficient $\bar{D}_{\exp}(q;t)\equiv\kappa_1/q^2$ of the cluster distribution. It should be clear that in this context, we explore the q-dependence of κ_1/q^2 for non evolving suspensions at a time in which the aggregates of these suspensions have achieved their final fractal structure and the aggregation processes have been stopped (see section III.C). In this framework, $\bar{D}_{\exp}(q;t)$ will present a clear dependence on q, for $qR>1$, in case of a wide cluster polydispersity (here R stands for the apparent mean hydrodynamic cluster radius). In our experiments, the evaluation of $\bar{D}_{\exp}(q;t)$ over the q-range $[6\cdot10^{-3},2.6\cdot10^{-2}]$nm^{-1}

showed a weak q-dependence for all the examined samples. The maximum increment detected for $\bar{D}_{\exp}(q;t)$ was approximately of 30% corresponding to the 100 mM sample (see figure 4). This result is consistent with those obtained for aggregation kinetics, as we will argue later, being both the evidence of a narrow cluster distribution, and consequently of a weak regime of polydispersity.

B. Discussion of the Structure Factors and Cryo-TEM images

According to the previous protocol, the experimental $S^*(q)$ were determined for all the electrolyte concentrations and an unquestionable power law dependence was obtained at each case (see Figure 5), from which the scattering exponents α were extracted. Table I also summarizes the results for the considered electrolyte-liposome samples. The absolute error associated to each exponent was estimated from the statistical reproducibility of the scattering data by their optimum power law fit. From this analysis, a clear trend is revealed: α decreases with increasing the magnesium concentration reaching a permanent value in the vicinity of 30 mM. The α values in the range 2.6-2.9 are a sign of dense morphologies that can be clearly identified as mass fractal with $d_m = \alpha$ ((expression (5)). On the other hand, after a careful analysis of the experimental data (which includes the MIS and polydispersity effects), structure factors with $\alpha > 3$ reveal the existence of surface fractals (see again expression (5)). Consequently, within the range $5\text{mM} \le [\text{MgCl}_2] \le 15$ mM, the resulting morphologies, included into the domain of surface fractals, will present a surface fractal dimension $d_s = 6 - \alpha$.

The surface fractals domain has Porod´s law, $d_s = 2$, as the lowest limit for a smooth surface [21], whereas $d_s \to 3$ corresponds to the highest limit for a completely rough surface. Our surface fractal dimensions are contained within $d_s(5\text{ mM}) = 2.54 \pm 0.08$ and $d_s(15\text{ mM}) = 2.96 \pm 0.05$.

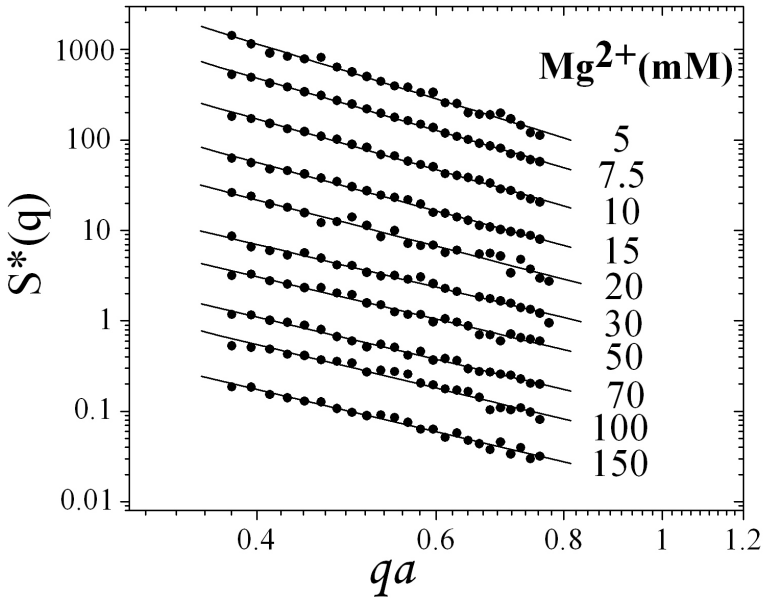

FIG. 5 Effective Structure Factors $S^*(q)$ for the different magnesium concentrations. The experimental values (circles) result from Expression (19) whereas solid lines represent the theoretical fit according to Expression (5). The content of this figure has been shown in Ref. [10].

Certainly, the above interpretation of the experimental $S^*(q)$, obtained from expression (19), is based on the conservation of the form factor, $P(q)$, of the primary particles inside the aggregates (see the cancellation between expressions (6) and (7) to give expression (8)). In this respect, it is essential to prove that we extract the real structural information from the scattered intensity when we deal with aggregates formed by primary particles that are deformable and potentially fusionable. Thus, it is frequent to find in literature dramatic distortions due to the deformation of the vesicles when they stick together [45, 46]. In these situations, the vesicles lose their original shape, and $P(q)$ included in expression (6) would not be anymore their form factor after aggregation. Then, the implicit cancellation assumed in expression (8) is not admissible and the resulting q-dependence is not only due to $S(q)$. However, this misinterpretation of $S(q)$ due to the deformation of the primary particles will be manifested only at large q-values ($q \geq a^{-1}$). This is the range for which the details of the shape of the vesicles can be clearly distinguished via SLS. In this respect, our measurements of $S^*(q)$ were

performed for $qa < 0.8$. Therefore, only for large values of this q-region, the plausible disturbance introduced by the deformation of the particles would have some effect on the determination of $S^*(q)$ via expression (19). Thus, one would expect bad correlated results, presumably far from a power law behaviour, only at large q if the vesicles change their shape when they aggregate. However, in our case, the same experimental power law behavior is manifested within the whole q-range (see figure 5) and, therefore, a non significant deformation of the vesicles inside the aggregates can be presumed. This experimental fact can be use as argument not only to discard an important deformation but other severe distortions as vesicle fusion, for which the primary particles would not retain their individuality.

From a theoretical viewpoint, the small deformation of our vesicles assumed from the experimental behavior of $S^*(q)$ at large q, can be accounted for by the approach proposed by Petsev [47]. In his paper, the author presents a general model for vesicle adhesion based on the coupling between van der Waals attraction and bending elasticity forces. Using standard values for Hamaker's constants, this author shows calculations that are relevant for vesicles in which the ratio between the bilayer thickness and the vesicle radius is around 0.01. Together with this ratio, a significant deformation is expected only when the ratio between the separation distance of two adhered vesicles and the vesicles radius is smaller than 0.02. In our case the first ratio results much greater, 0.06. Although no experimental data is available for the separation distance between two adhered PS vesicles in the presence of Magnesium, works as that cited in Ref. [39] by Ohki and Arnold, suggest a ratio between the separation distance and the particle radius of about 0.02-0.03. Accordingly, in the light of this model, a small deformation, consistent with our experimental data, is expected for our vesicles.

TABLE I. Experimental Scattering Exponents α with their corresponding fractal dimensions at different magnesium concentrations.

$[Mg^{2+}]$ (mM)	α	d
5	3.46 ± 0.08	$d_s = 2.54 \pm 0.08$ $(d_m = 3)$
7.5	3.28 ± 0.05	$d_s = 2.72 \pm 0.05$ $(d_m = 3)$
10	3.18 ± 0.05	$d_s = 2.82 \pm 0.05$ $(d_m = 3)$
15	3.04 ± 0.05	$d_s = 2.96 \pm 0.05$ $(d_m = 3)$
20	2.91 ± 0.12	$d_m = 2.91 \pm 0.12$
30	2.68 ± 0.07	$d_m = 2.68 \pm 0.07$
50	2.67 ± 0.08	$d_m = 2.67 \pm 0.08$
70	2.66 ± 0.06	$d_m = 2.66 \pm 0.06$
100	2.65 ± 0.07	$d_m = 2.65 \pm 0.07$
150	2.67 ± 0.08	$d_m = 2.67 \pm 0.08$

In addition to the experimental $S^*(q)$, we took Cryo-TEM images of different samples. Figures 6.b and 6.c show the micrographs corresponding to two aggregates at 7mM of $MgCl_2$. Uniform clusters can be observed in both cases. Thus, this high compactness would support and illustrate the interpretation that the high values obtained for the α exponent in these cases (5 and 7.5 mM) are associated to a surface fractal structure.

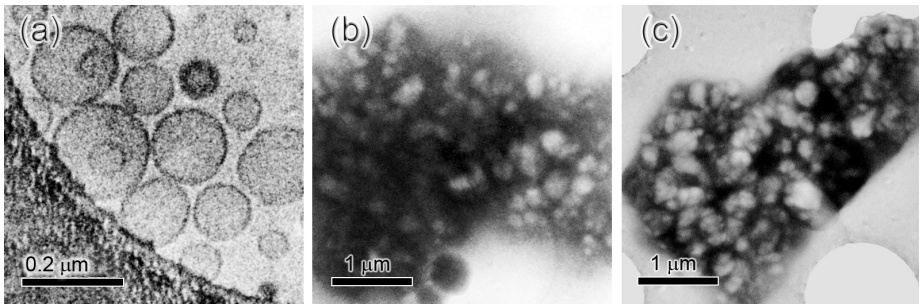

FIG. 6 Cryo-TEM images of PS liposomes in water (a) and after 5 minutes in water containing 7 mM of $MgCl_2$ (b and c). Dark areas indicate the presence of crystalline ice (amorphous ice appears as transparent area in images).

Accordingly, we can state that a transition from surface fractals to mass fractals has been found in the range from 5 to 150 mM of magnesium. The reader should however note that this interpretation cannot be done if the experimental data are not MIS-corrected, particularly at low salt concentrations (<10 mM). As it was discussed previously, in the case of uniform clusters the MIS effect is stronger at high q-values, i.e. small spatial scales, as the experimental function $\beta^a(q)/\beta^0(q)$ reveals (figure 2). At these scales, the light experience more reflections in uniform clusters than in those which are less compact and then the MIS has an effect on the measured fractal dimensions.

Certainly, very few structures of biological interest have been described by the surface fractal notion [42]. On the other hand, similar morphological evolutions have been rarely documented in colloidal physics from small angle scattering techniques. For instance, the pioneering results obtained by Keefer and Schaefer [8] in a system of rough particles made from silica condensation show a clear analogy with our measured fractal dimensions, even though they studied a significantly different system. In that work, the authors pointed out the application of the Eden model [41] to account for a theoretical description of the observed fractal structures. In any case, we should remark that our observed dilation symmetries need a deeper investigation to be theoretically justified.

C. Qualitative interpretation of morphologies using hydration energies.

We have concluded from the previous data that, when the Mg^{2+} concentration increases from 5 to 150 mM, the corresponding clusters experience a transition from uniform ($d_m = 3$) to also dense structures, $d_m = 2.6 - 2.7$. In the framework of a classical DLVO qualitative analysis, this high compactification would be explained by means of an aggregation in a secondary shallow minimum of the total interaction energy, $E = E_{elec} + E_{vdW}$, whose depth is electrolyte dependent since that the increase of divalent salt leads to a progressive screening of the surface charge. However, some difficulties arise when a comparison with the aggregation induced by calcium is done [9]. Aggregation induced by $CaCl_2$ showed a slow regime (Reaction Limited Cluster

Aggregation) from 2.5 to 5 mM calcium concentration whereas and a DLCA regime from 5mM to 7mM was documented. In both cases, *ramified* structures were observed ranging from $d_m = 1.91$ to $d_m = 1.75$. In this situation, the energy of the bond between two liposomes after sticking (accounted for van der Waals attraction) prevents reversibility and cluster compactification. Thus, as an example, whereas 5mM of magnesium leads to a *dense* morphology, $d_m = 3$, an identical calcium concentration induces branched structures, $d_m = 1.75$. This experimental behavior suggests that the bound between two vesicles would be appreciably stronger in the case of calcium. In any case, the DLVO picture, $E = E_{elec} + E_{vdW}$, cannot explain why the behaviors in the presence of calcium and magnesium at identical concentrations are so different if both are divalent cations. Hence, we turn our attention to the possible specific effect of the hydration energy in the presence of these two cations via the determination of the hydration grade of the liposome surfaces. The Fourier-Transform Infrared Spectroscopy (FTIR) analysis provides us this possibility.

As a result of this analysis, figure 7 shows the component bands of the fine structure of the spectra of PS liposomes in the carbonyl stretching zone (red) in D_2O at 0, 2.5, 5 and 7 mM of $CaCl_2$. In D_2O, the stretching CO band is composed by three bands located at 1,744 cm^{-1} (green), 1,727 cm^{-1} (yellow) and 1,708 cm^{-1} (blue). These bands are a consequence of the different hydration grade of the CO groups of both hydrocarbon chains. Thus, each one of component bands is exclusively the result of the hydration state of the two CO groups of the phospholipid and, if no isotopic labeling of the carbonyl group is performed, no differences between them can be observed [43]. As a result, the previously commented component bands observed in D_2O are originated by dehydrated carbonyl (1,744 cm^{-1}), monohydrated carbonyl (1,727 cm^{-1}) and dihydrated carbonyl (1,708 cm^{-1}). As can be observed, there is a progressive increment of the relative area of the 1744 cm^{-1} band (green) -corresponding to dehydrated CO- upon Ca^{2+} concentration. At the same time, at $CaCl_2$ concentrations of 2.5, 5 and 7 mM the experimental stretching band is composed by 5 component bands. These two supplementary bands are located in the low wave number zone of the experimental carbonyl band. This fact indicates that, in presence of the salt, the CO groups undergo a new type of interactions not present in pure D_2O. At high Ca^{2+} concentrations these

changes have been explained by different rotational chain isomers in the lipid-Ca^{2+} complex and a new strong hydrogen bond established between CO and water [45]. Our results show that the effect of $CaCl_2$ on CO groups, as observed by the FTIR spectra, is concentration-dependent and can be quantified.

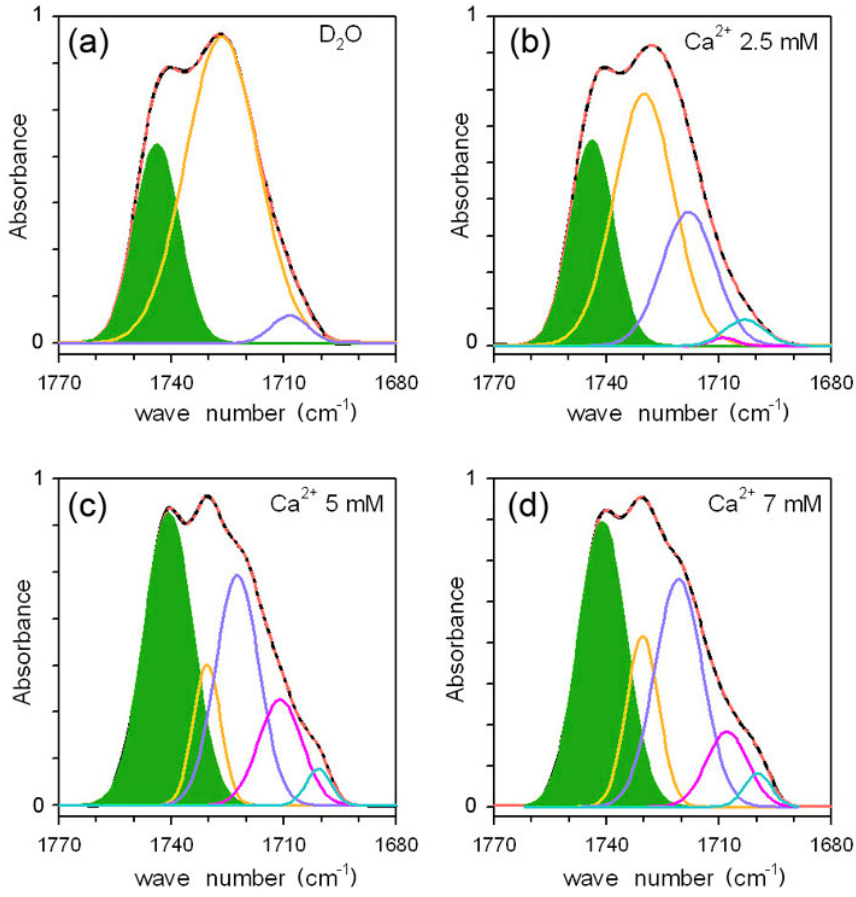

FIG.7 FTIR spectra of the carbonyl band of PS liposomes: (a) in pure D_2O, (b) $[Ca\,Cl_2] = 2.5$ mM, (c) $[Ca\,Cl_2] = 5$ mM, and (d) $[Ca\,Cl_2] = 7$ mM. Black line: experimental deconvolved spectrum. Dashed light red line: synthetic spectrum obtained from the component bands (it is overlapped with the experimental band). Filled dark green peak: component band corresponding to the dehydrated carbonyl group. Other lines: component peaks corresponding to carbonyl groups with different hydration grades.

The relative areas of the deconvolved component bands showed that, when $CaCl_2$ was added to the aqueous medium, there was an increase of the area of the non-hydrated carbonyl band, which had no significant shift of its maximum at any salt concentration

assayed. Thus, the microenvironment of the dehydrated CO is not affected by the presence of the divalent cation. At 2.5 mM of $CaCl_2$ this band had an area 16% larger than that in pure water, reaching a plateau at 5 mM, with a mean relative increment of 62%. Consequently, no further change occurs between 5 and 7 mM of $CaCl_2$ (filled green peak, figure 7). On the other hand, equivalent essays were performed in the presence of $MgCl_2$ over the range 0-20 mM. In that case, the studied carbonyl peak showed no significant change of the percentage area of its dehydrated carbonyl band in the studied range. Nevertheless, other functional groups of the phospholipid molecule, as phosphate or carboxylate, should be explored in a further investigation in order to account for the evolution of the fractal dimension in the presence of this cation.

Consequently, we propose a qualitative analysis on the basis of the area of the non-hydrated carbonyl band. With calcium concentration, the increase in this area suggests a progressive dehydration of the liposome surfaces. Water molecules would be removed from the surface and the hydration repulsive interaction would become smaller. Consequently, the barrier due to this hydration energy would decrease and, if the Coulomb repulsion is strongly screened, the resulting total energy could therefore show a deep minimum essentially accounted for van der Waals attraction. For the sake of clarity we present in Figure 8 a sketch with this qualitative interpretation. On the other hand, with magnesium, the dehydration of the lipid membrane associated to the carbonyl group would not take place and the hydration repulsive barrier would persist. Now the total interaction energy, when Coulomb repulsion is screened, $E \approx E_{vW} + E_{hyd}$, would present a "shallow" minimum with different depth depending on the magnesium concentration, see sketch of figure 9. Hence, this non-suppressed hydration would condition the depth of the energy minimum as well as the separation distance for two bound vesicles. This lower energy minimum would enhance the cluster compactification.

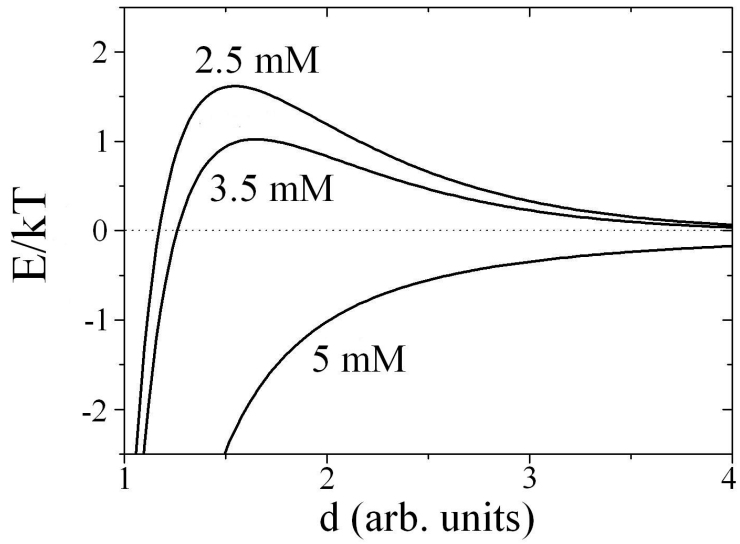

FIG. 8 Qualitative description of the interaction energy E at short distances between two liposomes in the presence of different calcium concentrations. With increasing the calcium concentration the barrier resulting from the addition of hydration and Coulomb repulsive interactions decreases. At 5 mM, for which a DLCA regime was achieved [9], only a deep minimum due to van der Waals attraction remains. The distance d (arbitrary units) represents the separation between the membranes of the two liposomes.

These observations, involving calcium and magnesium, may be consistent with the model proposed by Ohki and Arnold [39], which is based on the addition of Coulomb and hydration repulsions together with van der Waals attraction. We should remark how these authors examine under this model a possible mechanism of ion-induced vesicle fusion. Furthermore, we would like to mention the analogy of our results with the recent work by Lu et al. [46] in which similar contrasting morphologies are documented, from confocal microscopy, in a suspension of colloidal spheres of polymethylmethacrylate. They obtain dense clusters, $d_m = 2.4 - 2.6$, which are induced by a "long" range depletion attraction whereas they found ramified structures, $d_m = 1.7 - 1.8$, as a consequence of a "short" range depletion attraction. In our opinion, the long range depletion in this particular aggregation plays the same role as the total energy in the presence of magnesium whereas the total energy in aggregation of liposomes induced by calcium is equivalent to their "short" range depletion attraction.

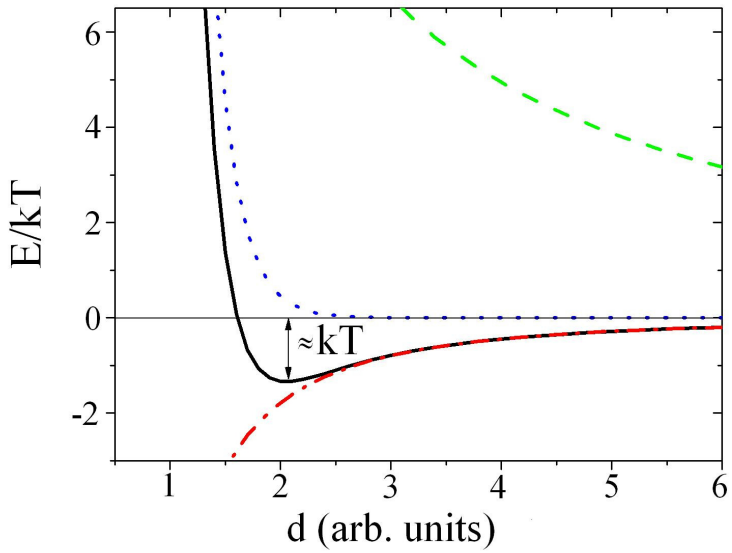

FIG. 9 Qualitative description of the interaction energy E at short distances between two liposomes. The green dashed line stands for the repulsive Coulomb energy (according to a Yukawa functional form), the blue dotted line represents an exponentially decaying hydration energy [36], and the red dashed-dotted line symbolizes van der Waals attraction. In simple terms, when magnesium is added, Coulomb repulsion is screened whereas the hydration interaction persists. The total energy in that case is therefore the result of the addition of van der Waals attraction and hydration repulsion (black solid line). This total energy presents a shallow minimum that conditions the dense cluster morphology of the magnesium induced aggregates. The distance d (arbitrary units) represents the separation between the membranes of the two liposomes.

D. Diffusion coefficient

Experimental data of the time evolution of $\bar{D}_{\exp}(q;t)$ obtained from DLS measurements according to the protocol presented previously are plotted in a double logarithmic scale in Figure 10. Figure 10.a shows $\bar{D}_{\exp}(q;t)/D_0$ for the aggregation processes involving dense mass fractal aggregates (magnesium concentrations of 30 mM, 100 mM and 150 mM), whereas the results corresponding to surface fractals populations (magnesium concentrations of 5 and 7 mM) are shown in Figure 10.b.

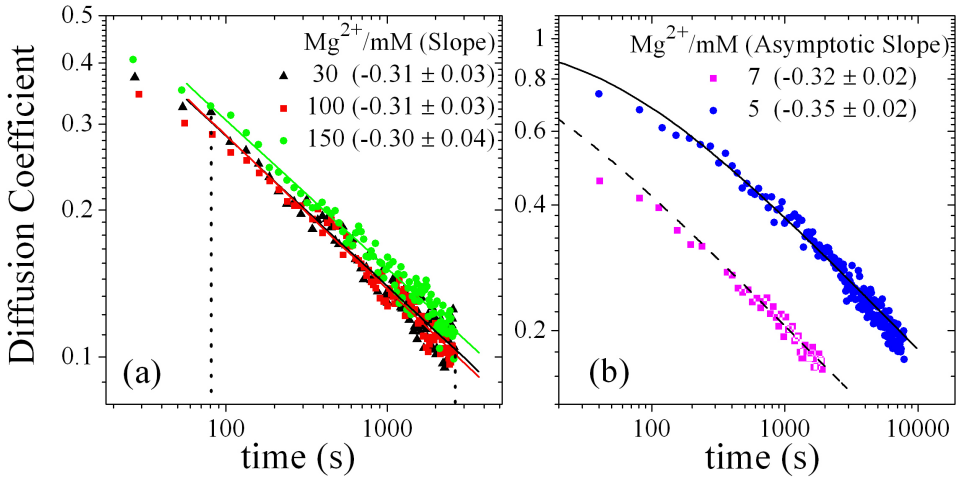

FIG.10 Normalized experimental mean diffusion coefficient $\bar{D}_{\exp}(q;t)/D_0$ as a function of time: (a) Mass Fractals at different magnesium concentrations: 150 mM (green circles), 100 mM (red squares) and 30 mM (black triangles). Linear fit at long times are plotted as solid lines whereas their corresponding slopes appear in brackets. Vertical dot lines denote the interpolation range. (b) Surfaces Fractals at different magnesium concentrations: 5 mM (blue circles) and 7 mM (magenta squares). Solid and dash lines show the numerical solution for Smoluchowski's Equation.

In both cases, all the experimental aggregation kinetics data exhibit a long time behavior consistent with $\bar{D}_{\exp}(q;t) \propto t^{-1/3}$ within the experimental uncertainty, in spite of the time shift between them. Expression (16) indeed gives us a clue to elucidate this common asymptotic behavior by a simple relationship: $3 = (1-\lambda)d_m$. Certain advantage can be taken from our experimental determination of d_m, which showed a common value $d_m = 3$ for the 5 and 7 mM samples. In this case (surface fractals), a value $\lambda = 0$ corresponding to a diffusive aggregation regime seems to be a convenient election. Accordingly, the interaction picture discussed before is coherent with that type of regime since aggregation happens due to the presence of a shallow minimum at short distances without any long-range interaction disturbing the diffusive motion of the clusters before sticking.

As pointed out previously, both D_n and $N_n(t)$ are required in order to account for these experimental data by means of expression (13). The frequency $N_n(t)$ is obtained by

solving Smoluchowski's model under the assumption of a reaction kernel. As our SLS data indicate, we are dealing with uniform clusters. Due to their high compactness, these clusters can be considered as uniform objects, $d_m = 3$, at least for surface fractals structures, whose size grows as $R_n \propto n^{1/3}$. This scaling growth together with our experimental determination $\lambda = 0$ and the assumption of Stokes-Einstein relation, $R_n^{-1} \propto D_n \propto n^{-1/3}$, lead us to the *classical* Brownian kernel $k_{ij} \propto \left(R_i^{1/3} + R_j^{1/3}\right)\left(D_i^{-1/3} + D_j^{-1/3}\right) \propto \left(i^{1/3} + j^{1/3}\right)\left(i^{-1/3} + j^{-1/3}\right)$ as a formal election [37]. In this context, the small-large reaction exponent, which also incorporates the collision cross-section of the aggregates ($k_{1j} \propto j^{\nu}$; $j \to \infty$), is $\nu = 1/3$. Therefore, the theoretical asymptotic behaviour will be essentially conditioned by the cluster compactness, i.e. by d_m.Under this framework, the aggregation processes will be dominated by the small-large clusters reactions and then cluster polydispersity will be discouraged [37]. This aspect is corroborated by the weak q-dependence of $\overline{D}_{\exp}(q;t)$ (see section IV.A) . As a conclusion, if we consider two diffusion-limited aggregation processes involving two different populations of surface fractals, i.e. populations with different d_s, the same values $\lambda = 0$ and $\nu = 1/3$ should be expected, independently of d_s.

In practice, it is found that a constant kernel ($k_{ij} = k_{11}\ \forall i, j$) reproduces essentially the same solution that the *classical* Brownian kernel even at moderate long times. Thus, the experimental values of the diffusion coefficient for the aggregation processes involving surface fractals were fitted using k_{11} as unique free parameter. Figure 10.b shows the results of these fits: in both cases the agreement is good even at short times. The delay between these two aggregation processes is theoretically accounted for by $k_{11}(5\text{ mM}) = \left(2.5 \cdot 10^{-19} \pm 0.5\right)\ \text{m}^3\text{s}^{-1}$ and $k_{11}(7\text{ mM}) = \left(1.6 \cdot 10^{-18} \pm 0.3\right)\ \text{m}^3\text{s}^{-1}$. In our opinion, this delay is due to the different strength of the bound between two vesicles at different magnesium concentrations. At 7 mM the roughness is higher than that at 5 mM and then a vesicle would be, in general, rounded by a less number of neighbours on the surface of an aggregate, being more likely the effective small-large captures during the aggregation process. Therefore, the different values of d_s have influence only on

the delay time during the aggregation process but not on the asymptotic behavior as expected.

This discussion seems to be a key to understand the aggregation kinetics results obtained for dense mass fractals (figure 10.a) even though they need a more complex model to account for them completely. Nevertheless, the mass fractals dimensions obtained at 30 mM, 100 mM and 150 mM magnesium concentrations are not far from that associated to a uniform object ($d_m = 3$). In this respect, as we pointed out previously, the experimental values of $\overline{D}_{\exp}(q;t)$ show a similar long time tendency to that corresponding to surface fractals. In addition, no structural differences were found within the range $30 \le [MgCl_2] \le 150$ (see Table I), i.e. the strength of the bound between two vesicles would not be increased within this range. This is also supported by the aggregation kinetics data shown in figure 10.a, where identical kinetics results (without delay time between them) are obtained at 30 mM, 100 mM and 150 mM, being the evidence for a common kinetics within $30 \le [MgCl_2] \le 150$.

In spite of the good qualitative, and even quantitative, description offered by our basic diffusive model, it should be stressed that other plausible options of reactive kernels could prove useful in order to account for the aggregation kinetics in the presence of magnesium. Certainly, our interpretation is based on the simplified interaction picture sketched in figure 9 together with the experimental evolution of $\overline{D}_{\exp}(q;t)$ and the measured fractal dimensions. This experimental phenomenology and the *a priori* interaction scenario lead us to a basic diffusive aggregation regime, $\lambda = 0$, if we apply van Dongen and Ernst scheme. Thus, the classical Smoluchowski's Brownian kernel seems a sensible choice. However, the previous picture is not the unique suggestive possibility. In this respect, a reaction kernel with a sticking probability [50] obtained from the inter-vesicles interaction could be effective in order to explain the evolution of the measured mass fractal dimensions (from 3 to 2.6) upon increasing magnesium concentration. This option was actually explored in our previous study in the presence of calcium [9], where the evolution from a slow to a DLCA regime was interpreted in terms of a decreasing repulsive barrier (see figure 8) and, consequently, an increasing

sticking probability. In the present work, the evolution of the measured mass fractal dimensions when we increase the magnesium concentration is understood in terms of a small change in the depth of the energy minimum (figure 9), enhancing the strength of the bond between two adhered vesicles. This could be caused by a small reduction of the hydration repulsion as the magnesium concentration is increased. Nevertheless, a more exhaustive study of the fine structure of the IR-absorption associated to the chemical groups of the phospholipid molecule is needed in order to elucidate this point. Furthermore, we feel that the use of reaction kernel would be associated to additional fitting parameters governing the inter-vesicles interaction. Although the values of these fitting parameters would have a predictive meaning, they cannot be specifically contrasted with our current empirical phenomenology. Moreover, in our opinion, and due to the high compactification, a complete model should also contemplate reversibility through a Smoluchowski's equation including fragmentation [51]. Undoubtedly, these refinements deserve to be contemplated in further studies although they are far from the scope of this work.

V. CONCLUSIONS

In this article the aggregation processes of charged phosphatidilserine liposomes induced by the presence of magnesium have been studied. Static and Dynamic Light Scattering, Fourier-Transform Infrared Spectroscopy and Cryo-Transmission Electron Microscopy have been used as experimental techniques. The main conclusions are:

a) The structure of the liposome clusters shows a transition from uniform (surface fractals) to less dense structures (mass fractals) when the magnesium concentration increases. These morphologies contrast with those reported in the presence of calcium at similar electrolyte concentrations.

b) We have proved that the multiple intracluster scattering has an influence on the determination of the fractal dimensions of the aggregates when they are very dense, i.e. at low magnesium concentration. In this respect, a careful experimental study of the

multiple intracluster scattering, based on a cross-correlation scheme, has been performed in order to obtain reliable values of the fractal dimensions. If this effect is not properly corrected, fractal dimensions could be wrongly determined.

c) We have shown that the classical DLVO model cannot explain the different morphologies documented in the presence of calcium and magnesium at identical concentrations. As a result, the hydration energy between liposomes due to the presence of magnesium and calcium should be introduced in order to explain (at least qualitatively) the different cluster morphologies. Thus, by means of Fourier-Transform Infrared Spectroscopy, we propose the measurement of the infrared absorption associated to the lipid headgroups in order to provide a quantitative estimation of the hydration grade of the liposome surfaces.

d) The kinetics of the aggregation processes has been studied through the time evolution of the mean translational diffusion coefficient of the aggregates. The experimental data were fitted solving Smoluchowski´s Equation. It has been shown that the relationship between structure and kinetics is consistent.

ACKNOWLEDGEMENTS

The authors are grateful to "Ministerio de Educación y Ciencia, Plan Nacional de Investigación, Desarrollo e Innovación Tecnológica (I+D+i)", Projects MAT2006-12918-C05-01 -02, and -05, the European Regional Development Fund (ERDF) and "Consejería de Innovación, Ciencia y Tecnología de la Junta de Andalucía" (Project P07-FQM-02496) for financial support.

Reference List

[1] Lasic D.D. *Handbook of Biological Physics*, Elsevier (London, 1995).

[2] Barenholz, Y. Curr. Opin. Colloid Interface Sci. **6**, 66 (2001).

[3] B. B. Mandelbrot, *Fractals, Form, Chance and Dimension* (Freeman, San Francisco, 1977).

[4] D. A. Weitz et al., Phys. Rev. Lett. **54**, 1416 (1985)

[5] J. L. Carrillo et al., Phys. Rev. E. **68**, 61509 (2003).

[6] L. Shen et al., Langmuir **17**, 288 (2001).

[7] P. Pfeifer and J. Avnir, J. Chem Phys. **79**, 3558 (1983).

[8] K. D. Keefer and D.W. Schaefer, Phys. Rev. Lett. **56**, 2376 (1986).

[9] S. Roldán-Vargas et al., Phys. Rev. E **75**, 021912 (2007).

[10] S. Roldán-Vargas et al., Phys. Rev. E (Rapid Communications) **78**, 010902 (2008).

[11] B. V. Derjaguin and L. Landau, Acta Physiochim. USSR **14**, 633 (1941).

[12] E.J.V. Verwey and J. T. D. Overbeek, *Theory of the stability of Lyophobic Colloids* (Elsevier, Amsterdam, 1948)

[13] S. Marcella, Chem. Phys. Lett. **42**, 129 (1976).

[14] D. N. Petsev and P. G. Velikov, Phys. Rev. Lett. **84**, 1339 (2000).

[15] J. Israelachvili and H. Wennerstrom, Nature **379**, 219 (1996).

[16] J. Martin and A. Hurd, J. Appl. Cryst. **20**, 61 (1987).

[17] P. Pfeifer and M. Obert, *The Fractal Approach to Heterogeneous Chemistry* (Chichester, England: Wiley, 1989)

[18] T. Vicsek, *Fractal Growth Phenomena* (World Scientific, 1988).

[19] H. D. Bale and P. W. Schmidt, Phys. Rev. Lett. **53**, 596 (1984).

[20] D. W. Schaefer et al., Phys. Rev. Lett. **52**, 2371 (1984).

[21] C.M. Sorensen, Aerosol Sci. Technol. **35**, 648 (2001).

[22] B.J. Berne and R. Pecora, *Dynamic Light Scattering* (Wiley, New York, 1976).

[23] Z. Chen et al., Phys. Rev. A **37**, 5232 (1988).

[24] M. Lattuada et al., Phys. Rev. E **64**, 61404 (2001).

[25] G. Phillies, J. Chem. Phys. **74**, 260 (1980).

[26] K. Schatzel, J. Modern Optics **38**, 1849 (1991).

[27] J.K.G. Dhont and C. G. de Kruif, J. Chem. Phys. **79**, 1658 (1983).

[28] A. Moussaïd and P.N. Pusey, Phys. Rev. E **60**, 5670 (1999).

[29] G. Odriozola et al., J. Colloid Interface Sci. **240**, 90 (2001).

[30] S.J. Jung et al., Powder Technology **88**, 51 (1996).

[31] D. E. J. Koppel, J. Chem. Phys. **57**, 4814 (1972).

[32] M. Y. Lin, et al. Phys. Rev. A **41**, 2005 (1990).

[33] M.L. Broide, Ph.D. Thesis. Massachusetts Institute of Technology, (1988).

[34] M.Z. Smoluchowski Phys. Z. **17**, 557 (1916).

[35] M.Z. Smoluchowski, Z. Phys. Chem. **92**,129 (1917).

[36] P. G. J van Dongen, and Ernst M. H, Phys. Rev. A **32**, 670 (1985).

[37] J. Martin et al., Phys. Rev. A, **41**, 4379 (1991).

[38] D. M. LeNeveu, P. Rand, and V. A. Parsegian, Nature **259**, 601 (1976).

[39] S. Ohki and K. Arnold, Coll. Surf. B **18**, 83 (2000).

[40] C. Haro-Perez, C. et al., J. Chem. Phys. **119**, 628 (2003).

[41] R. Jullien and R. Botet, *Aggregation and Fractal Aggregates*, (World Scientific, Singapore, 1987).

[42] J. Schüler et al., Biophys. J. **77**,1117 (1999).

[43] W. Hübner and A. Blume, Chemistry and Physics of lipids **96**, 99 (1998).

[44] V. Buzón, E. Padrós, and J. Cladera, Biochemistry **44**, 13354 (2005).

[45] S. Huebner et al., Biophys. J., **76**, 3158 (1999).

[46] F. Bordi et al., Biophys. J. **91**, 1513 (2006).

[47] D. N. Petsev, Langmuir **15**, 1096 (1999).

[48] W. Hübner and A. Blume, Chem. Phys. Lip. **96,** 99 (1998).

[49] P.J. Lu et al., Phys. Rev. Lett. **96**, 28306 (2006).

[50] A. Di Biasio et al., Phys. Rev. E **50**, 1649 (1994).

[51] F. Family et al., Phys. Rev. Lett. **57**, 727 (1986).

Part 3

Glass Transition: Experiment and Simulation

Paper V

Suspensions of Repulsive Colloidal Particles near the Glass Transition: Time and Frequency Domain Descriptions

Suspensions of Repulsive Colloidal Particles near the Glass Transition: Time and Frequency Domain Descriptions

Sándalo Roldán-Vargas[1], Juan de Vicente[1], Ramon Barnadas- Rodríguez[2], Manuel Quesada-Pérez[3], Joan Estelrich[2], and José Callejas-Fernández[1]

[1]Grupo de Física de Fluidos y Biocoloides, Departamento de Física Aplicada, Universidad de Granada, E-18071 Granada, Spain.

[2]Departament de Fisicoquímica, Facultat de Farmàcia, Universitat de Barcelona, E-08028 Barcelona, Catalonia, Spain.

[3]Departamento de Física, Escuela Politécnica Superior de Linares, Universidad de Jaén, Linares, E-23700 Jaén, Spain.

Abstract

We study the relaxation of both spontaneous and shear-induced fluctuations in suspensions of charged-stabilized colloidal particles near the glass transition by dynamic light scattering and rheology. Both observations are here understood in terms of a common structural relaxation process under a hard sphere mode coupling formalism. For ergodic systems, we show that the descriptions of the relaxation dynamics in time and frequency domains are governed by a common set of dynamic parameters. It is further shown that the microscopic ergodicity break-up induces the emergence of the macroscopic glass elasticity.

I. INTRODUCTION

Most of the current hopes to understand the glass transition (GT) phenomenon rely upon the idea of *structural relaxation*: Near the GT, a small change in the static structure of a glass-forming system induces a dramatic change in the system relaxation dynamics [1-3]. To investigate this phenomenon, one of the reference systems amenable to experimentation is a suspension of mesoscopic particles whose interaction is solely mediated by a repulsive potential [4, 5]. In these systems, the caging between nearest neighbors tends to constrain the individual motion when the particles volume fraction, ϕ, is increased. Eventually, if crystallization is bypassed in a controllable fashion [6], a critical volume fraction, ϕ_g, emerges from which only the local motion of the trapped particles remains. As a result of this structural arrest, the system becomes nonergodic, or glassy. While close to the glassy state their microscopic structure does not reveal a significant difference with that associated to a normal liquid, these systems behave as solid-like materials since they can sustain a given shear stress. Thus, their macroscopic liquid-to-solid transition has been associated to the microscopic ergodic-to-nonergodic transition, suggesting that macroscale elasticity arises from microscale structural arrest [7, 8].

So far, the relaxation dynamics of these colloidal systems has been studied extensively by dynamic light scattering (DLS) and rheology. The former have provided a time domain description of the slow system relaxation through the temporal correlation function, $f(q,\tau)$, of the particle-density fluctuations at a given magnitude of the wave vector q [9, 10]. The latter have proved the frequency dependence of the storage, G', and loss, G'', moduli when the system is weakly perturbed by a small shearing force [11]. Based on these experimental studies, the relaxations of these fluctuations have been interpreted separately in terms of structural relaxation processes [8-10]. However, the quantitative connection between these observations has only been investigated vaguely on real systems [7, 12-14].

In this work, we present experimental evidence of the equivalence between both relaxations in suspensions of charge-stabilized mesoscopic particles near the GT. From

light scattering and rheological measurements, our study provides a close interplay between the time and frequency domain descriptions of the GT under a mode coupling formalism. The dynamic parameters governing the ergodic multi-step relaxation observed through $f(q,\tau)$ are also revealed by mechanical spectroscopy using G' and G'' as rheological material functions. Furthermore, the threshold volume fraction at which ergodicity is broken is consistent with that at which the glass elasticity emerges. As a result, both observations are here presented as the manifestations of a common structural relaxation process. Finally, we also show that despite the long-range Coulomb repulsion through which the particles interact, the observed relaxations can be essentially described by the effective hard-sphere (HS) Mode Coupling Theory (MCT).

II. EXPERIMENTAL SYSTEM

In our experiments, we used phosphatidylserine (PS) liposomes dispersed in purified water at different concentrations. Measurements by dynamic and static light scattering on dilute suspensions gave a mean particle diameter of $\sigma = 220nm$ and a polydispersity (relative standard deviation) of about 0.3. As a consequence of the extrusion procedure [15], the liposomes showed a lipid layer thickness of about $5nm$. These thin layers enclosing an aqueous volume (i.e. our liposomes) present a refractive index ($n = 1.36$) slightly different from that of the water, allowing the preparation of nearly transparent suspensions at relatively high volume fractions. Due to the specific ionization of the PS molecule in water, our liposomes are negatively charged. To model their interaction, we considered the repulsive screened Coulomb part of the Derjaguin-Landau-Verwey-Overbeek potential [16]. Thus, using the rescaled mean spherical approximation to fit the experimental static structure factor (SSF), $S(q)$, of several concentrated suspensions, we obtained a mean liposome surface charge $Z = (270 \pm 50)e$ and a reciprocal Debye screening length $\kappa\sigma = 1.63$ for a residual ionic strength of $10^{-6} M$.

III. TIME DOMAIN DESCRIPTION: LIGHT SCATTERING AND MODE COUPLING THEORY

For our microscopic description, we performed light scattering experiments using a three-dimensional DLS spectrometer (LS instruments, Fribourg-Switzerland) with two incident He-Ne laser beams. Suspensions were contained in a cylindrical scattering cell which was immersed in a thermostatized bath at $T = 25\,^{\circ}\mathrm{C}$. With a digital correlator we computed the cross-correlation function of the scattered intensities, detected by two avalanche photodiodes positioned at an equal angle, for which the time-dependent contributions of multiple scattered photons can be neglected [17]. Both the SSFs and the (coherent) dynamic structure factors (DSFs), $f(q,\tau)$, were experimentally determined with a similar protocol as that described in Ref. [18] for a two-color DLS scheme. Ensemble average of $S(q)$ was ensured by continuously rotating the sample during the measurements. To determine $f(q,\tau)$, "brute-force" ensemble averaging was done: The sample was rotated by a small angle between each time-averaged measurement to a different orientation, exploring more than one hundred configurations each of them corresponding to an independent Fourier component. Since our samples did not present a significant influence of multiple scattering, our "brute-force" approach was also tested successfully using the procedure exposed in Ref. [19]. In this respect, the samples corresponding to our highest volume fractions and exhibiting a nonergodic behavior within our time window, showed a maximum deviation smaller than 2% in the nonergodicity parameters obtained by both methods. This result corroborates the statistical reliability of our ensemble averaging and the weak presence of multiple scattering.

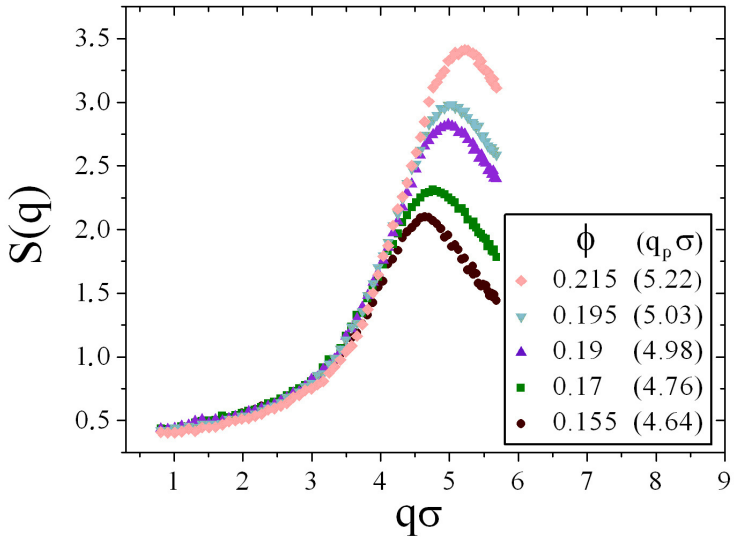

FIG.1 Experimental SSFs at different concentrations. Volume fractions are normalized to unity.

Using the previous protocol, the experimental SSFs for different volume fractions are shown in Fig. 1. The most apparent structural effect is the moderate change in the height and position of the main peak (q_p) upon increasing ϕ. Roughly speaking, a larger height is associated to a higher probability to find two neighbor particles at the most frequent distance whereas the shift to higher q implies a reduction of this distance. The corresponding dynamic information is shown in Fig. 2, where the DSFs measured at the main peaks of the previous SSFs present an archetypal ergodic-to-nonergodic transition. The ergodic systems ($\phi = 0.155$ and 0.17) show multi-step relaxation [2, 3]: Two typical β-decays, reflecting the localized motion of the particles in their cages, which are followed by the cage break-up (α-decay) [20]. For the nonergodic systems ($\phi = 0.19, 0.195,$ and 0.215), only the first β-decay remains (see inset Fig. 2), i.e. the particles only retain some local freedom during an experimental measurement [21]. This strong ϕ dependence of the relaxation time (Fig. 2) associated to a moderate structural change (Fig. 1) is the most prominent signal of a structural relaxation process.

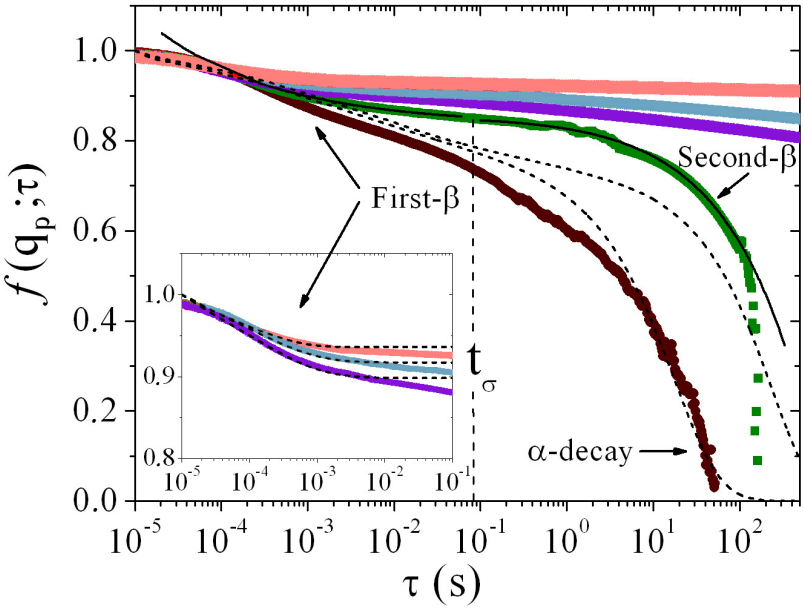

FIG.2 DSFs at the main peaks of the previous SSFs (Fig. 1). Symbols correspond to experimental data as shown in Fig. 1. Dashed lines stand for the MCT solutions (Eq. (1)). Solid lines are an example of interpolation curves for $\phi = 0.17$ according to the predicted power law behaviors for the first and second β-decays. The inset shows a detail of the first β-decay corresponding to the nonergodic systems.

One of the main candidates for a theory of structural relaxation is the MCT. Its simplest version for a glass-forming liquid of identical colloidal particles consists in a discrete set of M integro-differential equations [22]:

$$\frac{1}{D_0}\frac{\partial f(q,\tau)}{\partial \tau} + \frac{q^2}{S(q)} f(q,\tau) + \frac{q^2}{S(q)} \int_0^\tau m(q,\tau-\tau') \frac{\partial f(q,\tau')}{\partial \tau'} d\tau' = 0 \; ; \; \forall q = 1,...,M \qquad (1)$$

where D_0 is the free diffusion coefficient and the $m(q,\tau)$ functions, known as kernels, are mode-coupling functionals expressed in terms of quadratic polynomials combinations: $m(q,\tau) \propto f(p,\tau) f(k,\tau)$ $\left(k, p \in \{1,...,M\}\right)$. The imposed initial conditions are $f(q,0) = 1 \;\; \forall q$. A detailed discussion of the derivation and contents of this model can be found in Ref. [22].

Apart from $S(q)$, if the theory is specialized to a HS system, the unique input parameter is the HS diameter, σ_{MCT}, which is contained in $m(q,\tau)$. A remarkable difficulty appears if we want to use our experimental SSFs (Fig. 1) as input in the MCT equations to explain our dynamic results (Fig. 2): All length scales, then all q-values, are important and have to be considered. Therefore, we extended our experimental SSFs to $q\sigma = 28.4$, i.e. far beyond the observational limit which is placed at $q\sigma = 5.68$ (Fig. 1). This extension was performed by concatenating to our experimental SSFs those obtained from our rescaled mean spherical approximation assuming a monocomponent system. The employed q-range lead to relative errors smaller than 1% for the whole set of parameters defining the α and β decays of $f(q_p,\tau)$. In this respect, a more complete discussion of our methodology will be presented elsewhere.

Despite the "true" long range interaction between our particles, we used Eq. (1) for a $M = 50$ component model with σ_{MCT} as unique fitting parameter, where the numerical discretization was similar as that presented in Ref. [22]. The power law behaviors predicted by the MCT for the first, $f(q_p,\tau) - f(q_p,\infty) \propto (\tau)^{-a}$, and second, $f(q_p,\tau) - f(q_p,\infty) \propto (\tau)^{b}$, β-decays are well supported by the experimental data (Fig. 2). Thus, for our ergodic systems, both the MCT solutions and the fitted power laws present almost constant values for the dynamic exponents which are consistent with those corresponding to a HS system [22]: $a_{MCT} = 0.28 \pm 0.02$ and $b_{MCT} = 0.47 \pm 0.02$ (extracted from the MCT curves) whereas $a_{fit} = 0.30 \pm 0.01$ and $b_{fit} = 0.49 \pm 0.02$ (extracted from the experimental data and corresponding to the average exponents of both $\phi = 0.155$ and $\phi = 0.17$). We should observe that the MCT solutions were adjusted to match the precise location of the plateau, given by the experimental inflection point t_σ (Fig. 2), and not by imposing the best fit for the dynamic exponents. In spite of the good theoretical description of the β-decays, we find deviations in the length and the height of the plateaus between our MCT curves and the experimental data which can be associated to a nonrealistic treatment of the polydispersity of our system [23]. However, this disagreement deserves a more systematic investigation to be elucidated since the true long range interaction between our particles could also have a

non-negligible influence on it. For the nonergodic systems, the MCT predictions also provide an excellent description of the first β-decays (see inset Fig. 2) where $a = 0.33 \pm 0.03$. We emphasize that the whole set of the MCT curves (ergodic and nonergodic systems) are consistent with a ratio $\sigma_{MCT} / \sigma = 1.41 \pm 0.03$. This result also supports the idea that the essential physics of our system can be captured by an effective HS interaction. Concerning the value of ϕ_g, any finite time measurement precludes its precise determination since it is formally associated to a singularity at which the relaxation time diverges. Although the measured $f(q_p, \tau)$ present a nondecaying behavior from $\phi_g \approx 0.19$ within our time window, we can perform an additional test to assume a value for ϕ_g from the power law behavior placed by the MCT for the location of the plateau: $t_\sigma = t_0 |\varepsilon|^{1/2a}$ [2, 3]. Here t_0 is the system microscopic time associated to the initial intra-cage dynamics and $\varepsilon = (\phi_g - \phi)/\phi_g$. Thus, assuming $\phi_g = 0.19$ and according to this scaling behaviour, our experimental t_σ at $\phi = 0.155$ and 0.17 give us a common value $t_0 \approx 10^{-3} s$, which is a coherent time for the initial dynamics of our particles. Contrary to previous works [8], where an experimental time domain description was not performed, we next show that the macroscopic mechanical response of our system to small-amplitude oscillatory shear (SAOS) is also explained by the described spontaneous cage dynamics.

IV. FREQUENCY DOMAIN DESCRIPTION: RHEOLOGY AND MODE COUPLING THEORY

SAOS frequency sweep tests allow to measure viscoelastic observables such as G' and G'', providing a mechanical fingerprint of the material [11]. Although not only the linear [8, 24] but also the nonlinear [25, 26] rheology of colloidal glasses have been described in the past using a mode coupling formalism, here we focus on the linear viscoelastic regime (LVR).

Our rheological tests were carried out using a Paar Physica MCR rheometer. Parallel plates of 40 mm diameter were used to minimize handling problems which frequently

come up for long relaxation time fluids. Precautions were also taken to avoid any sample evaporation: A small amount of low viscosity silicone oil was poured at the rim of the upper disc and, furthermore, a solvent trap was used. To prevent wall slip, surfaces were covered with sandpaper. The temperature was fixed at 25.0 ± 0.1 ºC and controlled using a Peltier. The spacing between the plates was 300 μm (more than 1000 times the typical size of the constituents). The sample was initially subjected to a gentle steady shear rate of 20 s^{-1} during 10 s. After this, a 30 s rest period followed where no shear was applied ensuring that the local stresses created during the cell loading had relaxed and obtaining a reproducible initial state. This way the same structure conditions exist at the beginning of each test. Next, a sinusoidal shear strain was applied to the sample, and the stress response of the material to this deformation was then analyzed. Two kinds of rheological experiments were performed: i) Strain amplitude sweeps at a frequency of 1 Hz to determine the extent of the LVR. ii) Oscillation frequency sweeps in the LVR to obtain the mechanical spectrum of the sample, where $G'(\omega)$ and $G''(\omega)$ were determined, respectively, as the stress in-phase and in-quadrature with the strain divided by the strain amplitude.

The strain amplitude dependence of G' and G'' is shown in Fig. 3. At low volume fractions, G'' is larger than G' as expected for a viscous material. However, upon increasing concentration, G' overpasses G'' ($\phi > 0.18$), presenting a single-stage yielding typical of a repulsive colloidal glass with $G' \approx 10G''$ [27]. We highlight that the volume fraction corresponding to this rheological transition is in agreement with that at which the ergodic-to-nonergodic transition was documented by DLS ($\phi_g \approx 0.19$). This result supports the argument that macroscopic elasticity is a consequence of the microscopic particle-level arrest. Whatever the volume fraction in the nonergodic state, the LVR safely extends up to strain amplitudes of 3 %. Above this strain value, structure breaks, G' decreases and G'' reaches a maximum. Miyazaki et al. [28] provide a qualitative argument to explain this ubiquitous behavior in metastable complex fluids in terms of the MCT, adopting the "isotropically sheared hard-sphere model" [29]. In this respect, we observe that the low-strain storage modulus plateau, G_P, scales with ϕ as $G_P \propto \phi^{12.2\pm1.2}$ (see inset Fig. 3). This power law dependence can be derived from a simple scaling analysis at maximum packing ($r \propto \phi^{-1/3}$) involving a

power law behavior for the interaction potential ($V \propto r^{-n}$) and G_P ($\propto r^{-1}\partial^2 V/\partial r^2$). Accordingly, in our case the interaction potential would scale as $V \propto r^{-34}$, a result which is, once more, in accord with the effective HS-description also supported by our previous DLS study. Furthermore, the volume fraction dependence of G_P and $f(q_p,\tau)$ is also shown in the inset, Fig. 3. A clear correlation exists, suggesting that both the constant G_P-value and the nondecaying behavior of $f(q,\tau)$ do reflect the same physical information. However, the theoretical elucidation of this correlation is still a matter of debate that may be right at the heart of the existence of a true yield stress associated to the onset of flow [30, 31].

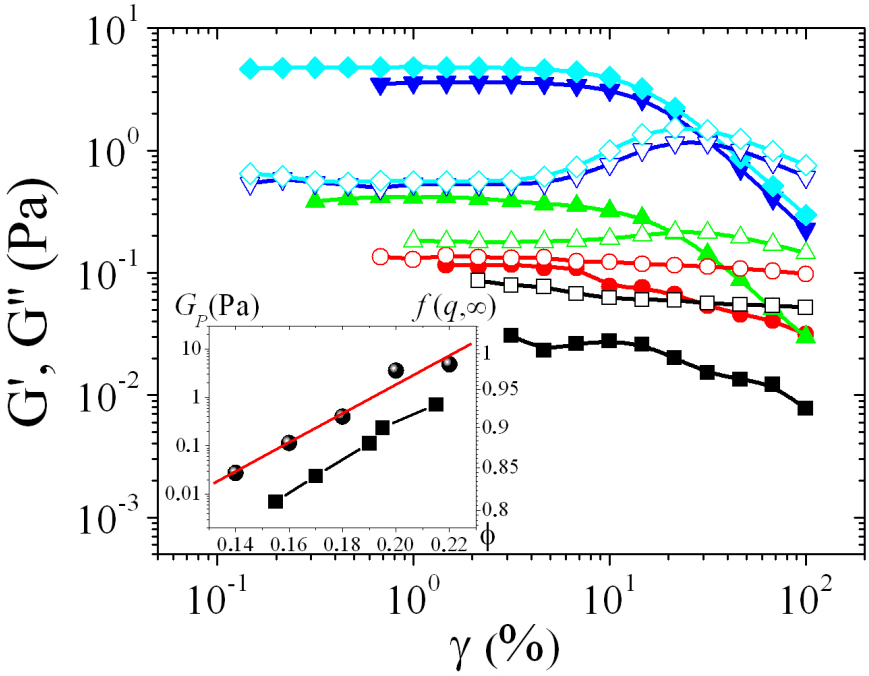

FIG.3 SAOS strain sweep curves at different volume fractions: 0.14 (squares), 0.16 (circles), 0.18 (up triangles), 0.2 (down triangles), 0.22 (diamonds). G' is represented by solid symbols and G'' by open symbols. Lines are plotted to guide the eye. Inset: Volume fraction dependence of G_P and $f(q_p,\infty)$ in the LVR (for the ergodic systems $f(q_p,\infty)$ was taken as $f(q_p,t_\sigma)$, see Ref. [5]).

To understand now the data corresponding to our oscillation frequency experiments, functions in frequency domain for $G'(\omega)$ and $G''(\omega)$ can be proposed for the β-decays via Fourier transformation as a validation of the fluctuation-dissipation theorem [1, 8]:

$$G'(\omega) = G_P + G_\sigma \left[\Gamma(1-a)\cos\left(\frac{\pi a}{2}\right)(\omega t_\sigma)^a - B\Gamma(1+b)\cos\left(\frac{\pi b}{2}\right)(\omega t_\sigma)^{-b} \right] \qquad (2)$$

$$G''(\omega) = G_\sigma \left[\Gamma(1-a)\sin\left(\frac{\pi a}{2}\right)(\omega t_\sigma)^a + B\Gamma(1+b)\sin\left(\frac{\pi b}{2}\right)(\omega t_\sigma)^{-b} \right] + \eta_\infty \omega \qquad (3)$$

where G_σ determines both the functional frequency dependence of $G'(\omega)$ and the magnitude of $G''(1/t_\sigma)$, Γ is the gamma function, η_∞ is the viscosity of the dispersing medium, and $B = 1$ ($B = 0$) for $\phi < \phi_g$ ($\phi > \phi_g$). In Fig. 4, we show a comparison between our experimental results for $\gamma = 1\%$ and the theoretical predictions (Eq. (2) and (3)). It should be stressed that we connected our DLS and rheological experiments by using as input parameters those previously obtained from our DLS measurements (a_{fit}, b_{fit}, and t_σ), G_σ being the unique free parameter. In all cases, a reasonable agreement is found bearing in mind that the observed scatter at low ϕ is due to the limited torque experimental resolution. Once more, a significant change in G' is found somewhere close to the glass transition, $\phi > 0.18$, where $G'(\omega)$ overpasses $G''(\omega)$ for any frequency within the explored ω-range (Fig. 4 (a) and (b)). For our highest ϕ-values ($\phi = 0.2$ and 0.22), G' is almost constant and about one order of magnitude larger than G'', as expected at the glassy state. Finally, G'' shows a minimum at an excitation frequency around $t_\sigma^{-1} = t_0^{-1}|\varepsilon|^{-1/2a}$ (Fig. 4 (b)) which is consistent with our DLS measurements (Fig. 2) [32], enhancing the connection between our time and frequency domain descriptions.

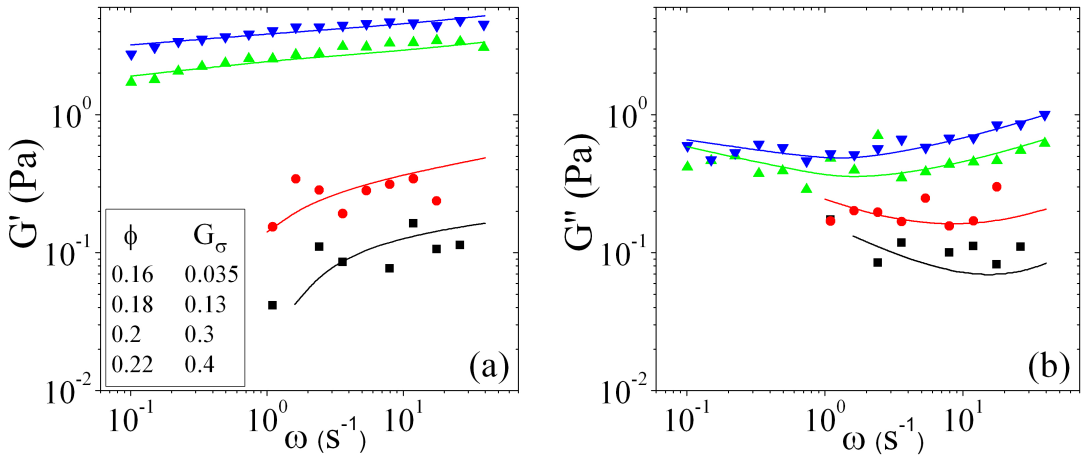

FIG.4 Mechanical spectra in the LVR: (a) $G'(\omega)$ and (b) $G''(\omega)$. Symbols correspond to experimental data as shown in Fig. 3. Lines stand for the MCT predictions (Eq. (2) and (3)).

V. CONCLUSIONS

The relaxations of both spontaneous and shear-induced fluctuations in repulsive colloidal suspensions near the GT have been empirically presented within a common structural relaxation process, supporting their equivalence on a mode coupling formalism. Our work encourages the impetus for more future systematic investigation to highlight the role of this equivalence.

ACKNOWLEDGEMENTS

The authors are grateful to "MICINN" (Projects: MAT2009-13155-C04-02, 03, and -04, MAT2009-14234-C03-03, and MAT2010-15101), ERDF Funds, and "Junta de Andalucía" (Project: P07-FQM-02496) for financial support. We also thank Walter Kob for valuable comments on our manuscript.

Reference List

[1] W. Götze and L. Sjögren, Rep. Prog. Phys. **55**, 241 (1992).

[2] W. Kob, Course 5: *Supercooled Liquids, the Glass Transition, and Computer Simulations,* Les Houches (Springer Berlin, Heidelberg (2003)).

[3] F. Sciortino and P. Tartaglia, Adv. Physics **54**, 471 (2005).

[4] W. Van Megen, T. C. Mortensen, S. R. Williams, and J. Müller, Phys. Rev. E **58**, 6073 (1998).

[5] K. N. Pham, S. U. Egelhaaf, P. N. Pusey, and W. C. K. Poon, Phys. Rev. E **69**, 011503 (2004).

[6] P. N. Pusey, W. van Megen, P. Bartlett, B. J. Ackerson, J. G. Rarity, and S. M. Underwood, Phys. Rev. Lett. **63**, 2753 (1989).

[7] V. Trappe and P. Sandkuhler, Curr. Opin. Colloid Int. Sci. **8**, 494 (2004).

[8] T.G. Mason and D.A. Weitz, Phys. Rev. Lett. **75**, 2770 (1995).

[9] W. van Megen and S. M. Underwood, Phys. Rev. E **49**, 4206 (1994).

[10] W. van Megen and S. M. Underwood, Phys. Rev. Lett. **70**, 2766 (1993).

[11] R.G. Larson, *The Structure and Rheology of Complex Fluids* (Oxford University Press, New York, (1999)).

[12] A. J. Banchio, J. Bergenholtz, and G. Nägele, Phys. Rev. Lett. **82**, 1792 (1999).

[13] L. Ramos and L. Cipelletti, Phys. Rev. Lett. **94**, 158301 (2005).

[14] E. Di Cola et al., J. Chem. Phys. **131**, 144903 (2009).

[15] S. Roldán-Vargas, R. Barnadas-Rodríguez, M. Quesada-Pérez, J. Estelrich, and J. Callejas-Fernández, Phys. Rev. E **79**, 011905 (2009).

[16] G. Nägele, Phys. Rep. **272**, 215 (1996).

[17] K. Schätzel, J. Mod. Opt. **38**, 1849 (1991).

[18] A. Moussaïd and P. N. Pusey, Phys. Rev. E **60**, 5670 (1999).

[19] P. Pusey and W. van Megen, Physica A **157**, 705 (1989).

[20] For our ergodic systems, statistics at long times (final α-decay) is not reliable since we adapted the duration of our measurements to reach only a consistent description of the first and second beta decays. However, the MCT solutions show the predicted stretched exponential decay $f(q_p,\tau) \propto \exp\left(-(\tau)^{\beta}\right)$, where $\beta = 0.82 \pm 0.02$.

[21] We found that our nonergodic systems aged only in the first few hours after tumbling. Then, after a waiting time of one day, we performed independent measurements separated by one day finding no evolution due to aging effects within the time window of the measurements.

[22] T. Franosch, M. Fuchs, W. Götze, M. R. Mayr, and A. P. Singh, Phys. Rev. E **55**, 7153 (1997).

[23] W. Götze and Th. Voigtmann, Phys. Rev. E **67**, 021502 (2003).

[24] G. Nägele and J. Bergenholtz, J. Chem. Phys. **108**, 9893 (1998).

[25] J.M. Brader, M.E. Cates, and M. Fuchs, Phys. Rev. Lett. **101**, 138301 (2008).

[26] J.M. Brader, T. Voigtmann, M. E. Cates, and M. Fuchs, Phys. Rev. Lett. **98**, 058301 (2007).

[27] K.N. Pham et al., Europhysics Lett. **75**, 624 (2006).

[28] K. Miyazaki et al., Europhysics Lett. **75**, 915 (2006).

[29] M. Fuchs and M. E. Cates, Phys. Rev. Lett. **89**, 248304 (2002).

[30] P.C.F. M øller, J. Mewis, and D. Bonn, Soft Matter **2**, 274 (2006).

[31] D. Bonn and M. M. Denn, Science **324**, 1401, (2009).

[32] The emergence of t_σ in both the time and frequency domain descriptions is accounted for by the very nature of the Fourier transformation. On one hand, t_σ is the characteristic time associated to the beta-decays: $f(q_p,\tau)-f(q_p,\infty)\propto(\tau/t_\sigma)^{-a}$ and $f(q_p,\tau)-f(q_p,\infty)\propto(\tau/t_\sigma)^{b}$. On the other hand, via Fourier transformation, the frequency t_σ^{-1} appears as the characteristic counterpart in the frequency domain description given by Eq. (2) and (3).

Paper VI

Non-monotonic Temperature Evolution of Dynamic Correlations in Glass-Forming Liquids

"Wir müssen wissen. Wir werden wissen."*

David Hilbert

* "We must know. We will know." Phrase pronounced at the 1930 annual meeting of the Society of German Scientists and Physicians. It was declaimed in opposition to the 19th century Latin maxim "*ignoramus et ignorabimus"* ("we do not know and we will not know").

Non-monotonic Temperature Evolution of Dynamic Correlations in Glass-Forming Liquids

Walter Kob[1], Sándalo Roldán-Vargas[1, 2], and Ludovic Berthier[1]

[1]Laboratoire des Colloïdes, Verres et Nanomatériaux,
UMR CNRS 5587, Université Montpellier 2, 34095 Montpellier, France

[2]Departamento de Física Aplicada, Grupo de Física de Fluidos y Biocoloides,
Universidad de Granada, 18071 Granada, Spain

Abstract

The viscosity of glass-forming liquids increases by many orders of magnitude if their temperature is lowered by a mere factor of 2-3 [1, 2]. The microscopic mechanisms governing structural relaxation in viscous liquids are not well understood and therefore there exists no well-accepted theoretical explanation for this dramatic evolution that ultimately leads to the glass transition [2]. Recent studies suggest that this widespread phenomenon is accompanied by spatially heterogeneous dynamics [3, 4], and a growing dynamic correlation length quantifying the extent of correlated particle motion [5–7]. However, the microscopic origin, nature and geometry of these collective movements remain largely unknown. Here we use a novel numerical method to detect and quantify spatial correlations which reveals a surprising non-monotonic temperature evolution of spatial dynamical correlations, accompanied by a slower, monotonic growth of a second lengthscale of a very different nature. Our results directly unveil a dramatic qualitative change in atomic motions near the mode-coupling crossover temperature [8] which involves no fitting or indirect theoretical interpretation. We observe a maximum in the size of dynamic correlations that has gone so far undetected, which we interpret as a striking signature of an avoided dynamical critical point. At low temperature, we also observe an accelerated growth of a static correlation length scale, suggesting that the development of amorphous order [9] controls structural relaxation. Our results impose severe new constraints on theoretical descriptions of the glass transition, and open several research perspectives, in particular for experiments, to confirm and quantify our observations in real materials.

More than forty years ago Adam and Gibbs [10] put forward the seminal idea that the relaxation dynamics of highly viscous liquids occurs through 'cooperatively relaxing regions'. Their theory suggested that particle motion occurs in a collective manner in localized domains whose typical size is controlled by entropy, and thus increases with decreasing temperature. This result implied that the relaxation mechanism is controlled by a unique lengthscale of thermodynamic origin with a direct signature in the dynamics. This approach regained momentum in the 1990's when novel experimental techniques and large scale computer simulations established the presence of dynamical heterogeneities, i.e. localized regions where dynamics is significantly different from the average [3, 4], although these observations can also be interpreted as a purely dynamical phenomenon [11].

A qualitatively similar, but much more detailed, theoretical description is obtained within the framework of the random first order transition (RFOT) theory [12]. Within this approach, there exists an ideal glass transition which underlies glass formation, with an associated diverging correlation lengthscale of entropic origin, related to the existence of a large number of long-lived metastable states. At very low temperature, the glassformer is described as a 'mosaic' of correlated domains that rearrange in a thermally activated, collective manner, such that again static and dynamic correlations coincide and grow with the viscosity [13]. However, models with an RFOT (mainly mean-field like models) also display a 'spinodal' singularity at a higher temperature, T_c, at which metastability is lost and therefore the mosaic picture is no longer useful [12, 14]. Thus above T_c, a different approach must be used and it is found that the dynamics within mean-field models [15] has profound similarities with the one predicted from mode-coupling theory [8], where T_c corresponds to a dynamic critical point associated with a diverging dynamical correlation length [16]. Thus, even at the theoretical level, the physics near T_c remains 'mysterious' [17]: How can a dynamical correlation length diverge at two distinct temperatures? The mystery thickens in finite dimensions for which the mode coupling singularity is cut off, and its existence can be inferred only from fitting relaxation data [8], a procedure that is prone to criticisms, and therefore the physical relevance of the 'avoided' singularity at T_c has remained a debated issue.

Progress is also slow because experiments on molecular systems do not have enough resolution to follow atomic motions over long times [3], and numerical simulations often cannot access low enough temperatures to make definite statements on the size and nature of dynamic heterogeneities (in fact there are so far no numerical studies on the dynamical heterogeneities below T_c). At present, the most direct measurements [4] seem to indicate the growth of a dynamical correlation length increasing from 1-2 particle diameters at moderately supercooled temperatures to 5-10 diameters close to the glass transition temperature, but the interpretation of the experimental data is often rather difficult [7].

In parallel to the quest for a dynamical length scale, evidence has also been found for an increasing of static correlations. However, this information is not captured by standard two-point correlation functions. Recent work has for instance suggested the growth of locally favored geometric structures in some model systems [18, 19], but these methods are not easily generalized to different glass-formers. One possibility to tackle this problem are the point-to-set correlations which are an elegant, general method to capture the multi-point static correlations which might characterize the non-trivial structure of viscous liquids [20]. The conceptual idea is to 'pin' the position of a number (or a 'set') of particles in an equilibrated configuration of the fluid, and measure how the position of the remaining particles is affected. It was recently argued that in the geometry in which particles outside a spherical cavity are pinned, this point-to-set correlation should detect the typical domain size of the RFOT theory mosaic state [21]. Numerical simulations confirmed qualitatively the growth of point-to-set correlations in this particular geometry [9]. However, the connection to dynamic correlations and the precise temperature dependence of the various lengthscales were not studied, and these results did not resolve the 'mystery' [17] of the T_c crossover.

Inspired by previous work on confined fluids [22], we have generalized the idea of a point-to-set correlation to a novel geometry. We pin particles in a semi-infinite space and detect the resulting effect on the other half space. The principal advantage is that we can measure simultaneously the static and dynamic profiles induced by the frozen wall.

Additionally we were able to perform simulations from the high temperature liquid down to below T_c with a realistic molecular dynamics, thus allowing us to resolve at once multi-point static and dynamic correlations in a very broad temperature regime encompassing the (hypothetical) mode-coupling crossover.

We study a binary mixture of quasi-hard spheres [23], as described in the Methods. The fluid is equilibrated by means of standard molecular dynamics using periodic boundary conditions in all three directions. To simulate particles pinned within a semi-infinite space, $z < 0$, it is enough to freeze at an arbitrary time $t = 0$ the position of all particles within a slice of thickness $d_{wall} = 1.4\sigma$ which is perpendicular to the $z-$axis: They form our 'set'. Because we use periodic boundary conditions, we work with a very large system size in the z-direction, ensuring that bulk behaviour is recovered at the center of the simulation box, i.e. the replicated walls do not interfere with each other.

To properly measure a point-to-set correlation it is crucial that these frozen walls have the same structure as the equilibrated liquid at temperature T, such that the average static properties of the confined liquid are unperturbed [20, 22]. We have measured how far (in z) the wall influences both the static local density field and its dynamics, giving us independent access to static and dynamic correlation length scales. Note that within RFOT theory, the spatial extent of the static profile near a wall is not directly controlled by the mosaic lengthscale [14], and a comparison with results obtained with a spherical cavity [9] is not immediate.

A convenient observable to characterize the influence of the wall is the overlap profile $q_c(t,z)$, defined as follows [9]. We discretize space into small cubic boxes of linear size $\delta \approx 0.55\sigma$, and define $n_i(t) = 1$ if box i is occupied by at least one particle at time t, and $n_i(t) = 0$ if not.

The overlap profile in the z direction with respect to the template configuration at time $t = 0$ is

$$q_c(t,z) = \left[\frac{\sum_{i(z)} \langle n_i(t) n_i(0) \rangle}{\sum_{i(z)} \langle n_i(0) \rangle} \right]_{wall} , \qquad (1)$$

where the sums run over all boxes at distance z from the wall, $\langle \cdots \rangle$ is the usual thermal average, and $[\cdots]_{wall}$ is an additional average over independent wall realizations. Thus $q_c(t,z)$ quantifies the similarity of particle configurations separated by a time t at distance z, and, by construction, $q_c(t=0,z)=1$, for all z. We also studied $q_s(t,z)$, the single particle version of Eq. (1), obtained by requesting that the box i is occupied at times 0 and t by the same particle.

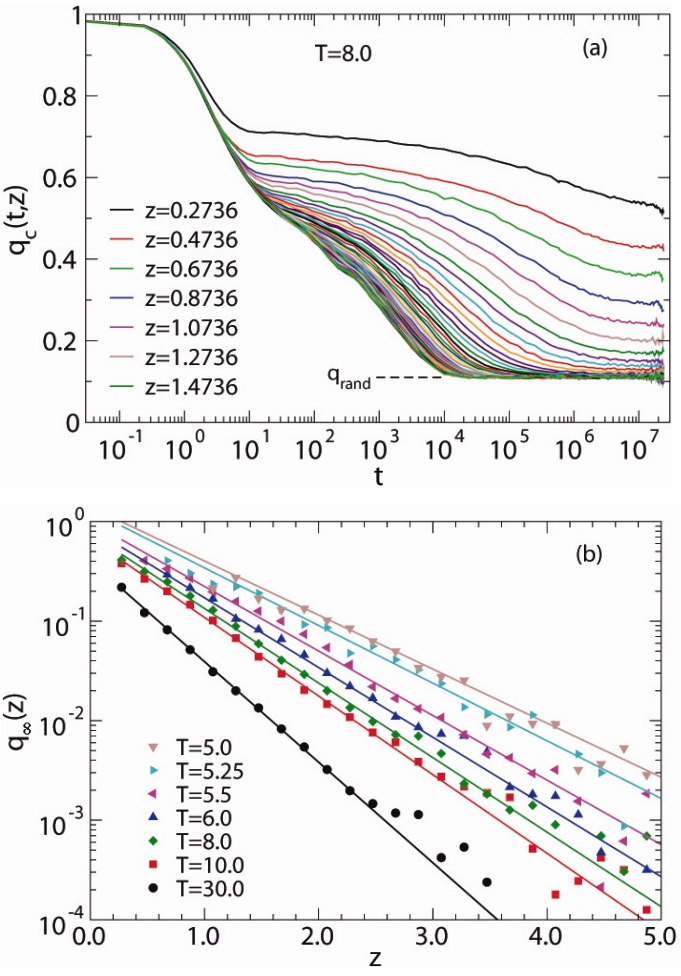

FIG. 1: (a) Time dependence of the overlap $q_c(t,z)$, Eq. (1), for $T = 8.0$ and various values of z, increasing from $z = 0.2736$ (near the wall, rightmost curve) by increments of 0.2. The leftmost curve presents the bulk behaviour. (b) z −dependence of the nontrivial part of the static overlap $q_\infty(z)$ for different temperatures (symbols). The solid lines are fits with the exponential given in Eq. (3).

In Fig. 1a we show the time dependence of $q_c(t,z)$ at $T=8.0$ for different values of z. For large z (leftmost curves) the correlators become independent of z and present the bulk behavior. The presence of a shoulder at intermediate times reflects the usual cage motion of particles observed in glassy systems [2]. In the long-time limit, $t\to\infty$, the correlator decays to $q_{rand}=0.110595$, the probability that a box is occupied, a quantity we measured with high precision from bulk simulations. With decreasing z, the height of the plateau at intermediate times increases and the timescale to reach it decreases. The final decay becomes much slower near the wall than in the bulk, showing that the α-relaxation is strongly affected by the frozen wall. Furthermore the long-time limit of the overlap increases from its trivial value, $q_c(t\to\infty,z)>q_{rand}$, showing that sufficiently close to the wall, the density cannot freely fluctuate. Thus the set of frozen particles with $z<0$ influences the position of the liquid particles at $z>0$ over a non-trivial static lengthscale. Finally, Fig. 1a shows that there exists a range of z values for which the long-time limit of the overlap is the trivial bulk value, while the relaxation timescale is slower than the bulk. This directly shows, with no further analysis, that dynamic correlations have a larger range than static ones, as we confirm below.

To quantify these observations, we fit the final decay of $q_c(t,z)$ to the stretched exponential form

$$q_c(t,z)-q_{rand}=A\exp\left[-(t/\tau)^{\beta}\right]+q_{\infty}, \qquad (2)$$

where A, τ, β, and q_{∞} are fitted for each z. The profile of the static overlap, $q_{\infty}(z)$ measures how far from the wall density fluctuations are correlated, while $\tau(z)$ measures how far dynamics is affected. We found that Eq. (2) also describes well the single particle overlap, $q_s(t,z)$, with the obvious difference that $q_s(t\to\infty,z)=0$, because all particles eventually leave the box that they occupy at $t=0$. Thus, we obtain a second, 'self' dynamic profile from the study of $q_s(t,z)$.

In Fig. 1b, we display the temperature evolution of the static overlap profiles $q_\infty(z)$. The semi-log plot suggests to describe these data using an exponential decay [24]

$$q_\infty(z) = B\exp\left(-z/\xi^{stat}\right), \tag{3}$$

which allows us to define a static point-to-set correlation lengthscale $\xi^{stat}(T)$. From these data it is clear that ξ^{stat} grows when temperature decreases, a result in good qualitative agreement with previous work [9] using a very different geometry. Notice that $B(T)$ also changes rapidly with T, which suggests to define $\xi^{stat-\mathrm{int}} \equiv B(T)\xi^{stat}$ as a convenient estimate of the integrated profile, $\xi^{stat-\mathrm{int}} \approx \int_0^\infty q_\infty(z)dz$.

We now analyse the dynamic profiles. To take into account the fact that the amplitude and stretching of the time dependent correlations evolve with z, see Fig. 1a, we have calculated the area under the correlators $q_c(t,z)$ and $q_s(t,z)$, taking into account only the secondary, slow relaxing part. We denote these resulting times by $\tau_c(z)$ and $\tau_s(z)$, respectively. Previous studies [22] have suggested that for large z the $z-$dependence of $\tau_s(z)$ can be described well by an exponential functional form,

$$\log(\tau_s) = \log\left(\tau_s^{bulk}\right) + B_s\exp\left(-z/\xi_s^{dyn}\right), \tag{4}$$

where $B_s(z)$ and, more importantly, the dynamic lengthscale, $\xi_s^{dyn}(T)$, are adjusted for each z. The bulk relaxation time $\tau_s^{bulk}(T)$ is measured independently with a very good precision, see Fig. 2a. Using a power law fit inspired by mode-coupling theory [8], $\tau_s^{bulk}(T) \propto (T - T_c)^{-\gamma}$, we obtain $T_c \approx 5.2$, but deviations from the algebraic fit appear above T_c near $T = 6.0$, see Fig. 2a.

In Fig. 2b we show that the data at large z can indeed be fitted well by the ansatz in Eq. (4). We have found a similar behaviour for $\tau_c(z)$, providing us with a second dynamic

correlation lengthscale, $\xi_c^{dyn}(T)$. For high temperatures Eq. (4) gives a good description of the data over the entire range of distances z. For intermediate and low temperatures we see the development of a curvature in a semi-log plot, suggesting at small z deviations from the simple exponential dependence. This might suggest, although very indirectly, the appearance of more than one relaxation process for the relaxation dynamics.

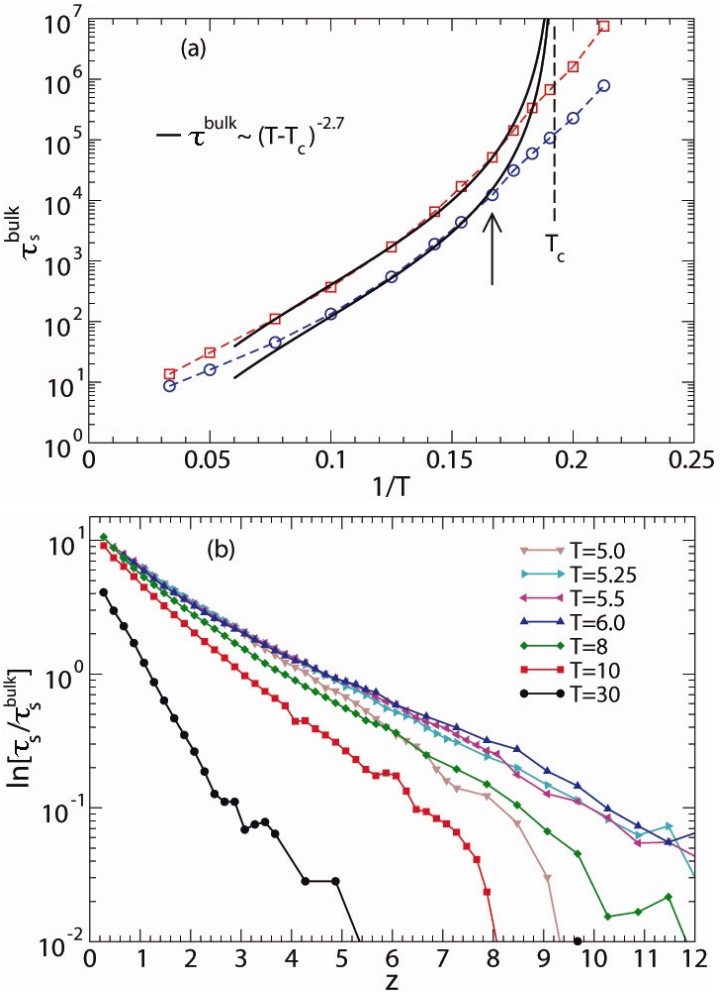

FIG. 2: (a) Temperature evolution of bulk relaxation time for large (top) and small (bottom) particles. Solid lines represent a power-law fit with $T_c \approx 5.2$ (dashed line), the arrow indicates $T = 6.0$ where deviations from the fit appear. (b) z−dependence of the relaxation time $\tau_s(z,T)$ at various temperatures. Note the non-monotonic T−dependence at intermediate and large z.

A remarkable behaviour occurs at intermediate and large distances, which has, to our knowledge, remained undetected. The dynamic profiles exhibit a striking nonmonotonic evolution with temperature. A close inspection of Fig. 2b shows that the dynamic profiles extend to increasingly larger distances when temperature decreases from

$T = 30.0$ down to $T = 6.0$, but become shorter-ranged when T is decreased further, down to $T = 5.25$ and then $T = 5.0$. The maximum occurs near $T = 6.0$, which is also the temperature where deviations from mode-coupling fits appear, see Fig. 2a.

We have carefully checked that this behaviour is not a result of our numerical analysis. A direct visual inspection of the time correlations functions $q_s(z,t)$ reveals that the spread of the curves in the slow decay has a maximum at $T = 6.0$, so that the non-monotonic temperature behavior in Fig. 2a is not an artifact of our fits, but is a genuine effect. In addition, we found very similar results for the collective relaxation time, $\tau_c(z,T)$, which further shows that this non-monotonic behavior does not sensitively depend on the considered observable. Thus, these results give us direct evidence that the relaxation processes responsible of spatial dynamic correlations have a non-monotonic temperature behavior. To our knowledge, all previous numerical and experimental studies of spatially heterogeneous dynamics have reported spatial correlations which grow as the temperature is decreased and dynamics slows down [3–7, 19].

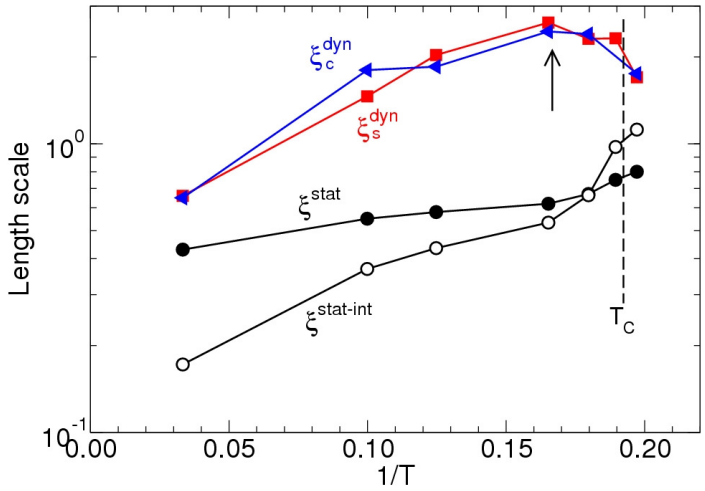

FIG. 3: Temperature dependence of static and dynamic length scales identified in this work. The arrow at $T = 6.0$ and the dashed line at $T_c = 5.2$ are as in Fig. 2. Dynamic length scales display a non-monotonic behaviour with a maximum at $T = 6.0$, while static length scale increase modestly above T_c.

In Fig. 3 we summarize the temperature dependence of the static and dynamic lengthscales identified above. The static length scales show a modest but steady and

monotonic growth with decreasing temperature, which seems to become more pronounced below $T \approx 6.0$. These are natural findings from the RFOT theory perspective [12, 14, 17], in the sense that static correlations should only become prominent below T_c. We also include in Fig. 3 the dynamic lengthscales, which have a striking local maximum near $T = 6.0$. A comparison with Fig. 2a strongly suggests to interpret this maximum in the context of RFOT theory where a dynamic critical point at T_c exists in the mean-field limit (but which is avoided in finite dimensions) whereas activated dynamics governed by growing static correlations appears at low temperatures. Using RFOT theory Stevenson et al. have suggested that around T_c the cooperative domains should indeed change shape, in that they have an open structure above T_c and a more compact structure below T_c [25]. Our findings may be viewed as a striking confirmation of this scenario. Although a gradual change from 'flow-like' to 'hopping' motion was often invoked in the past [8], mainly to rationalize successes and failures of the mode-coupling theory, our results provide a very direct, microscopic evidence of a change of relaxation mechanism which involves no theoretical fitting or indirect interpretation.

If we naively extrapolate our results to lower temperatures, we find a temperature below which static correlations become larger-ranged than dynamic ones, a situation which is physically not very meaningful. We are led to speculate that at much lower temperatures, dynamic lengthscales should exhibit an upturn, and perhaps become slaved to static ones, as in the Adam-Gibbs picture [10] and the scaling regime of RFOT theory [12]. However, studying numerically this final regime is at present too difficult. We suggest that experimental work is needed to resolve these issues further. Our study also suggests that investigations of confined systems should be revisited in both simulations and experiments, and the mode-coupling crossover studied more extensively in glassformers of varying fragility. However, since the model investigated here has no unusual features regarding the relaxation dynamics [23], we expect our results to apply also to other simple models such as hard spheres, Lennard-Jones-like systems, or soft spheres.

Methods– We study an equimolar binary mixture of harmonic spheres [23] with diameter ratio 1.4, with interactions between particle i and j given by

$$V_{ij}(r) = \varepsilon\left(\left|\vec{r}_i - \vec{r}_j\right| - \sigma_{ij}\right)^2 \qquad \text{if} \qquad \left|\vec{r}_i - \vec{r}_j\right| < \sigma_{ij}\,, \tag{5}$$

where $\sigma_{11} \equiv \sigma$ is the unit of length, $\sigma_{12} \equiv 1.2$, and $\sigma_{22} \equiv 1.4$. The total number of particles is 4320 and all of them have the same mass m. Time is expressed in units of $\sqrt{m\sigma^2/\varepsilon}$ and temperature in units of $10^{-4}\varepsilon$, setting the Boltzmann constant $k_B = 1.0$. We have used a rectangular box of size $L_x = L_y = 13.68$ and $L_z = 34.2$, yielding a number $\rho = 0.6749715$. The equations of motion have been integrated with the velocity form of the Verlet algorithm. The longest runs extended over 830 million time steps, which took about 6 weeks of CPU time on a high end processor. In order to improve the statistic of the results we have averaged over 10-30 independent walls. The total amount of computer time to obtain the described results was therefore around 7 years. In practice, to prevent particles to penetrate in the frozen half-space, we introduced at the two surfaces of the frozen slice an infinitely hard wall, and have checked that this frozen geometry has negligible influence on the structure of the fluid. Note that we are investigating here a dynamical equilibrium, i.e. all fluid particles can leave their initial positions and explore the whole confined space, thus assuring thermodynamic equilibrium conditions.

ACKNOWLEDGEMENTS

We thank G. Biroli and A. Cavagna for fruitful exchanges about this work, and the Région Languedoc-Roussillon (L.B.), ANR DYNHET (L.B. and W.K.), and MICINN (Project: MAT2009-13155-C04-02) and Junta de Andalucía (Project: P07-FQM-02496) (S.R.V.) for financial support. W.K. is member of the Institut Universitaire de France.

AUTHOR CONTRIBUTIONS

L.B., W.K., and S.R.V contributed to the computer simulations and analysis of the data and the writing of the paper.

Reference List

[1] P.G. Debenedetti and F. H. Stillinger, Supercooled liquids and the glass transition, Nature **410**, 259 (2001).

[2] K. Binder and W. Kob, Glassy materials and disordered solids, 2nd edition (World Scientific, Singapore, 2010).

[3] M. D. Ediger, Spatially Heterogeneous Dynamics in Supercooled Liquids, Annu. Rev. Phys. Chem. **51**, 99 (2000).

[4] Dynamical heterogeneities in glasses, colloids, and granular media, Eds.: L. Berthier, G. Biroli, J.-P. Bouchaud, L. Cipelletti, and W. van Saarloos, (Oxford University Press, at press).

[5] C. Bennemann, C. Donati, J. Baschnagel, and S. C. Glotzer, Growing range of correlated motion in a polymer melt on cooling towards the glass transition, Nature **399**, 246 (1999).

[6] L. Berthier, G. Biroli, J.-P. Bouchaud, L. Cipelletti, D. El Masri, D. L'Hˆote, F. Ladieu, and M. Pierno, Direct Experimental Evidence of a Growing Length Scale Accompanying the Glass Transition, Science **310**, 1797 (2005).

[7] C. Dalle-Ferrier, C. Thibierge, C. Alba-Simionesco, L. Berthier, G. Biroli, J.-P. Bouchaud, F. Ladieu, D. L'Hˆote, and G. Tarjus, Spatial correlations in the dynamics of glassforming liquids: Experimental determination of their temperature dependence, Phys. Rev. E **76**, 041510 (2007).

[8] W. G¨otze, Complex dynamics of glass-forming liquids: A mode-coupling theory (Oxford University Press, Oxford, 2008).

[9] G. Biroli, J.-P. Bouchaud, A. Cavagna, T. S. Grigera, and P. Verrocchio, Thermodynamic signature of growing amorphous order in glass-forming liquids, Nature Phys. **4**, 771 (2008).

[10] G. Adam and J. H. Gibbs, On temperature dependence of cooperative relaxation properties in glass-forming liquids, J. Chem. Phys. **43**, 139 (1965).

[11] D. Chandler and J. P. Garrahan, Dynamics on the Way to Forming Glass: Bubbles in Space-Time, Annu. Rev. Phys. Chem. **61**, 191 (2010).

[12] T. R. Kirkpatrick, D. Thirumalai, and P. G.Wolynes, Scaling concepts for the dynamics of viscous liquids near an ideal glassy state, Phys. Rev. A **40**, 1045 (1989).

[13] X. Y. Xia and P. G.Wolynes, Fragilities of liquids predicted from the random first order transition theory of glasses, Proc. Natl. Acad. Sci. USA **97**, 2990 (2000).

[14] S. Franz and A. Montanari, Analytic determination of dynamical and mosaic length scales in a Kac glass model , J. Phys. A: Math. Theor. **40**, F251 (2007).

[15] T. R. Kirkpatrick and D. Thirumalai, Dynamics of the structural glass transition and the p-spin interaction spin glass model, Phys. Rev. Lett. **58**, 2091 (1987).

[16] G. Biroli and J. P. Bouchaud, Diverging length scale and upper critical dimension in the Mode-Coupling Theory of the glass transition, Europhys. Lett. **67**, 21 (2004).

[17] G. Biroli and J.-P. Bouchaud, The Random First-Order Transition Theory of Glasses: a critical assessment, to appear in a book on RFOT edited by V. Lubchenko and P.W. Wolynes, arXiv:0912.2542.

[18] D. Coslovich and G. Pastore, Understanding fragility in supercooled Lennard-Jones mixtures. I. Locally preferred structures, J. Chem. Phys. **127**, 124504 (2007).

[19] H. Tanaka, T. Kawasaki, H. Shintani, and K. Watanabe, Critical-like behaviour of glass-forming liquids, Nature Materials **9**, 324 (2010).

[20] A. Montanari and G. Semerjian, Rigorous inequalities between length and time scales in glassy systems, J. Stat. Phys. **125**, 22 (2006).

[21] J.-P. Bouchaud and G. Biroli, On the Adam-Gibbs- Kirkpatrick-Thirumalai-Wolynes scenario for the viscosity increase in glasses, J. Chem. Phys. **121**, 7347 (2004).

[22] P. Scheidler, W. Kob, and K. Binder, Cooperative motion and growing length scales in supercooled confined liquids, Europhys. Lett. **59**, 701 (2002).

[23] L. Berthier and T. A. Witten, Compressing nearly hard sphere fluids increases glass fragility, EPL **86**, 10001 (2009).

[24] G. Parisi, On the replica scenario for the glass transition, arXiv:0911.2265.

[25] J. D. Stevenson, J. Schmalian, and P.G. Wolynes The shapes of cooperatively rearranging regions in glass-forming liquids Nature Phys., **2**, 268 (2006).

Conclusions

What have we learned?

The first part of this dissertation concerns the Brownian dynamics of rigid and deformable mesoscopic particles suspended in a molecular liquid. We have learned that there is no way to discriminate between the (diffusive) motion at long times of rigid and deformable Brownian particles. We have also learned that this discrimination can be made if we explore the Brownian motion at short times, that is, times at which dynamics is still non-diffusive. At such as short times, the Brownian motion of rigid particles is understood in terms of a crossover between ballistic and diffusive motion: The long time tail prediction works. However, for deformable Brownian particles we have to consider not only translational but also deformational motion, where the latter is a consequence of the specific flexibility of the particles. Therefore, merely by appealing Brownian dynamics, we can distinguish between two deformable particles with similar size but different elastic properties. Nevertheless, it is also true that, despite our efforts to understand the Brownian dynamics of deformable mesoscopic particles, a complete theoretical understanding of this motion, including the coupling between translational and deformational degrees of freedom, still remains elusive.

Our second finding also concerns Brownian motion. So far, the most widely used experimental technique to study Brownian motion has been dynamic light scattering (DLS). In this sense, here we have provided a stochastic description of the signal detected in conventional DLS experiments for Markovian observations of the particle position. From a purely theoretical viewpoint, we have shown that this fluctuating signal has a stochastic representation: The Ornstein-Uhlenbeck (OU) process. Thus, the electric fields scattered not only by monodisperse but also by polydisperse Brownian particle systems have been satisfactorily pictured by the notion of the OU process. Concerning practical purposes, we have further shown that this representation results

in a useful tool for characterizing colloidal mixtures of variable size as well as for testing digital correlators. In spite of this finding, we do not have a model for describing adequately the detected signal for non-Markovian observations of the Brownian particle position.

The second part of this dissertation shows an example of structure and dynamics: The fractal organizations arising in an evolving aggregating suspension of charged liposomes as consequence of their short range (London-van der Waals) attractions. We have learned that the short range hydration repulsive forces between lipid membranes play a central role on these aggregation processes. That is, the classical DLVO theory, where hydration forces are not considered, does not explain part of our experimental phenomenology. Thus, if hydration is negligible, e. g. in the presence of divalent Calcium, aggregation kinetics and fractal structures are similar to those reported for more conventional mesoscopic particles such as polystyrene microspheres. However, if hydration is obvious, as in the presence of divalent Magnesium, compact fractal structures scarcely documented in the previous literature emerge: Surface fractals. In this sense, we have reported an interesting transition from surface to mass fractal structures upon increasing Magnesium concentration. Since hydration forces are significant in our study, we have proposed a methodology to quantify the hydration grade of the liposome surfaces by means of Fourier-Transform infrared spectroscopy. However, some important problems remain unsolved such as the elucidation of an adequate theoretical description of the hydration forces and their role to prevent membrane fusion.

The final part of our investigation treats the glass transition phenomenon. Founding our interpretation on the Mode Coupling Theory (MCT), we have shown that the phenomenology in time and frequency domains of the relaxation dynamics of a colloidal system near the glass transition is governed by a common set of dynamic parameters. That is, both descriptions can be understood in terms of a common structural relaxation process. Moreover, our work connects the breakdown of the system ergodicity with the emergence of the glass elasticity. However, we know that MCT has a range of validity. The naive physicist's question arises: Is MCT valid whereas the structure of a glass-forming liquid is similar to that of a normal liquid?

To explore the emergence of “non-liquid” structures in glass-forming liquids, we have proposed a *gedankenexperiment* whose realization has been performed by means of a molecular dynamics simulation. As a result, we observed the accelerated growth of an amorphous structural order near the mode-coupling crossover temperature. This acceleration is accompanied by a striking dramatic change in the system relaxation dynamics which had been so far undetected. This latter effect leaves its signature as a maximum in the size of the dynamic correlations. Could our results be an initial step to confirm the MCT crossover? Does our growing static correlation length control structural relaxation near the glass transition? Can we construct a solid theoretical “bridge” between these structures and the system relaxation dynamics? Hopefully, our work will encourage future systematic investigation devoted to answer these questions.

Conclusiones

¿Qué hemos aprendido?

En la primera parte de esta disertación hemos estudiado la dinámica Browniana de partículas mesoscópicas rígidas y deformables suspendidas en un líquido molecular. Hemos aprendido que no podemos discriminar entre el movimiento difusivo (a tiempos largos) de partículas rígidas y deformables. Hemos aprendido también que esta discriminación es posible si exploramos el movimiento Browniano a tiempos cortos, esto es, tiempos para los cuales la dinámica no es todavía difusiva. Para estos tiempos, el movimiento de las partículas Brownianas rígidas presenta un cambio que puede ser entendido como una transición de movimiento balístico a movimiento difusivo: la predicción de "la cola a tiempos largos" funciona. Sin embargo, para partículas Brownianas deformables debemos considerar no sólo el movimiento de traslación sino también el movimiento de deformación, siendo este último una manifestación de la flexibilidad de la partícula. De esta manera, simplemente apelando al estudio de la dinámica Browniana, podemos distinguir entre dos partículas deformables que tengan un tamaño similar pero diferentes propiedades elásticas. En cualquier caso, es también cierto que, a pesar de nuestros esfuerzos por entender la dinámica Browniana de partículas deformables, carecemos todavía de una comprensión teórica completa de este movimiento que incluya el acoplamiento entre grados de libertad de traslación y deformación.

Nuestro segundo resultado se refiere también al movimiento Browniano. Hasta hoy, la técnica experimental más ampliamente utilizada para el estudio del movimiento Browniano ha sido la dispersión dinámica de luz (que aquí notaremos con su acrónimo inglés, DLS). En esta disertación, hemos descrito estocásticamente la evolución temporal de la señal detectada en experimentos convencionales de DLS para observaciones Markovianas de la posición de las partículas. Desde un punto de vista

puramente teórico, hemos mostrado que esta señal fluctuante posee una representación estocástica bien definida: el proceso de Orsntein-Uhlenbeck (OU). Así, la señal correspondiente al campo eléctrico dispersado no sólo por sistemas monodispersos sino también por sistemas polidispersos ha sido satisfactoriamente representada mediante la noción de proceso de OU. En cuanto a la aplicación práctica, hemos mostrado además que esta representación deviene en una herramienta útil para la caracterización de mezclas coloidales de tamaños variables, así como para la calibración de correladores digitales. A pesar de haber logrado ciertos objetivos, no poseemos un modelo estocástico adecuado con el que describir la señal detectada para observaciones no Markovianas de la posición de las partículas.

La segunda parte de esta disertación muestra un ejemplo de estructura y dinámica: las organizaciones fractales que emergen en una suspensión agregante de liposomas cargados como consecuencia de sus interacciones atractivas de corto alcance (London-van der Waals). Hemos aprendido que las fuerzas repulsivas de hidratación entre membranas lipídicas juegan un papel central en estos procesos de agregación. De esta manera, si la hidratación es despreciable, como ocurre en presencia del catión de Calcio divalente, la cinética de agregación y las estructuras fractales resultantes son similares a las documentadas para otras partículas mesoscópicas más convencionales, v. g. partículas de poliestireno. Sin embargo, si la hidratación es patente, como ocurre en presencia del catión de Magnesio divalente, aparecen estructuras compactas que hasta ahora han tenido una presencia muy escasa en la literatura precedente: los fractales de superficie. En este sentido, hemos documentado una interesante transición entre fractales de superficie y fractales de masa a medida que aumentamos la concentración de Magnesio. Dada la relevancia de las fuerzas de hidratación en este trabajo, hemos propuesto una metodología para cuantificar el grado de hidratación de las superficies lipídicas de nuestras partículas mediante el uso de espectroscopía de infrarrojos. No obstante, quedan todavía problemas abiertos tales como la dilucidación de un marco teórico con el que describir las fuerzas de hidratación así como su papel para prevenir la fusión entre membranas lipídicas.

La parte final de nuestra investigación aborda el fenómeno de la transición vítrea. Basando nuestra interpretación en la teoría de modos acoplados (usamos aquí su acrónimo inglés, MCT), hemos mostrado que las descripciones fenomenológicas en los dominios del tiempo y la frecuencia de la dinámica de relajación de un sistema coloidal cercano a la transición vítrea, están gobernadas por un conjunto común de parámetros dinámicos. Esto nos dice que ambas descripciones pueden ser entendidas en base a un proceso de relajación estructural común. Hemos conectado, además, la ruptura de la ergodicidad del líquido vítreo con la aparición de la elasticidad propia del vidrio. Sin embargo, sabemos que la MCT tiene un rango de validez. Llega entonces la pregunta del físico ingenuo: ¿Es la MCT válida mientras la estructura del líquido vítreo es similar a la de un líquido normal?

Con objeto de explorar la aparición de estructuras "no-líquidas" in líquidos vítreos, hemos propuesto un experimento mental (*gedankenexperiment*) cuya realización se ha llevado a cabo mediante una simulación de dinámica molecular. Como resultado, observamos el crecimiento acelerado de un orden estructural amorfo cerca de la temperatura de transición de la MCT. Esta aceleración está acompañada por un cambio dramático y significativo en la dinámica de relajación del sistema que hasta ahora no había sido detectado. Este último efecto deja su firma a modo de máximo en el tamaño de las correlaciones dinámicas. ¿Podrían ser nuestros resultados un paso inicial para confirmar la existencia de la transición predicha por la MCT? ¿Nuestra longitud estática creciente controla la relajación estructural cerca de la transición vítrea? ¿Podemos construir un puente sólido entre estas estructuras y la dinámica de relajación del sistema? Tal vez, nuestro trabajo impulse la aparición de investigaciones sistemáticas futuras dedicadas a dar respuesta a estas preguntas.

APPENDIX A

Resolution of the Smoluchowski Equations

As mentioned in Chapter 4 (section 4.4), the existence of an explicit solution for the set of Smoluchowski Equations (4.16) depends on the chosen kernel. Not unfrequently, Equations (4.16) have to be solved numerically, e.g. the Brownian kernel (4.24) and the RLCA kernel (4.25) (see also Paper III, section IV.C). Accordingly, in this appendix we present a simple method, used within this dissertation, to obtain and validate the numerical solution of Equations (4.16) for those cases with no analytical solution. Our procedure is based on a Runge-Kutta fourth order explicit method. To have a precise approach to the mathematical and programming fundamentals, the reader can consult references [1, 2] at the end of this appendix.

By definition, an explicit method allows us to express the value of the unknown function $y(t+h)$ at time $t+h$ as a function of its values at previous times. One simple case is:

$$y(t+h) = F\left(y(t), t\right) \tag{A.1}$$

Where $y(t+h)$ is an explicit function of $y(t)$ and time. Thus, relation (A.1) can be used as basis to solve numerically the complete problem:

$$\frac{dy(t)}{dt} = f\left(y(t), t\right) \quad , y(0) = y_0 \tag{A.2}$$

In the case of the Runge-Kutta fourth order explicit method, problem (A.2), under the explicit option (A.1), results in the well known discretization:

$$
\begin{aligned}
&y(t+h) = y(t) + \frac{h}{6}\left(k_1 + 2k_2 + 2k_3 + k_4\right) \quad , y(0) = y_0 \\
&k_1 = f\left(y(t), t\right) \\
&k_2 = f\left(y(t) + \frac{h}{2}k_1, t + \frac{h}{2}\right) \\
&k_3 = f\left(y(t) + \frac{h}{2}k_2, t + \frac{h}{2}\right) \\
&k_4 = f\left(y(t) + hk_3, t + h\right)
\end{aligned}
\tag{A.3}
$$

Where relation (A.3) presents four evaluations within the interval $[t, t+h]$, two of them at the extremes (k_1 y k_4) whereas the others, doubly weighted, are evaluated at the middle point $t + h/2$ (k_2 y k_3). With these evaluations, this method has an error of the order of h^4 for the interval $[t, t+h]$.

The Smoluchowski problem (4.16) with initial monomeric conditions involves an additional difficulty since, in principle, it is formally defined for an increasing set of Equations (expressed here in terms of the aggregation time T):

$$
\begin{aligned}
&\frac{dX_n(T)}{dT} = \frac{1}{2}\sum_{i+j=n} K_{ij}X_iX_j - X_n\sum_{i=1}^{\infty} K_{ni}X_i \equiv f_n(\vec{X}, K_{ij}) \\
&\vec{X}(0) = (1, 0, \ldots)
\end{aligned}
\tag{A.4}
$$

Or equivalently:

$$
\begin{aligned}
&\frac{d\vec{X}(T)}{dt} = \vec{f}\left(\vec{X}(T)\right) \quad , \vec{X}(0) = (1, 0, \ldots) \\
&\vec{X}(T) = (X_1(T), X_2(T), \ldots) \\
&\vec{f}\left(\vec{X}(T)\right) = \left(f_1(\vec{X}(T)), f_2(\vec{X}(T)), \ldots\right)
\end{aligned}
\tag{A.5}
$$

If we now apply (A.3):

$$\vec{X}(T+h)=\vec{X}(T)+\frac{h}{6}\left(\vec{k}_1+2\vec{k}_2+2\vec{k}_3+\vec{k}_4\right) \quad ,\vec{X}(0)=(1,0,...)$$
$$\vec{k}_1=\vec{f}\left(\vec{X}(T)\right)$$
$$\vec{k}_2=\vec{f}\left(\vec{X}(T)+\frac{h}{2}\vec{k}_1\right) \qquad \text{(A.6)}$$
$$\vec{k}_3=\vec{f}\left(\vec{X}(T)+\frac{h}{2}\vec{k}_2\right)$$
$$\vec{k}_4=\vec{f}\left(\vec{X}(T)+h\vec{k}_3\right)$$

In our study (Chapter 4 and Paper III), we used a simple cut off on the number of equations, that is, we imposed a previous dimensionality to $\vec{X}(T)$ and $\vec{f}\left(\vec{X}(T)\right)$. In this sense, there are methodologies to approximate the computation of the non-considered Equations (see reference [3]). In practice, these implementations are only worthwhile in those cases where the homogeneity parameter, λ, Equation (4.26), is large, e.g. product kernel ($\lambda=2$). Nevertheless, to ensure the reliability of our cut off, we first introduced a control on the conservation of the number of monomers from $T=0$ to T_{final} (see Paper III, section IV.C):

$$\left|\sum_{i=1}^{Nc} iX_i(T)-1\right|\leq\varepsilon\approx 0 \quad ,\forall T\leq T_{final} \qquad \text{(A.7)}$$

Where $\varepsilon<<1$ is the imposed accuracy, Nc being the number of computed Equations, that is, $\vec{X}(T)=\left(X_1(T),...,X_{Nc}(T)\right)$. However, condition (A.7) is insufficient to ensure the convergence to the real solution since we need not merely to ensure stability but also consistency (Lax equivalence theorem [1]). In this sense, an efficient and obvious criterion is to decrease the time step h until we reach the required constant solution. Thus, our problem couples the input ternary set (h, Nc, T_{final}) with the accuracy ε.

To test our input parameters, we satisfactorily reproduced the analytical solution for the constant and sum kernels (Equations (4.18) and (4.19)), whose asymptotic behavior is

equal or faster than that presented by the Brownian and RLCA kernels (Paper III). The Brownian and constant kernels are characterized by $\lambda = 0$, the fastest RLCA kernel in Paper III by $\lambda = 0.28$, and the sum kernel by $\lambda = 1$. Thus, we found that the ternary set ($h = 5 \cdot 10^{-3}$, $Nc = 500, T_{final} = 50$) with $\varepsilon = 10^{-5}$ provides us with a reliable result.

Finally, we offer our algorithm which can be easily specialized to the Euler or Runge-Kutta second order methods by taking $m = 1$ or $m = 1,2$ respectively.

Runge-Kutta four order explicit method for solving Smoluchowski's Equations

<Input parameters (h, Nc, T_{final}, ε)>

<Select kernel>

<Set initial conditions ($T = 0$), e.g. monomeric initial conditions: $\vec{X}(0) = (1,0,0,...)_{1xNc}$

Time loop ($T \leq T_{final}$)

$T = T + h$ (h preferably adaptative)

Number of Equations loop ($n = 1,..., Nc$)

Runge-Kutta order loop ($m = 1,...4$)

<Evaluation of $k_m\left(f_n(\vec{X}(T)\right)$>

End Runge-Kutta order loop

$$X_n(T+h) = X_n(T) + \frac{h}{6}\left[k_1(f_n) + 2k_2(f_n) + 2k_3(f_n) + k_4(f_n)\right]$$

End Number of Equations loop

< Control on the conservation of the number of monomers (A.7)>

<Evaluation of the average over the population $\vec{X}$, e.g. Diffusion coefficient>

End time loop

Reference List

[1] M. Abramowitz and I. A. Stegun, *Handbook of Mathematical Functions*, Dover Publications, New York (1968).

[2] W. H. Press, B. P. Flannery, S. A Teukolsky, and W. T. Vetterling, *Numerical Recipes in The Art of Scientific Computing* Cambridge University Press; 2ed. (1992).

[3] G. Odriozola, *Agregación Reversible en sistemas coloidales en medios binarios*, Tesis Doctoral, Universidad de Granada (2000).

APPENDIX B

Resolution of the MCT Equations

This appendix is dedicated to the numerical discretization of the MCT Equations for monocomponent colloidal systems, Equations (5.4)[38]:

$$\frac{1}{D_0}\partial_t f(q,t) + \frac{q^2}{S(q)} f(q,t) + \frac{q^2}{S(q)} \int_0^t m(q,t-t')\partial_{t'} f(q,t')dt' = 0\,; \quad (f(q,t=0)=1) \;\; \forall \mathrm{q} \tag{B.1}$$

In particular, here we offer a recipe for the time-discretization which will be completed with the q-discretization presented in reference [2] for a hard-spheres (HS) system.

First, we use the right Riemann sum to approximate the integrals:

$$\int_{t=0}^{t} y(q,t')dt' \cong \sum_{i=1}^{N} y(q,t_i)\left[t_i - t_{i-1}\right] \tag{B.2}$$

Derivatives will be approximated by the forward Euler method:

$$\partial_t y(q,t)\big|_{t=t_i} \cong \frac{y(q,t_i) - y(q,t_{i-1})}{t_i - t_{i-1}} + O\left((t_i - t_{i-1})^2\right) \tag{B.3}$$

Thus, the first step ($t = t_0 = 0 \rightarrow t = t_1$) corresponding to the integral results:

$$\int_{t=0}^{t_1} m(q,t_1 - t')\partial_{t'} f(q,t')dt' \cong m(q,0)\left[f(q,t_1) - f(q,0)\right] \tag{B.4}$$

[38] For an extention to binary mixtures the reader can consult ref. [1] at the end of this appendix.

Now, we proceed in the same way for the second step ($t_0 = 0 \rightarrow\ t = t_2$):

$$\int_{t=0}^{t_2} m(q,t_2 - t')\partial_{t'} f(q,t')dt' = \int_{t=0}^{t_1} m(q,t_2 - t')\partial_{t'} f(q,t')dt' + \int_{t_1}^{t_2} m(q,t_2 - t')\partial_{t'} f(q,t')dt' \cong$$
$$\cong m(q,t_2 - t_1)\left[f(q,t_1) - f(q,0)\right] + m(q,0)\left[f(q,t_2) - f(q,t_1)\right] \qquad \text{(B.5)}$$

Here we have to note that, in general, the time-discretization will be adaptative, that is, it will not be equidistant: $t_n - t_m \neq t_{n-m}$ ($n > m$: $n,m \in N$). Therefore, we will take as $t_n - t_m$ the nearest time to $t_n - t_m$ which had already been computed. We will notate this time as t_{nm}. Then, we can rewrite $m(q,t_2 - t_1)$, Expression (B.5), as $m(q,t_{21})$.

Finally, for $t_0 = 0 \rightarrow\ t = t_{n+1}$:

$$\int_{t=0}^{t_{n+1}} m(q,t_2 - t')\partial_{t'} f(q,t')dt' \cong \sum_{j=1}^{n} m(q,t_{(n+1)j})\left[f(q,t_j) - f(q,t_{j-1})\right] +$$
$$+ m(q,0)\left[f(q,t_{n+1}) - f(q,t_n)\right] \qquad \text{(B.6)}$$

If we now incorporate the non-integral terms of the Equations (B.1), by also using (B.3), we obtain the expected explicit expression for $f(q,t_{n+1})$:

$$f(q,t_{n+1}) = \frac{f(q,t_n)\left[\dfrac{1}{q^2 D_0 (t_{n+1} - t_n)} + m(q,0)\right] - \displaystyle\sum_{j=1}^{n} m(q,t_{(n+1)j})\left[f(q,t_j) - f(q,t_{j-1})\right]}{\dfrac{1}{q^2 D_0 (t_{n+1} - t_n)} + \dfrac{1}{S(q)} + m(q,0)} \;;\; n \geq 1$$

$$f(q,t_1) = \frac{f(q,0)\left[\dfrac{1}{D_0 t_1} + m(q,0)\right]}{\dfrac{1}{q^2 D_0 t_1} + \dfrac{1}{S(q)} + m(q,0)} \quad ;\quad f(q,t_0 = 0) = 1 \;\; \forall q \qquad \text{(B.7)}$$

Equations (B.7), which provide us with $f(q,t_{n+1})$ as a function of its preceding values, must be completed by introducing the q-discretization of the kernel $m(q,t)$ (See Chapter 5, section 5.1, Expressions (5.5) and (5.6)). For a HS system, this discretization takes the form [2]:

$$m(q,t) = \frac{n(\Delta qd)^3}{32d^3\pi^2}\sum_{\hat{k}}\sum_{\hat{p}}{}' S(q)S(k)S(p)\left(\hat{k}\hat{p}/\hat{q}^5\right)\times$$
$$\times\left[\left(\hat{k}+\hat{q}-\hat{p}\right)c(\hat{k})+\left(\hat{p}+\hat{q}-\hat{k}\right)c(\hat{p})\right]^2 f(k,t)f(p,t) \qquad \text{(B.8)}$$

Where, again, n represents the number density of particles, $c(q)=\left(S(q)-1\right)/nS(q)$ is the direct Ornstein-Zernike relation, d the HS diameter, Δqd the non-dimensional step size, $\hat{q}=qd/\Delta qd$, $\hat{k}=qk/\Delta qd$, and $\hat{p}=qp/\Delta qd$. Finally, the prime at the sum represents the restriction:

$$\left|\hat{q}-\hat{k}\right|+1/2\le\hat{p}\le\hat{q}+\hat{k}-1/2 \quad \text{where } \hat{p},\hat{k}=1/2,3/2,... \qquad \text{(B.9)}$$

Thus, Expressions (B.7), (B.8), and (B.9) offer the numerical solution of the MCT Equations (B.1) for a HS system. Accordingly, figure 1 shows a simple scheme from which we see how $f(q_j,t_i)$ depends on the previous times and also on the coupling of the different q.

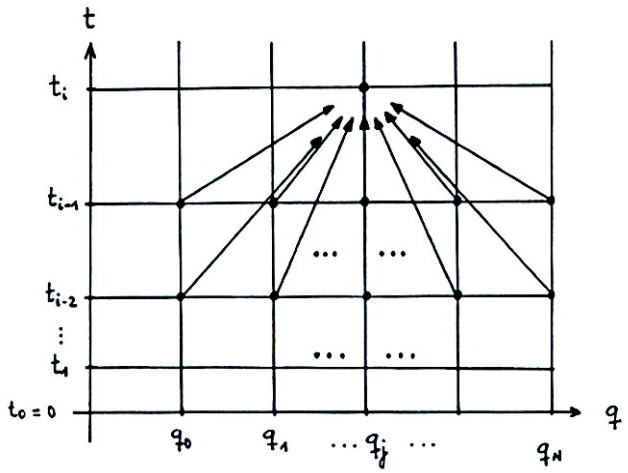

FIG. 1: MCT Scheme: time and q discretizations.

To perform a rough test, we compared our results (Equations (B.7), (B.8), and (B.9)) with those corresponding to a Brownian dynamics simulation for a HS-like system (Ref. [3]). As input we use the discrete version (40-component model) of the static structure factor coming from the mentioned simulation (see figure 2).

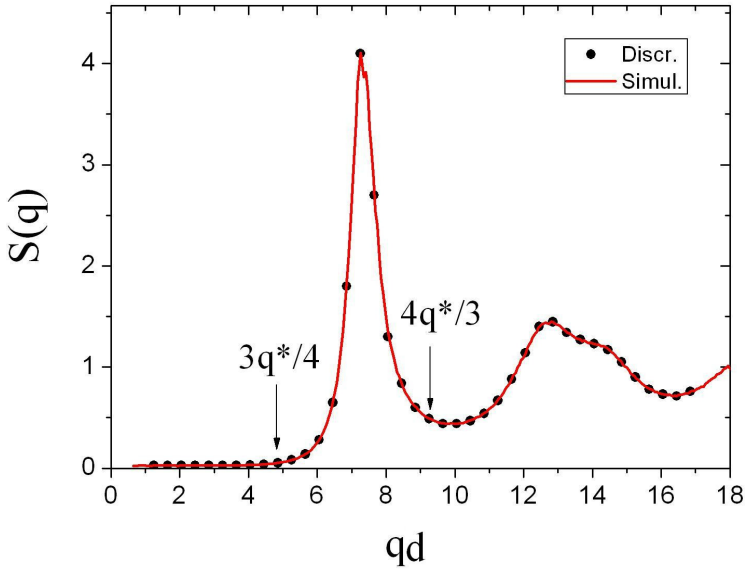

FIG. 2: 40-Equations model (dots), Equations (B.8) and (B.9). The q-discretization is: $1.25 < qd < 16.85$, $\Delta qd = 0.4$. "Continuous" $S(q)$ (red line): Brownian Dynamics simulation of a HS-like system at $\phi = 0.585$ (10% polydispersity) [3].

As first comparison, figure 3 shows the results obtained from Equations (B.7), (B.8), and (B.9) at the mean peak of the normalized dynamic structure factor, q^*, (Fig. 2) and those corresponding to the Brownian dynamics simulation of reference [3]. We found $\lambda = 0.75$, to be compared with the MCT prediction for hard spheres: $\lambda_{HS} = 0.735$ ($a_{HS} = 0.312$ and $b_{HS} = 0.583$) [2] (see also Chapter 5, section 5.1). For the final α-decay we obtained $\beta = 0.84$. Units of time and length were conveniently normalized by taking $d = 1$ whereas the free diffusion coefficient was fixed according to the optimization criterion*: $f_{MCT}(q^*,t) \approx f_{Brownian\ dynamics}(q^*,t)$. An additional "shift" was applied where $\phi_{MCT} = 0.53 \rightarrow \phi_{Brownian\ dynamics} = 0.585$ (see Chapter 5, section 5.1).

* $D_0 \in R^+$ minimizes $\left\{\sum_i \left[f_{MCT}(D_0;q^*,t_i) - f_{Brownian\ dynamics}(q^*,t_i)\right]^2\right\}$.

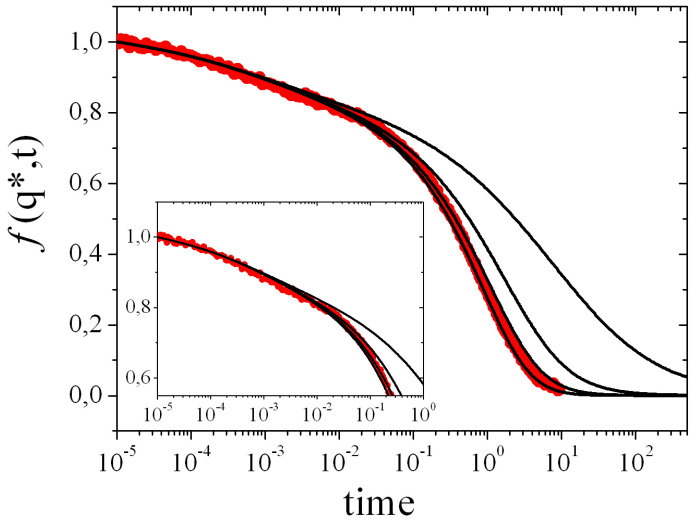

FIG. 3: Dynamic structure factor at the mean peak of the corresponding static structure factor (Fig. 2). Black lines (up to down) correspond to four different adaptative time-discretizations: 400, 800, 1600, and 3200 time steps respectively. Red dots stand for the results of the Brownian dynamics simulation [3].

Finally, figure 4 shows $f(q,t)$ for two additional q values: $3q*/4$ and $4q*/3$ (see Fig. 2). Here again, the optimization criterion was $f_{MCT}(q*,t) \approx f_{Brownian\ dynamics}(q*,t)$. In this sense, we clearly see the emergence of deviations presumably due to the right and left cut offs in the number of the computed MCT Equations.

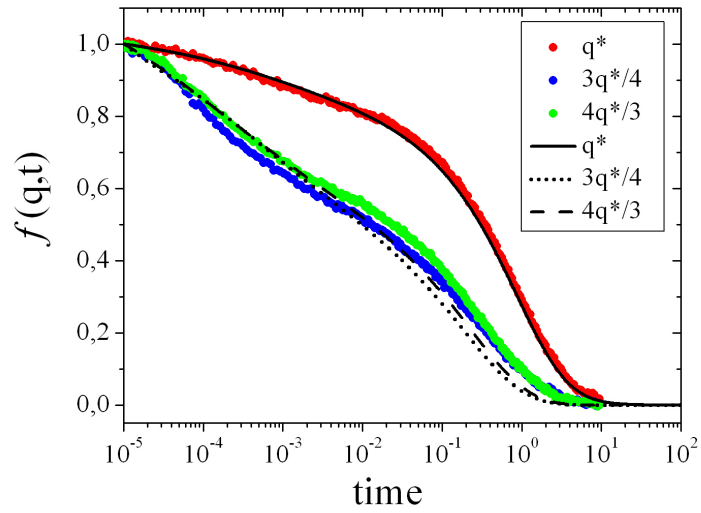

FIG. 4: Dynamic structure factor at different q (see Fig. 2)

ACKNOWLEDGEMENTS

I want to express my gratitude to Dr. A. M. Puertas for helpful discussions and for supplying his results of Brownian Dynamics simulations.

Reference List

[1] W. Götze and Th. Voigtmann, Phys. Rev. E **67**, 021502 (2003).

[2] T. Franosch, M. Fuchs, W. Götze, M. R. Mayr, and A. P. Singh, Phys. Rev. E **55**, 7153 (1997).

[3] Th. Voigtmann, A.M. Puertas, and M. Fuchs, Phys. Rev. E **70**, 061506 (2004).

Papers and Proceedings

(Peer review: 8. Conference proceedings: 1)

1- W. Kob, **S. Roldán-Vargas**, and L. Berthier. *Non-monotonic temperature evolution of dynamic correlations in glass-forming liquids*. Under revision in Nature, Dec.15, 2010. http://w3.lcvn.univ-montp2.fr/~berthier/divers/kob.pdf

2- I. Pérez-Victoria, F. J. Pérez-Victoria, **S. Roldán-Vargas**, R. García-Hernández, L. Carvalho, S. Castanys, F. Gamarro, J. C. Morales, and J. M. Pérez-Victoria. *Non-reducing trisaccharide fatty acid monoesters: Novel detergents in membrane biochemistry*. Biochim. Biophys. Acta 1808, 717 (2011).

3- **S. Roldán-Vargas**, J. de Vicente, R. Barnadas-Rodríguez, M. Quesada-Pérez, J. Estelrich, and J. Callejas-Fernández. *Suspensions of repulsive colloidal particles near the glass transition: Time and frequency domain descriptions*. Phys. Rev. E 82, 021406 (2010).

4- **S. Roldán-Vargas**, M. Peláez-Fernández, R. Barnadas-Rodríguez, M. Quesada-Pérez, Estelrich, and J. Callejas-Fernández. *Nondiffusive Brownian motion of deformable particles: Breakdown of the "long-time tail"*. Phys. Rev. E 80, 021403 (2009). Selected for the August 31, 2009 issue of Virtual Journal of Nanoscale Science and Technology.

5- **S. Roldán-Vargas**, M. Quesada-Pérez, and J. Callejas-Fernández. *Stochastic description of the light scattered by a polydisperse colloidal suspension: Simulation and experiment*. J. Chem. Phys. 131, 034509 (2009).

6- **S. Roldán-Vargas**, R. Barnadas-Rodríguez, M. Quesada-Pérez, J. Estelrich, and J. Callejas-Fernández. *Liquid-glass transition in suspensions of charged liposomes*. AIP Conf. Proc. 1091, 179 (2009).

7- **S. Roldán-Vargas**, R. Barnadas-Rodríguez, M. Quesada-Pérez, J. Estelrich, and J. Callejas-Fernández. *Surface fractals in liposome aggregation*. Phys. Rev. E 79, 011905 (2009). Selected for the January 15, 2009 issue of Virtual Journal of Biological Physics Research.

8- **S. Roldán-Vargas**, R. Barnadas-Rodríguez, A. Martín-Molina, M. Quesada-Pérez, J. Estelrich, and J. Callejas-Fernández. *Growth of lipid vesicle structures: From surface fractals to mass fractals*. Phys. Rev. E 78, 010902 (2008) (Rapid Communications). Selected for the August 1, 2008 issue of Virtual Journal of Biological Physics Research.

9- **S. Roldán-Vargas**, A. Martín-Molina, M. Quesada-Pérez, R. Barnadas-Rodríguez, J. Estelrich, and J. Callejas-Fernández. *Aggregation of liposomes induced by calcium: A structural and kinetic study*. Phys. Rev. E 75, 021912 (2007). Selected for the March 1, 2007 issue of Virtual Journal of Biological Physics Research.